# UNIVERSITÀ DEGLI STUDI DI BARI
*Aldo Moro*

Dipartimento Interateneo di Fisica '*M. Merlin*'


---

Scuola di Dottorato di Ricerca in Fisica

Ciclo XXV

Settore scientifico disciplinare: FIS/01

# Background Estimation for the Search of the Standard Model Higgs Boson in the Decay Channel H$\rightarrow ZZ^* \rightarrow 4\ell$ with the CMS experiment at $\sqrt{s} = 7$ TeV and 8 TeV


**Dottorando:**
Dott. Gurpreet Singh

**Coordinatore:**
Chiar.mo Prof. Salvatore Vitale Nuzzo

**Supervisore:**
Chair.mo Giorgio Pietro Maggi

Dott. Nicola De Filippis


---

**Esame Finale 2013**

To all those who continuously seek the truth . . .

"Our judge is not God or governments, but Nature."

- *Tejinder Singh Virdee*

# Acknowledgements

I would like to begin by thanking my Ph.D. supervisor, Nicola De Filippis, whose insistence on expressing problems in the most simplistic terms and enthusiastic scientific attitude, helped me to guide towards the core and fundamental issues of physics problems. I am extremely grateful for the fundamental and social support, that I have received from Giorgio Pietro Maggi, who has served as a second advisor for me. Additionally, I want to thank to Marcello Maggi, who have given numerous sharp and critical suggestions during my Ph.D. period. I am sincerely thankful to Lucia Silvestris, Anna Colaleo, Donato Creanza, Alexis Pompili, Director of INFN Bari, Director of Department of Physics and to the whole CMS Bari community for their continuos support and cooperation.

I owe the deepest thanks to referees of this thesis: Francesco Conventi (Universita e INFN Napoli) and Roberto Bellotti (Bari) for their careful reading and valuable suggestions to improve the quality of my thesis' content.

I thank Giacinto Donvito for his cooperation and always being available. I also wish to thank to Anna Massarelli and all members of administrative staff of INFN and Physics department.

I want to thank all the people for their help and support, who have worked with me on this analysis or indirectly helped in my work: Joe Bochenek, Marco Meneghelli, Paolo Giacomelli, Mario Masciovecchio, Cristina Botta, Roberto Salerno, Adish Vartak, Lorenzo Bianchini, Simranjit Singh Chhibra, Piet Verwilligen.

I am very grateful to Ashok Kumar (DU, India), who have motivated me to join particle physics and always helped in every possible way.

I want to thank, in particular, the friends who have made my stay a wonderful and memorable in Bari during last three years: Mahinder, Gurpreet Selopal, Nicola tritto, Francesco Barille, Giacomo, Nicola pacifico, Liliana, Giorgia, Massimo, Mario, Cessare, Rosamaria, Raffaella, Emilia. Finally, I thank to all of my fellow students, postdocs and all colleagues from Bari and CERN for all of their support through the years.

I owe the great gratitude to my mother Charanjeet Kaur and my father Wassan Singh for giving me life and guiding me to where I am today. I thank them and my younger brother Harpreet Singh for their unconditional love and support.

Last but not least, the Chain of my gratitude would be definitely incomplete if I would forget to thank the first and the major cause of this chain, The Almighty "God". My deepest and sincere gratitude for inspiring and guiding this humble being.

*Gurpreet Singh*

*February* 11, 2013

# Contents

# List of Figures

# List of Tables

# Introduction

Physics is a scientific discipline and its primary aim is to describe all naturally occurring phenomena in terms of the matter content of the universe and mutual interaction of matter, which results in inventions of numerous applications for mankind from best available understanding of nature. Elementary particle physics addresses these goals at the most fundamental level and attempts to comprehend the most basic building blocks of matter to elucidate the basic interactions between them. In the $20^{th}$ century, a new experimental branch known as high energy physics (HEP) evolves from this theoretical branch, which studies the interactions between elementary particles at very high energy. By using particle accelerators and colliders, these high energy interactions allow the production of new particles which generally don't exist in nature under ordinary conditions.

Historically, progress in particle physics has followed a reductionist path, whereby layers of complexity have been successfully explained in terms of ever more basic building blocks. Atoms were reduced to electrons, protons and neutrons, and protons and neutrons were in turn reduced to quarks and gluons. Similarly, the electric and magnetic forces were combined into the electromagnetic force, which was in turn combined with the weak force to give us the combined description of the electroweak forces. These successes have converged, at the current state of our understanding, to the theory of elementary particles and interactions known as the standard model (SM) of particle physics. The SM predicts the existence of a unique physical Higgs scalar boson associated to the spontaneous electroweak symmetry breaking, the so called *Higgs mechanism*.

The SM is the quantum field theory (QFT), which has the greatest number of experimental verifications till date. In particular, the Higgs boson mass, like those of quarks, leptons and gauge bosons, is a free parameter of the theory. Direct searches for the SM Higgs boson have been already performed at the $e^+e^-$ collider LEP and at the $p\bar{p}$ collider Tevatron. A lower bound of $m_H \geq 114.4$ GeV/c$^2$ at 95% CL (Confidence Level) has been set for the Higgs mass at LEP [1], while the D0 and CDF experiments at Tevatron excluded the mass range $162 \leq m_H \leq 166$ GeV/c$^2$

(95% CL) and reported an excess of events in the range 120-135 GeV/$c^2$ [2]. Despite the success of best available theoretical and experimental understanding of Particle Physics, still we have some open fundamental questions as:

- What is the mechanism for electroweak gauge symmetry breaking, which generates the masses of the W and Z bosons ?
- What are the masses of the neutrinos and what is the mechanism that generates them [3] ?
- What is the origin of dark energy and dark matter, accounting for more than 95 % of the energy density of the universe and more than 80 % of its matter [4] & [5] ?

The work presented in this thesis will contribute to get an answer of the first question by using data collected with the CMS detector. The search for the SM Higgs boson is one of the main goal of the CMS experiment at the Large Hadron Collider (LHC) of CERN. The current analysis has been performed over proton-proton collision data collected by the CMS detector in years 2011 ($\mathcal{L}_{int} = 5.05$ fb$^{-1}$ @ $\sqrt{s} = 7$ TeV) and 2012 ($\mathcal{L}_{int} = 12.21$ fb$^{-1}$ @ $\sqrt{s} = 8$ TeV).

The searches for the SM Higgs boson has to cope with several SM or electroweak processes that may have similar final states as those of the Higgs signal [1] and generally known as 'background processes'. The development of accurate background estimation techniques will lead to more confident experimental observation about the existence or exclusion of the Higgs boson in that particular decay mode. An experimental methodology has been developed to estimate all background processes in a particular decay mode of the SM Higgs boson, when it decays as $H \rightarrow ZZ^*$ and each Z boson further decays into a muon pair or electron pair.

In chapter 1, a short theoretical introduction to the SM Higgs physics and SM background processes is given in context of $H \rightarrow ZZ^* \rightarrow 4\ell$ decay mode. The production mechanism of relevant background processes and Higgs boson will be briefly presented in the same. The chapter 2 contains a comprehensive description of the LHC and CMS experiment. The reconstruction, identification and isolation techniques for leptons are presented briefly in chapter 3. The key information about Monte Carlo samples, event generators and data samples used in current analysis is discussed in the same chapter.

[1] In accord with current work, the phase space populated by signatures of the SM Higgs boson-like events, is called 'signal phase space' and corresponding events are called 'signal events'. The signal phase space is dedicated to examine the leptons coming from H$\rightarrow$ ZZ$^*$ decay chain.

The studies about important physics observables over Monte Carlo simulations are presented in the same, which helps to understand and finalize better working points to differentiate between Higgs signal and background processes.

The chapter 4 will discuss background estimation methodologies in context of $H \rightarrow ZZ^* \rightarrow 4\ell$ analysis. The principal sources of background come from almost irreducible ZZ continuum, instrumental backgrounds such as Z+jets or WZ+jet(s) where jets are misidentified as leptons and reducible background Z$b\bar{b}$/Z$c\bar{c}$, $t\bar{t}$ processes, where Z and W's undergoes leptonic decays and two secondary leptons produced within b-jets. Individual control regions (CR) are defined for the estimation of corresponding backgrounds in Higgs signal phase space.

In addition, an alternate event selection methodology has been presented to increase the event selection efficiency for Higgs signal.

The estimated values of contributing background processes along with relevant sources of uncertainties are described in chapter 5. It also contains the complete results about four lepton mass spectrum, the event yields of contributing signal and background processes in signal phase space and statistical results of $H \rightarrow ZZ^* \rightarrow 4\ell$ decay mode. The contribution of background estimation results in ZZ cross section measurement and for $H \rightarrow ZZ^* \rightarrow 4\ell$ analysis by Bayesian approach will be discussed briefly.

# Chapter 1

# The Standard Model

The fundamental components of matter and their interactions are described by the standard model (SM) of particle physics, which is based upon two separate quantum field theories (QFT) [6], describing the electroweak interaction (Glashow-Weinberg-Salam model or GWS) and the strong interaction (Quantum Chromo-Dynamics or QCD). Theoretical and experimental studies in particle physics for more than fifty years have led to the development of the current SM of particle physics. Although it is still incomplete, the SM is widely accepted as the most reliable theory to describe all observed particles and their mutual interactions. In first half of current chapter, a brief introduction to the theoretical base of the SM will be presented. For more details, extensive bibliography is available in this subject as Ref. [7]. The production mechanisms of the SM Higgs signal and relative background processes are discussed briefly in second half of this chapter.

## 1.1 The Standard Model of Elementary Particles

The four fundamental forces that we observe in nature are the electro-magnetic force, the weak force, the strong force and the gravitational force. The SM describes all of these forces with the exception of the gravitational force because *gravity* is extremely weak to have visible effects at the 'TeV' scale. In the SM, the interactions between particles are described in terms of the exchange of *bosons*, integer-spin particles which are carriers of the fundamental interactions. Each fundamental force is associated with *spin 1* mediator particles. The strong force is mediated by 8 colored gluons and the electromagnetic force is mediated by the photon, while the weak interactions are mediated by the $W^{\pm}$ and Z bosons. The main characteristics of fermions, bosons and corresponding interactions are summarized in Tab. (1.1) and Fig. (1.1).

Table 1.1: Fundamental interactions

| | Electromagnetic | Weak | Strong |
|---|---|---|---|
| Quantum | Photon ($\gamma$) | $\mathrm{W}^{\pm}, Z$ | Gluons |
| Mass ($\frac{\mathrm{GeV}}{\mathrm{c}^2}$) | 0 | 80, 90 | 0 |
| Coupling constant | $\alpha(Q^2 = 0) \approx \frac{1}{137}$ | $\frac{\mathrm{G_F}}{(\mathrm{hc})^3} \approx 1.2 \cdot 10^{-15} (\frac{\mathrm{GeV}}{\mathrm{c}^2})$ | $\alpha(m_Z) \approx 0.1$ |
| Range (cm) | $\infty$ | $10^{-16}$ | $10^{-13}$ |
| Self-interaction | No | Yes | Yes |

The SM describes the matter as composed by twelve elementary particles, *fermions* (6 quarks and 6 leptons) grouped in three generations. The higher generation particles decay via weak interactions to lower generation particles, explaining why the low energy world (as it is known today) consists only of particles of the first generation. For each fermion, there exists also a corresponding anti-fermion which carry same mass but opposite electric charge.

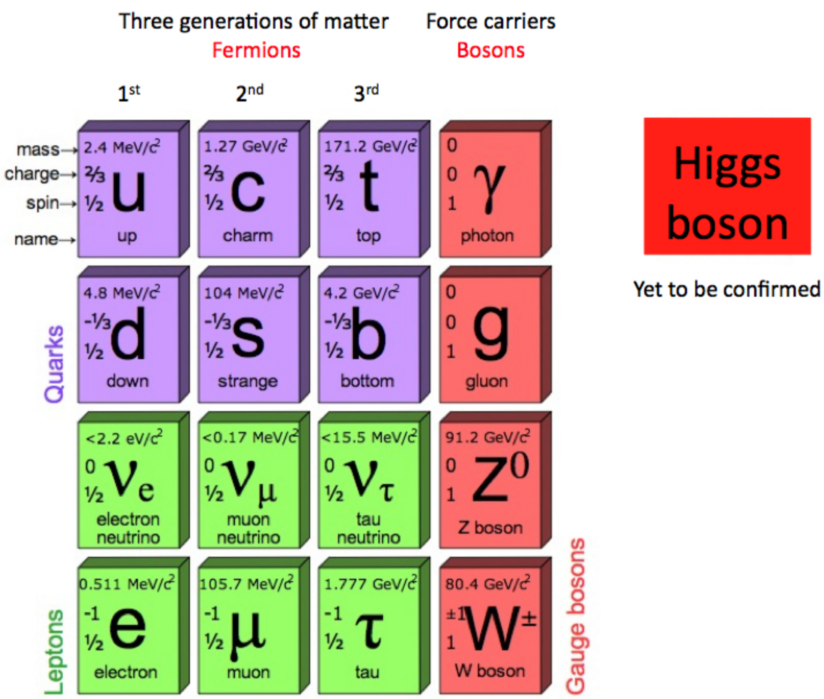


Figure 1.1: The SM fermions and bosons grouped in generations

The three leptons $e^-, \mu^-, \tau^-$ have charge of -1 while the corresponding neutrinos are neutral. Neutrinos were introduced in the SM as massless particles however recent results from neutrino oscillation experiments points that neutrinos having very small but non- zero masses. Quarks are subject to both strong and electroweak interactions and do not exist as free states, but only as constituents of a wide class of particles, the *hadrons*, such as protons and neutrons. On the other hand, leptons only interact through electromagnetic and weak forces. The three charged leptons are identical with respect to interaction with all known fundamental forces irrespective to their differences in mass.

The standard model is formulated mathematically as a field theory under the $SU(3) \otimes SU(2)_L \otimes U(1)$ symmetry. SU(3) describes color and interactions between gluons and quarks, while $SU(2)_L \otimes U(1)$ describes electroweak interactions. By Noethers theorem, each symmetry corresponds to a conservation law yielding a conserved quantity, which, in the case of the standard model, are color, weak isospin and hypercharge for the three symmetry groups mentioned respectively. In the unbroken $SU(2)_L \otimes U(1)$ symmetry, gauge bosons and fermions are required to be massless. The mass of the weak bosons ($W^{\pm}$ & Z) is explained by breaking of the symmetry between the electromagnetic and weak interactions via the Higgs mechanism described in the next section.

## 1.2 The Higgs mechanism

The gauge bosons and fermions are massless by the electroweak unification theory but experimentally it is not found true. This section describes spontaneous symmetry breaking which is the mechanism through which weak gauge bosons are believed to acquire their masses [6], [8]. To illustrate spontaneous symmetry breaking two examples are studied, a global gauge symmetry and a local gauge symmetry applied to U(1) and SU(2) symmetry groups. First we start from a complex scalar field $\phi = (\phi_1 + i\phi_2)/\sqrt{2}$ described by the Lagrangian:

$$\mathcal{L} = (\partial_\mu \phi) * (\partial^\mu \phi) - \mu^2 \phi^* \phi - \lambda (\phi^* \phi)^2 \tag{1.1}$$

where the first term is the kinetic energy term, the second term is the mass term and the third term is an interaction term. This Lagrangian is invariant under global gauge transformation $\phi \to e^{i\alpha}\phi$ with $\alpha$ independent on spatial coordinates. The Lagrangian is

$$\mathcal{L} = \frac{1}{2}(\partial_\mu \phi_1)^2 + \frac{1}{2}(\partial_\mu \phi_2)^2 - \frac{1}{2}\mu^2(\phi_1^2 + \phi_2^2) - \frac{1}{4}\lambda(\phi_1^2 + \phi_2^2)^2. \tag{1.2}$$

If the case where $\lambda > 0$ and $\mu^2 < 0$ is considered, a circle of minima of the potential V($\phi$) is observed in the $\phi_1$, $\phi_2$ plan of radius $v$, such that

$$\phi_1^2 + \phi_2^2 = v^2 \qquad with\ v^2 = -\frac{\mu^2}{\lambda}. \tag{1.3}$$

The fact that the minimum is not at $\phi = 0$ is very interesting for perturbation theory to work; the Lagrangian has to be defined around the global minimum, that is now at $v$. Therefore the field needs to be translated to the new minimum by redefining it as:

$$\phi(x) = \sqrt{\frac{1}{2}}(v + \eta(x) + i\xi(x)). \tag{1.4}$$

Substituting the new field into the Lagrangian gives:

$$\mathcal{L}' = \frac{1}{2}(\partial_\mu \xi)^2 + \frac{1}{2}(\partial_\mu \eta)^2 + \mu^2\eta^2 + \mathcal{O}(\eta^3, \xi^3, \eta^4, \xi^4). \tag{1.5}$$

The third term shows that the new Lagrangian has acquired a new mass term for the field $\eta$ with mass $\mu_\eta = \sqrt{-2\mu^2}$, however there is no term like that for the field $\xi$. This is a consequence of the Goldstone theorem, which states that whenever a continuos symmetry is spontaneously broken, always massless scalars occur in the new theory (the field $\xi$ in this case).
The next step is to repeat the same process in a local gauge invariant $U(1)$ symmetry. So let's assume a scalar field interacting with an electromagnetic field. The theory is described by the Lagrangian:

$$\mathcal{L} = |D_\mu \phi|^2 - \mu^2\phi^*\phi - \lambda(\phi^*\phi)^2 - \frac{1}{4}F_{\mu\nu}F^{\mu\nu} \tag{1.6}$$

where $D_\mu = \partial_\mu - ieA_\mu$ is the covariant derivative and the transformation is $\phi \rightarrow e^{i\alpha(x)}\phi$. For $\mu^2 < 0$ the field has a new minimum $v$ exactly as before. Translating the Lagrangian to the new minimum gives:

$$\begin{aligned}\mathcal{L}' = &\frac{1}{2}(\partial_\mu \xi)^2 + \frac{1}{2}(\partial_\mu \eta)^2 + (-v^2\lambda\eta^2) + \frac{1}{2}e^2v^2A_\mu A^\mu \\ &- evA_\mu\partial^\mu\xi - \frac{1}{4}F_{\mu\nu}F^{\mu\nu} + other\ interaction\ terms\end{aligned} \tag{1.7}$$

In this new Lagrangian, the field $\eta$ has acquired a mass of $m_\eta = \sqrt{2\lambda v^2}$ but even more important is the fact that the field $A_\mu$ has also acquired a mass $m_A = ev$, which implies that the gauge boson of this theory became massive. The residual issue is that the field $\xi$ is still massless, which implies that the Goldstone theorem could still stand. In addition, the presence of a term $A_\mu\partial^\mu\xi$ introduces a coupling of the $A_\mu$ field to the scalar field. In terms of physics, the mass acquired by field $A_\mu$ results as creation of one more polarization degrees of freedom *i.e.* longitudinal polarization.

The additional term $A_\mu \partial^\mu \xi$ provides the term needed to make the polarization transverse because simply translating the field variables as in eq. 1.4, does not create a new degree of freedom. Therefore the particle spectrum in the Lagrangian is not correct and one of the fields in the Lagrangian doesn't correspond to a particle. The gauge invariance of the Lagrangian can be used to redefine it in a way that the particle content is more understandable. The complex field was defined as:

$$\phi = \sqrt{\frac{1}{2}}(v + \eta + i\xi) \approx \sqrt{\frac{1}{2}}(v + \eta)e^{\frac{i\xi}{v}} \tag{1.8}$$

It implies that the gauge can be picked differently so that

$$\phi \to \sqrt{\frac{1}{2}}(v + h(x))e^{\frac{i\theta(x)}{v}} \tag{1.9}$$

$$A_\mu \to A_\mu + \frac{1}{ev}\partial_\mu \theta \tag{1.10}$$

This particular choice of gauge transformation is known as the unitary gauge and is designed to make $h(x)$ real. Since $\theta$ appears as a phase factor, it will not appear in the final Lagrangian. Substituting into eq. 1.6 gives the final Lagrangian as:

$$\begin{aligned} \mathcal{L}'' = &\frac{1}{2}(\partial_\mu h)^2 - \lambda v^2 h^2 + \frac{1}{2}e^2 v^2 A_\mu^2 - \lambda v h^3 - \frac{1}{4}\lambda h^4 \\ &+ \frac{1}{2}e^2 A_\mu^2 h^2 + v e^2 A_\mu^2 h - \frac{1}{4}F_{\mu\nu}F^{\mu\nu} \end{aligned} \tag{1.11}$$

In this new Lagrangian, the field $A_\mu$ has acquired a mass via the term $\frac{1}{2}e^2 v^2 A_\mu^2$ and there is no massless Goldstone boson in the Lagrangian but a new scalar $h$ with a mass of $m = \sqrt{2\lambda v^2}$ called the *Higgs boson*. So with this procedure the massless Goldstone boson has been converted to the additional longitudinal polarization degree of freedom so that the field acquires mass resulting in a Lagrangian with a scalar massive particle, a massive field and interaction terms. This procedure is known as the *Higgs mechanism*. For this mechanism to be the way for vector bosons to acquire mass in nature, a new particle must exist. The Higgs boson has not been yet discovered and the purpose of this thesis is to contribute in this quest by estimating the background processes of $H \to ZZ^* \to 4\ell$ decay channel.

The last step is to apply the Higgs mechanism to the electroweak model based on $SU(2)_L \otimes U(1)_Y$ symmetry and create mass for the vector bosons and fermions. We use the covariant derivative:

$$D_\mu = \partial_\mu + igT_a W_\mu^a + i\frac{g'}{2}B_\mu Y, \tag{1.12}$$

which corresponds to gauge invariance for the $SU(2)_L \otimes U(1)_Y$ symmetry. Substitution of eq. 1.12 in the Lagrangian of the scalar field (*i.e.* eq. 1.1 ) gives:

$$\mathcal{L} = \left| \left( i\partial_\mu - gT_a \cdot W_\mu^a - g' B_\mu \frac{Y}{2} \right) \phi \right|^2 - V(\phi) \tag{1.13}$$

For this Lagrangian to be invariant, $\phi$ must be invariant under $SU(2)_L \otimes U(1)_Y$ symmetry. A choice satisfying this is using an isospin doublet with Y=1:

$$\phi = \begin{pmatrix} \phi^+ \\ \phi^0 \end{pmatrix} \tag{1.14}$$

$$where \quad \begin{array}{l} \phi^+ \equiv (\phi_1 + i\phi_2)/\sqrt{2} \\ \phi^0 \equiv (\phi_3 + i\phi_4)/\sqrt{2} \end{array}$$

The new field will have a vacuum expectation value of

$$\phi_0 \equiv \frac{1}{\sqrt{2}} \begin{pmatrix} 0 \\ v \end{pmatrix} \tag{1.15}$$

Expanding the kinetic term of the scalar field and using the Pauli matrices as the generators of SU(2) gives:

$$\left| \left( -ig\frac{T_a}{2} W_\mu^a - i\frac{g'}{2} B_\mu \right) \phi \right|^2 =$$

$$\frac{1}{8} \left| \begin{pmatrix} gW_\mu^2 + g'B_\mu & g(W_\mu^1 - iW_\mu^2) \\ g(W_\mu^1 + iW_\mu^2) & -gW_\mu^3 + g'B_\mu \end{pmatrix} \begin{pmatrix} 0 \\ v \end{pmatrix} \right|^2 =$$

$$\left( \frac{1}{2} vg \right)^2 W_\mu^+ W^{-\mu} + \frac{v^2}{8} (W_\mu^3, B^\mu) \begin{pmatrix} g^2 & -gg' \\ -gg' & g'^2 \end{pmatrix} \begin{pmatrix} W^{3\mu} \\ B^\mu \end{pmatrix}$$

where we used the $W$ raising and lowering operators, defined as $W_\mu^\pm = \left( W_\mu^1 \mp iW_\mu^2 \right)/\sqrt{2}$. The first term in this expression corresponds to a massive $W$ boson with mass of

$M_W = vg/2$. The matrix term can be expressed as a function of the fields $A$ and $Z$ by finding a transformation between $W^3$, $B$ and $A, Z$ that diagonalizes the matrix so that the elements in the diagonal are the mass terms $\frac{1}{2}M_Z^2 Z_\mu^2$, $\frac{1}{2}M_A^2 A_\mu^2$, for $Z$ and $A$ respectively. The transformation is:

$$A_\mu = \frac{g' W_\mu^3 + g B_\mu}{\sqrt{g^2 + g'^2}} \tag{1.16}$$

$$Z_\mu = \frac{g W_\mu^3 - g' B_\mu}{\sqrt{g^2 + g'^2}} \tag{1.17}$$

from which is derived that $M_A = 0$ (the photon remains massless) and $M_Z = \frac{v}{2}\sqrt{g^2 + g'^2}$. Therefore all gauge bosons gained mass, the photon mass is zero and there is one additional scalar particle. The two couplings $g$ and $g'$ are related by electroweak unification via the weak mixing angle $\theta_w$ as $tan\theta_w = g'/g$. The final step is to give mass to the fermions. The problem in $SU(2)_L \otimes U(1)_Y$ was that the mass term $m\bar{\psi}\psi$ was not invariant. This can be solved by introducing a fermion coupling to the Higgs. In case of electrons, a term can be added in the Lagrangian of the form:

$$\mathcal{L}_e = -K \left[ \begin{pmatrix} \bar{\nu}_e & e^- \end{pmatrix}_L \begin{pmatrix} \phi^+ \\ \phi \end{pmatrix} e_R + e_R^- \begin{pmatrix} \phi^- & \bar{\phi}^0 \end{pmatrix} \begin{pmatrix} \nu_e \\ e \end{pmatrix}_L \right] \tag{1.18}$$

Substituting the form of the Higgs field in the unitary gauge the Lagrangian becomes

$$\mathcal{L}_e = -\frac{K}{\sqrt{2}} v(e_L^- e_R + e_R^- e_L) - \frac{K}{\sqrt{2}} v(e_L^- e_R + e_R^- e_L)h \tag{1.19}$$

Picking the constant $K$ such as that $m_e = Kv/\sqrt{2}$ gives a fermion mass term in the Lagrangian:

$$\mathcal{L}_e = -m_e e^- e - \frac{m_e}{v} e^- e h, \tag{1.20}$$

Therefore the electron has acquired mass and a new coupling has been introduced between the Higgs boson and the fermions proportional to the ratio of the electron and $W$ mass, which is very small since $m_e$ is small.

## 1.3 Z and Higgs Boson Production in p-p collisions

The standard model describes all interactions between quarks and leptons. Those interactions result in production and decay of the $W^{\pm}, Z$ and Higgs bosons. However to study scalar and vector boson production in proton collisions, the hard interaction between quarks and gluons has to be separated from the proton substructure. The quarks inside the proton are not free but are strongly bound, exchanging colored gluons. The continuous interactions between the quarks makes them virtual particles lying off their mass shell. Gluons are carrying about 50% of the proton momentum and can produce additional quark-antiquark pairs (e.g. $b\bar{b}$). The quark content of the proton is separated into the valence quarks $(u, d)$, the sea quarks $(u, d, s, c)$ and the gluons, together called *partons*.

Therefore, in a proton collision, any quark or gluon combination can contribute to the hard scattering process. The probabilities for a specific parton with a given momentum fraction of the proton to participate in the hard process are known as parton distribution functions and measured by using data from deep inelastic scattering experiments. Therefore the center of mass energy $\sqrt{s}$ for each hard scattering process is related to the center of mass energy of the two colliding protons $\sqrt{S}$ as:

$$s = xyS \tag{1.21}$$

where $x, y$ are the momentum fractions of the contributing partons. One important aspect of hadron colliders is that those parton distribution functions make them versatile machines for discovery although the hard scattering center of mass is not well defined. If the center of mass energy of the protons is high enough, depending on the parton momentum fractions, every collision will create particles of different masses and the possibility to observe new physics increases. This section describes the phenomenology of Z, a rare decay process of Z$\rightarrow 4\ell$ and Higgs bosons production mechanism in proton collisions.

### 1.3.1 Z boson production

The $Z$ boson is produced in proton-proton collisions at leading order by fusion of quark- antiquark pairs. The simplest diagram that can create a $Z$ boson is shown in Fig 1.2 (a). In this process, the $Z$ boson has no transverse momentum but is created and moving along the beamline. This process can create a virtual photon that will decay to a fermion pair or a $Z$ boson or a $W^+W^-$ boson or ZZ. Neglecting the virtual photon part and assuming massless fermions, the matrix element for the $Z$ production is:

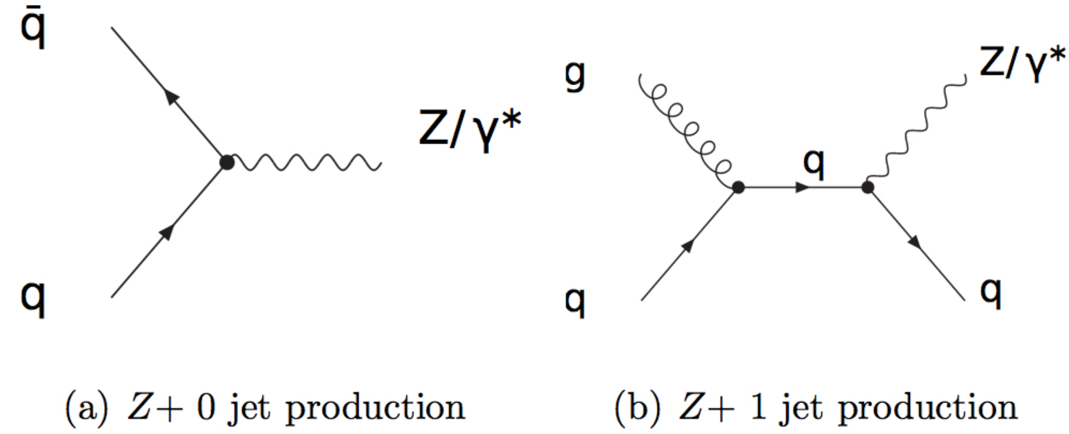


Figure 1.2: Z boson production mechanisms in hadron colliders.

$$|\mathcal{M}|^2 = (s\sqrt{2}g_Z)^2 \frac{(g_V)^2 + (g_A)^2}{2} M_Z^2 = 32 \frac{G_F}{\sqrt{2}}(g_V^2 + g_A^2) M_Z^4 \tag{1.22}$$

and the differential cross section at parton level is:

$$\sigma = 8\pi \frac{G_F}{\sqrt{2}}(g_V^2 + g_A^2) M_Z^4 \delta(s - M_Z^2), \tag{1.23}$$

where $s$ is the center of mass energy of the colliding quarks. This formula implies that to create a $Z$ boson, the two quarks must have a center of mass energy equal to the mass of $Z$ boson. In lepton colliders where elementary particles are colliding, the energy of the beams is set to the $Z$ mass to create a $Z$ boson. In hadron colliders the situation is different. In the LHC, protons are colliding at a large constant energy of $\sqrt{s} = 7$ TeV in 2011 and $\sqrt{s} = 8$ TeV in 2012. For the $Z$ to be created, two partons from the proton should interact. Those partons must be a quark-antiquark with suitable momentum fractions $x, y$ such that $s = xyS$. Then the parton distribution functions are integrated for $x, y$ to give the full cross section:

$$\sigma = \frac{8\pi}{3}\frac{G_F}{\sqrt{2}} \int dxdy \sum (g_V^2 + g_A^2) xyS f_q(x) f_{\bar{q}}(y) \tag{1.24}$$

where the integration is performed under the constraint $xyS = M_Z^2$ and $f_q$ are the parton distribution functions (PDF). The sum runs over all quarks.

There is a significant contribution from higher order diagrams such as one shown in Fig 1.2 (b) resulting in an additional parton in the final state that hadronizes to a jet. Those types of events are also observed and constitute very important background in Higgs searches as it is described in next sections.

In terms of the $Z$ decay signature, the $Z$ boson decays primarily to hadrons or lepton pairs according to the $V - A$ couplings. $Z$ decays to a pair of leptons about 3% of the time for each lepton flavor and the most straightforward final state for $Z$ measurement is a muon or electron pair.

### 1.3.2 Z $\to 4\ell$ process

This process is referred as single-resonant four-lepton production. The leading order (LO) Feynman diagram for the production and decay of $q\bar{q} \to Z \to 4\ell$ is displayed in Fig. 1.3. It has been shown in Ref. [9] that the Z $\to 4\ell$ decay gives a clean resonant peak in the four-lepton invariant mass distribution and number of events in the Z $\to 4\ell$ peak at $m_{4\ell} = m_Z$ is an order of magnitude larger than the expected number of events for the SM Higgs boson with a mass $m_H$ anywhere in the remaining allowed range of 117.5 - 118.5 GeV/$c^2$ and 122.5 - 127.5 GeV/$c^2$ (see Ref. [10, 11]).

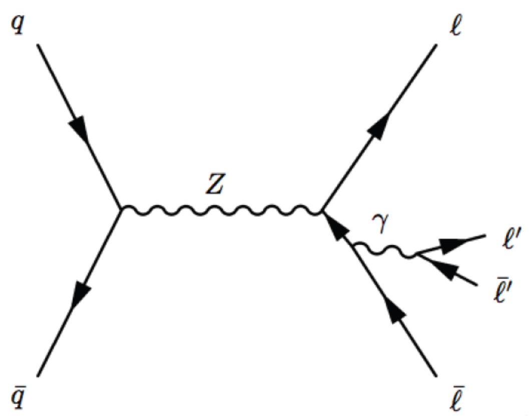


Figure 1.3: The $q\bar{q} \to Z \to 4\ell$ decay process.

Therefore, the Z $\rightarrow 4\ell$ peak can be used for a direct validation for understanding the four-lepton mass scale and the four-lepton mass resolution in the phase space to the Higgs boson four-lepton decays.

### 1.3.3 Higgs boson production

The main processes contributing to the Higgs boson production at a proton-proton collider are represented by the Feynman diagrams in Fig. 1.4. The corresponding cross sections are shown in Fig. 1.5 for centre-of-mass energies of 7 TeV and 8 TeV [12]. The 7 TeV is the energy provided by the LHC during the 2010 - 2011 runs and 8 TeV energy corresponds to runs collected in 2011 - 2012. The total production cross section at 7 TeV is lower than at 8 TeV as shown in Fig. 1.5.

The Higgs boson couples with a strength proportional to the mass, therefore, it has large couplings to $W$ and $Z$ boson pairs. In terms of the fermions, the introduced Yukawa couplings impose a dependence of the coupling as $m_f^2$, therefore the Higgs coupling is enhanced for heavy quarks (especially $t$) and leptons (especially $\tau$). The dominant production modes of Higgs boson are discussed below:

#### 1.3.3.1 Gluon-Gluon Fusion

The gluon fusion [12] through a heavy quark loop is the dominating mechanism for the Higgs boson production at the LHC over the entire mass range [1] due to high luminosity of gluons. The process is shown in Fig. 1.4 (a) with a $t$ quark-loop, which is the main contribution due to its large Yukawa coupling to the Higgs boson. The dynamics of the gluon-fusion mechanism is controlled by strong interactions, which require detailed studies of the effect of QCD radiative corrections and evaluation of electroweak (EW) corrections to obtain accurate theoretical predictions.

The latest results in the computation of the cross section for this process are shown in Fig. 1.5 and used in the analysis presented in this thesis, include next-to-next-to-leading order (NNLO) QCD contributions, complemented with next-to-next-to-leading log (NNLL) re-summation, and next-to-leading order (NLO) electroweak corrections.

An uncertainty of 15-20% on the calculation of this partonic cross section is assumed, mostly depending on the choice of the parton density functions (PDFs), implementation of the EW corrections, missing terms in the perturbative expansion and on the uncalculated higher-order QCD radiative corrections.

[1] 100 GeV/$c^2 \leq M_H \leq$ 1 TeV/$c^2$ being investigated at LHC.

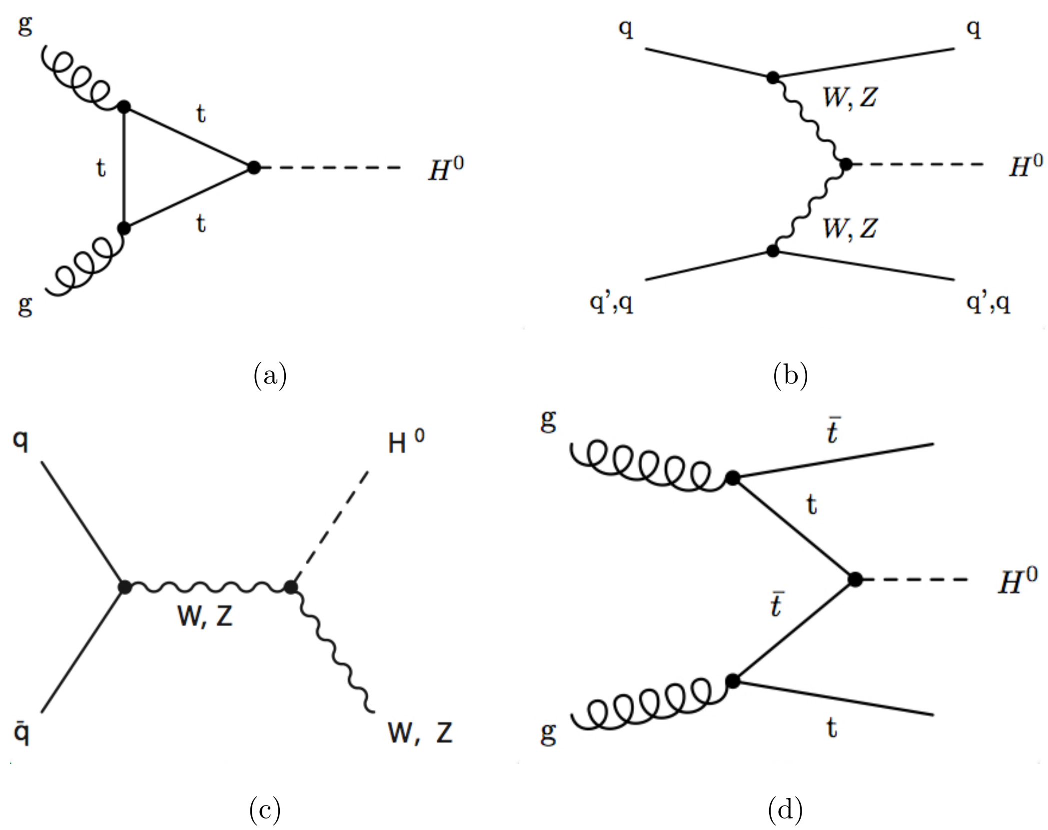


Figure 1.4: Higgs boson production mechanisms at tree level in proton-proton collisions: (a) gluon-gluon fusion, (b) vector boson fusion, (c) W and Z associated production (or Higgsstrahlung), and (d) $t\bar{t}$ associated production.

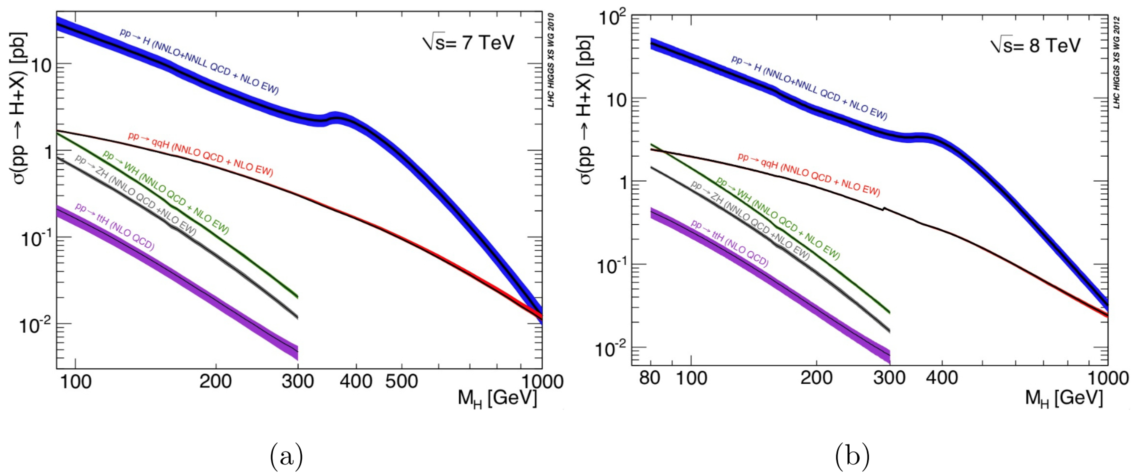


Figure 1.5: Cross sections for the different Higgs boson production modes, as functions of the Higgs boson mass, at LHC's centre-of-mass energy equal to 7 TeV (a) and 8 TeV (b) (see Ref. [12]).

#### 1.3.3.2 Vector Boson Fusion (VBF)

The production of the standard model Higgs boson via fusion of a pair of $W$ or $Z$ bosons in association with two hard jets in the forward and backward regions of the detector, frequently quoted as the vector-boson fusion (VBF) channel [12] and shown in Fig. 1.4 (b). It is second most dominant production mechanism of the Higgs-boson at the LHC. Higgs-boson production in the VBF channel plays also an important role in the determination of Higgs-boson couplings at the LHC. Bounds on non-standard couplings between Higgs and electroweak (EW) gauge bosons can be imposed from precision studies in this channel. In addition this channel contributes in a significant way to the inclusive Higgs production over the full Higgs-mass range.

The production of a Higgs boson + 2 jets receives two contributions at hadron colliders. The first type, where the Higgs boson couples to a weak boson that links two quark lines, is dominated by t- and u-channel-like diagrams and represents the genuine VBF channel. The hard jet pairs have a strong tendency to be forward-backward directed in contrast to other jet-production mechanisms, offering a good background suppression (transverse-momentum and rapidity cuts on jets, jet rapidity gap, central-jet veto etc.).

The presence of two spectator jets with high invariant mass in the forward region provides a powerful tool to tag the signal events and discriminate the backgrounds, thus improving the signal to background ratio, despite the low cross section. Moreover, both leading order and next-to-leading order cross sections for this process are known with small uncertainties and the higher order QCD corrections are quite small. It is about one order of magnitude lower than $gg$ fusion for a large range of $m_H$ values and the two processes become comparable only for very high Higgs masses ($\mathcal{O}$(1 TeV)).

#### 1.3.3.3 Associated Production

The production of the SM Higgs boson in association with a $W^{\pm}$ and Z bosons is usually defined as *Higgsstrahlung* processes, which can be used to tag the event. The process is shown in Fig. 1.4 (c) and is several orders of magnitude lower than those of $gg$-fusion and VBF. It have been considered mainly by exploiting two decay modes, $H \rightarrow W^+W^-$ and $H \rightarrow b\bar{b}$. The former is examined as it could contribute to the measurement of the Higgs boson coupling to W bosons and the latter decay mode might contribute to the discovery of a low-mass Higgs boson and allow to measure the coupling of the Higgs boson to b quarks. The cross section for this process is known at the NNLO QCD and NLO EW level. The inclusion of these available contributions increases the LO cross section by about 20-25%.

The last process, illustrated in Fig. 1.4 (d), is the associated production of a Higgs boson with a $t\bar{t}$ pair. Also for this process, the cross section is orders of magnitude lower than those of gluon and vector boson fusion. The presence of the $t\bar{t}$ pair in the final state can provide a good experimental signature. For this cross section, NLO QCD calculations are available.

#### 1.3.3.4 Decay modes of the SM Higgs boson

The SM Higgs boson decays primarily to fermion or boson pairs and the branching ratio is enhanced for heavier particles. The Higgs boson decay branching fractions as a function of the Higgs mass are presented in Fig. 1.6.

For low Higgs mass, the primary decays are via $b\bar{b}$ and $\tau\tau$ while for higher masses the $WW$ and $ZZ$ final states dominate. For $m_H \approx 2m_t$, the Higgs decay to top pairs also contributes. Despite the structure of the couplings, the most sensitive modes for the Higgs boson depends upon the experimental reasons. For example, at low mass, the $b\bar{b}$ final state can only contribute via associated production $(WH, ZH)$ since the $pp \to b\bar{b}$ background is overwhelming.

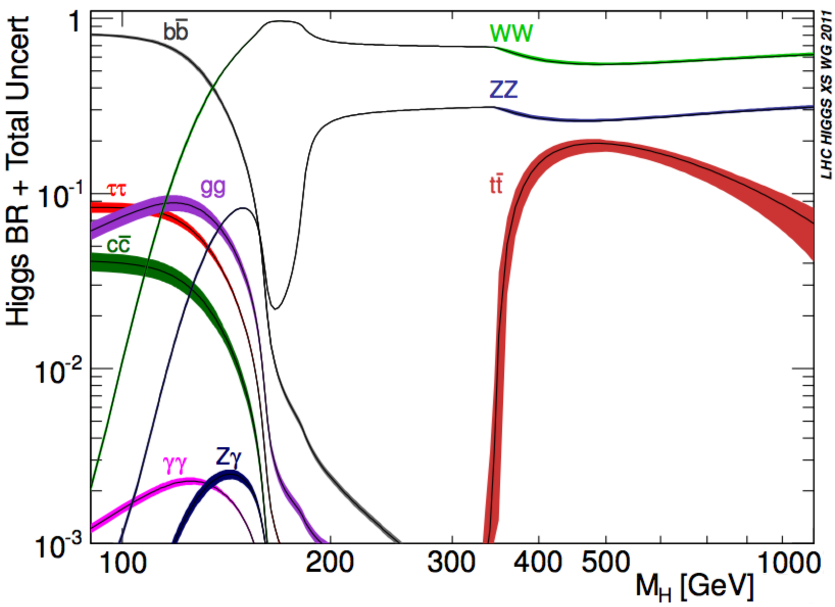


Figure 1.6: The SM Higgs boson decay branching fractions as a function of the Higgs mass.

In the same sense, $H \rightarrow \tau\tau$ dominantly contributes via $VBF$ topologies due to the overwhelming $Z \rightarrow \tau\tau$ background from other production mechanisms. On the other hand, $ZZ$ and $WW$ decay modes also contribute to lower mass Higgs searches because of the clean experimental signatures as leptonic decays *i.e.* $ZZ \rightarrow 4\ell$ and $WW \rightarrow 2l2\nu$. Finally $H \rightarrow \gamma\gamma$ has very low branching ratio but the relatively clean two photon signature provides the best sensitivity at low mass.

## 1.4 The SM Background Processes

The background processes are described in context of H$\rightarrow ZZ^* \rightarrow 4\ell$ decay mode. Here and henceforward, $Z$ stands for $Z, Z^*$ and $\gamma^*$ (wherever applicable). For the event generation, $\ell$ is to be understood as being any charged lepton, $e, \mu$ or $\tau$. The predominant source of backgrounds giving 4 *leptons* as final state are:

- *irreducible ZZ continuum*, which gives 4 lepton in final state as $q\bar{q}\rightarrow ZZ^* \rightarrow 4\ell$ and $gg\rightarrow ZZ^* \rightarrow 4\ell$.
- *reducible backgrounds* as Z$b\bar{b}$, Z$c\bar{c}$ & $t\bar{t}$ processes.
- *instrumental backgrounds* such as Z+jets or WZ+jet(s).

The analysis will focus on reconstructed final states with electrons or muons only and considered final states are: 4$\mu$, 4e, 2$\mu$2e. The production mechanism of some of the main backgrounds is discussed briefly in following sections.

### 1.4.1 Irreducible backgrounds

The four-lepton events from non resonant di-boson production constitute the main source of background events. This background is called 'ZZ continuum' for simplicity throughout the succeeding sections and will be considered in the category of *irreducible backgrounds*, as the event topology and kinematics is very similar to those of Higgs signal events.

The lowest order production mechanism is the one represented in Fig. 1.7a as $q\bar{q} \rightarrow ZZ^*/Z\gamma^*$. In case of SM Higgs boson production via the gluon fusion mechanism, the gluon-induced ZZ background, although technically of NNLO compared to the first order Z-pair production, amounts to a non-negligible fraction of the total irreducible background at masses above the $2m_Z$ threshold. The associated diagram $gg \rightarrow ZZ^*/Z\gamma^*$ is represented in Fig. 1.7b.

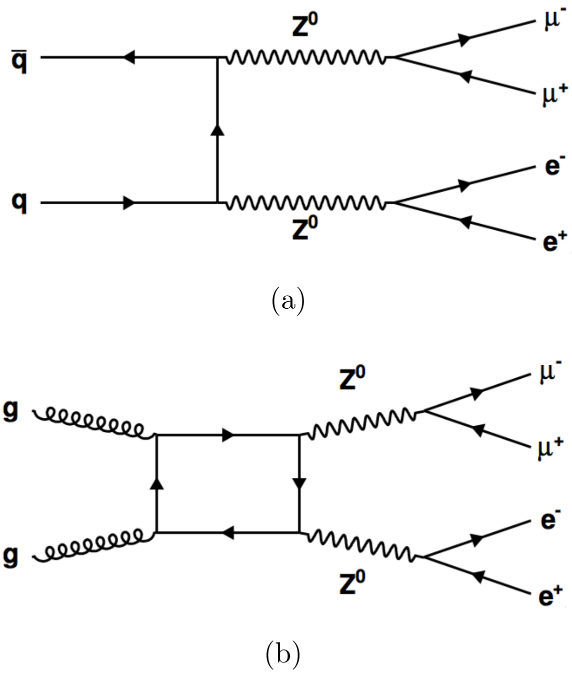


Figure 1.7: Lowest order diagrams for the $q\bar{q} \to ZZ^*/Z\gamma^*$ process (a) and for the $gg \to ZZ^*/Z\gamma^*$ process (b).

### 1.4.2 Reducible backgrounds

The instrumental & reducible backgrounds are contributing in 4 lepton signal phase space because jets can be misidentified as leptons, Z & W's undergoes leptonic decays and b-jets can produce other two leptons from secondary vertices. In addition, the multiple jet production from $QCD$ hard interactions can also contribute in early stages of the analysis, as well as other di-boson ($WW, WZ, Z\gamma$) and single top backgrounds.

In the category of reducible backgrounds, those with final state leptons coming from b (c) decays are the most important. The main source of background events of this type are the associated production of Zb$\bar{b}$/Zc$\bar{c}$ with $Z \to \ell^+\ell^-$ decays, as shown in Fig 1.8. In addition, the production of top quark pairs in the decay mode $t\bar{t} \to W^+bW^-\bar{b} \to \ell^+\ell^-\nu\bar{\nu}b\bar{b}$ have a considerable contribution among reducible backgrounds and shown in Fig 1.9. The B mesons can decay semi-leptonicaly in three different ways:

- with a direct decay (b→ $\ell$, BR $\approx$ 10.7%),
- with a cascade decay (b→c→ $\ell$, BR $\approx$ 8%),
- with a 'wrong sign' cascade decay (b→c→ $\ell$, BR $\approx$ 1.6%).

So these processes with two b/c quarks decaying leptonicaly can lead to $4\ell$ final state events. These backgrounds are called reducible as the experimental signature of leptons from b/c decay can be separated from that of leptons from W and Z decays because those are prompt leptons, which gives different kinematical behavior of final decay products.

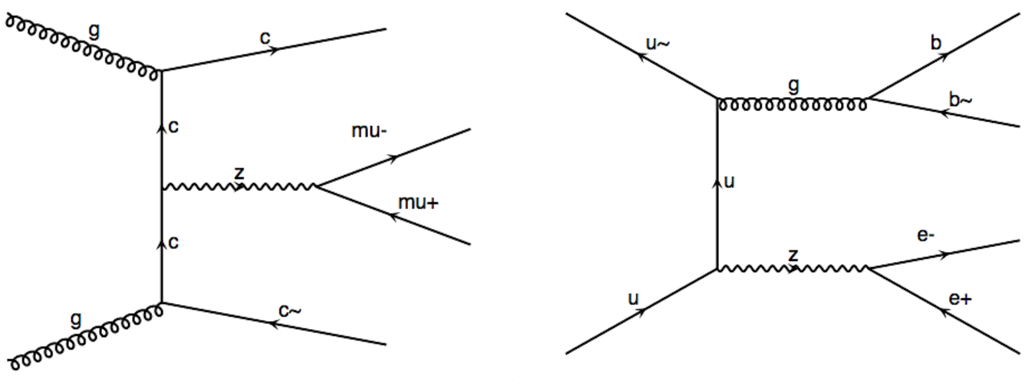


(a) (b)

Figure 1.8: Some of the probable decay modes for Zc$\bar{c}$ (a) and Zb$\bar{b}$ (b), which can give $2\ell$ + 2 heavy flavor jets.

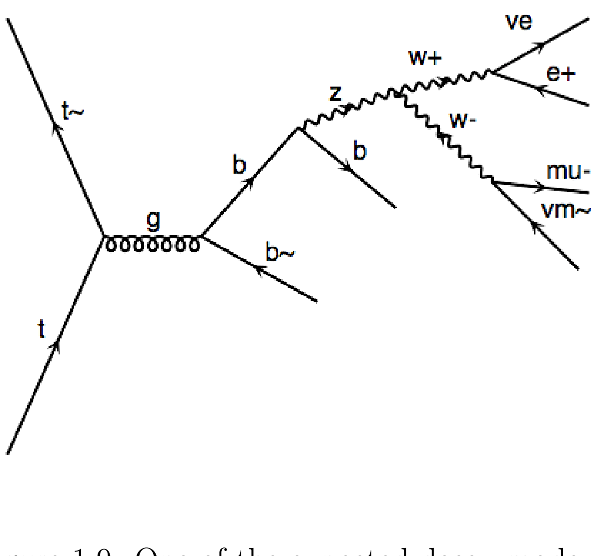


Figure 1.9: One of the expected decay mode of t$\bar{\text{t}}$.

### 1.4.3 Instrumental backgrounds

The category of instrumental backgrounds is used to indicate background events with final state leptons from mis-identification of other particles like jets, *e.g.* Z + light flavor jets (u,d,s), QCD multi-jets and WZ + jets processes where leptons mainly comes from jets faking leptons.

In WZ + jets, the jets can originate from the hadronisation of both light (u, d, s) and heavy (c, b) quarks. Fig 1.10a represents $WZ + jets \rightarrow \ell^{\pm}\nu\ell'^{+}\ell'^{-}(\ell, \ell' = e, \mu$ where one jet in final state can be mis-identified as lepton. Similarly in case of Z + jets decays (see Fig 1.10b, 1.11a & 1.11b) as $2\ell$ + 2 light jets where these 2 additional jets can fake leptons.

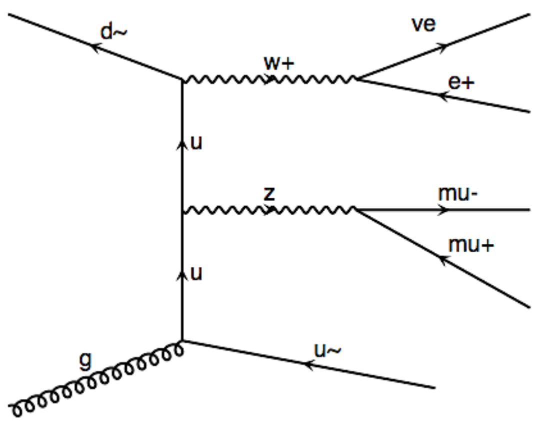


(a)

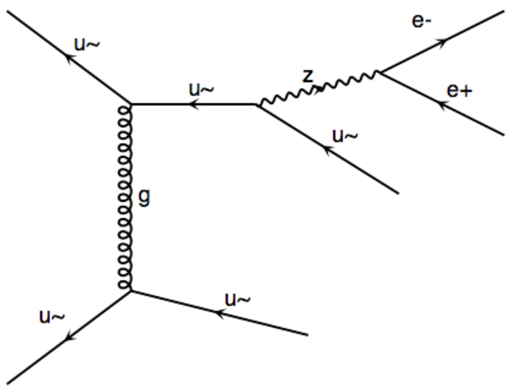


(b)

Figure 1.10: One of the probable decay modes for WZ+jet(s) decaying to $3\ell$ + 1 jet + 1 $\nu$ final state (a) and Z+$u\bar{u}$ (b).

More precisely this is the general case for electrons, while reconstructed muons in these processes, in addition to those from the Z and W decay, mainly comes from decay in fight of light primary hadrons.

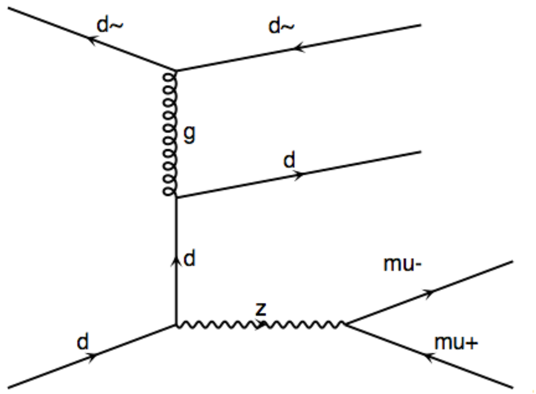


(a)

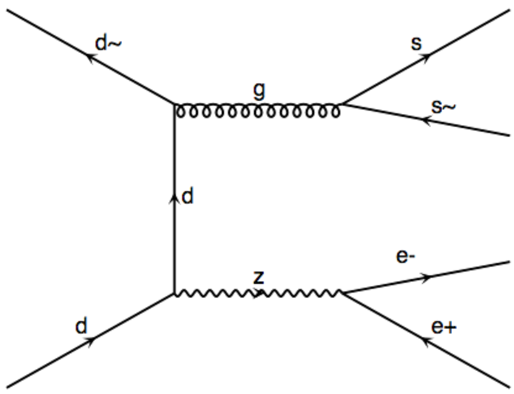


(b)

Figure 1.11: Probable decay modes for Z+$d\bar{d}$ (a) and Z+$s\bar{s}$ (b).

# Chapter 2

# Experimental Apparatus

The Large Hadron Collider, LHC [13, 14] has been built by using the existing LEP tunnel at CERN under French and Swiss territory, to carry on research in fundamental physics. This machine is an excellent scientific and technical milestone towards understanding nature and the SM Higgs physics. It is the largest circular collider and the highest energy particle accelerator ever built because a large amount of energy is required in order to produce heavier fermions, which can couple stronger with the Higgs boson or can boost its production.

## 2.1 The Large Hadron Collider

The design of the LHC started in 1981, but the project was not approved by CERN council until December 1994. The building and commissioning of the LHC was a huge technological effort. The magnitude of the experiment, the biggest ever built, caused some unpredictable delays and during fifteen years the design has considerably evolved and matured but the original idea stayed untouched. In the years to come, LHC will reach its design energy and luminosity, and particle physics will enter new territories that have never been explored before by previous colliders. The total integrated luminosity delivered by LHC in different time spans since beginning is shown in Fig. 2.1 & 2.2.

The LHC started providing $p\bar{p}$ collisions on 23 November 2009, at the centre-of-mass energy of $\sqrt{s} = 900$ GeV. This energy was then raised to $\sqrt{s} = 2360$ GeV and later, on 30 March 2010, the first collisions at a centre-of-mass energy of 7 TeV, the highest ever reached at a particle collider, were recorded by the four experiments [15]: ALICE, ATLAS, CMS and LHCb.

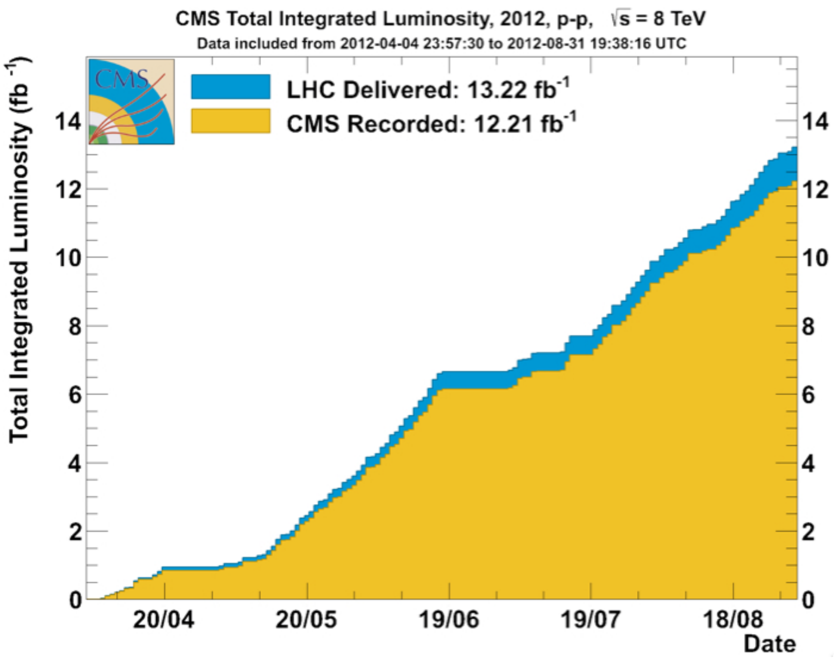


Figure 2.1: Integrated luminosity versus time delivered to, and recorded by CMS (see Sec. 2.2) during stable beams for *pp* running at 8 TeV centre-of-mass energy.

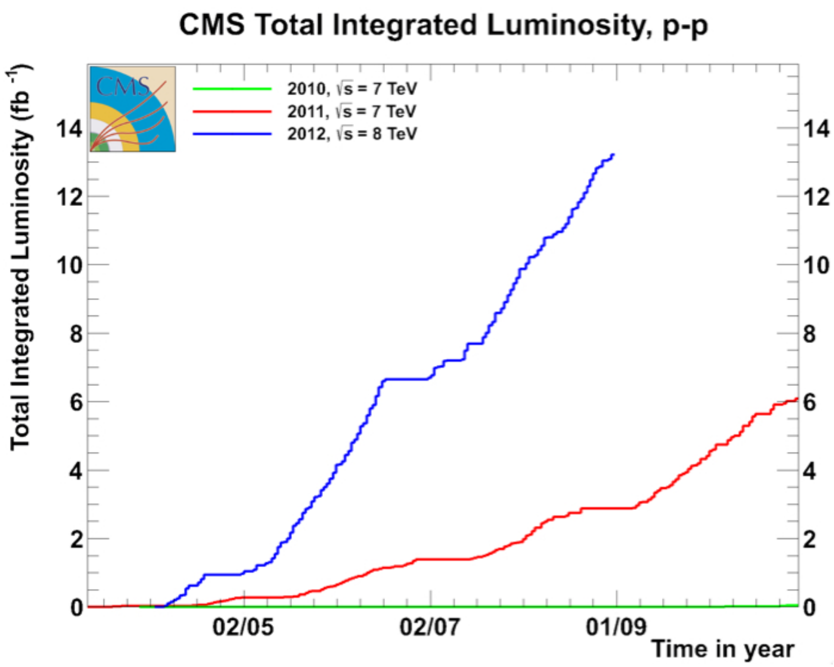


Figure 2.2: Total integrated luminosity vs. time since the startup of the LHC.

### 2.1.1 The LHC design concept

The accelerator complex of LHC as shown in Fig. 2.3, is composed of various small accelerators that deliver two particle beams, running in opposite directions at increasing energies until they reach the main LHC accelerator ring. It was designed to provide proton-proton collisions with a center-of-mass energy of 14 TeV and a luminosity of $10^{34}$ $cm^2s^{-1}$. It will also provide heavy ion collisions (Pb) with a center-of-mass energy of more than 1000 TeV and a luminosity exceeding $10^{27}$. A summary of the machine parameters is given in Tab. 2.1 and detail can be find in Ref. [15]. The numbers indicated correspond to the nominal values.

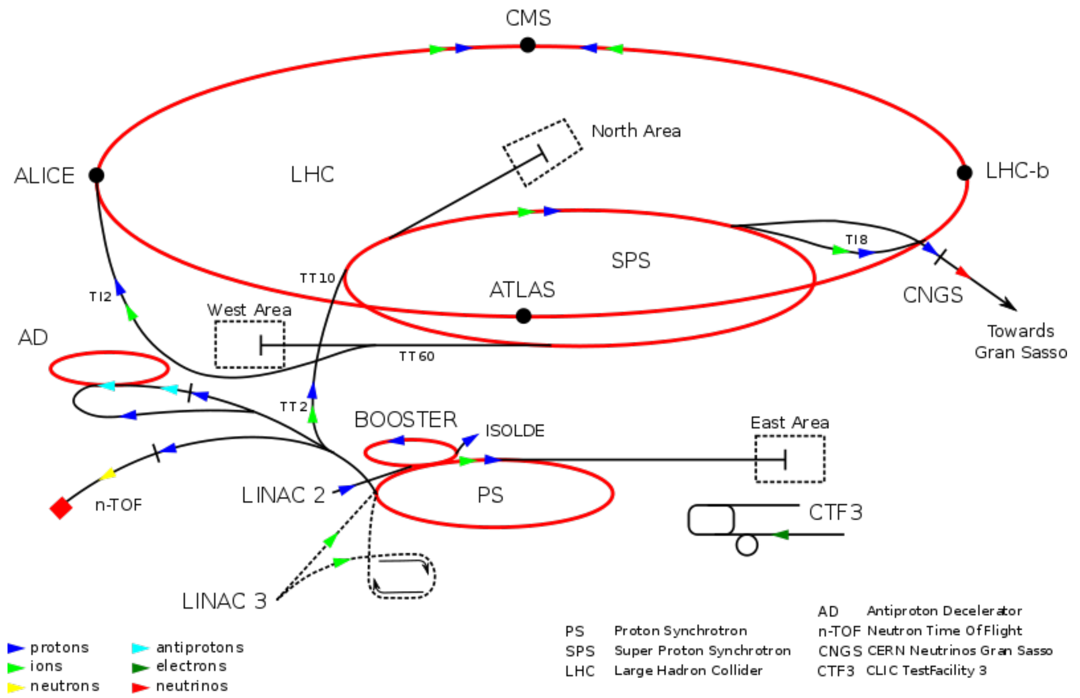


Figure 2.3: A schematic diagram of the LHC accelerator complex is shown. Protons are first accelerated in the linear accelerator (LINAC), and transferred to the Booster where they are accelerated to a kinetic energy of 1.4 GeV. Next, they enter the proton synchrotron (PS) ring, arranged into bunches, and accelerated to 25 GeV. Then, they are transported to the super proton synchrotron (SPS), where they are accelerated to 450 GeV and finally injected into the LHC.

Table 2.1: Design parameters of the Large Hadron Collider.

| Large Hadron Collider | |
|---|---|
| circumference | 26659 m |
| depth | 50 - 175 m |
| total number of magnets | 9600 |
| number of main dipoles | 1232 |
| number of quadrupoles | 392 |
| temperature | 1.9 K (-271.3 C) |
| beam vacuum pressure | $10^{-13} atm$ |
| nominal p energy | 7 TeV |
| center-of-mass energy | 14 TeV |
| design luminosity | $10^{34}\ cm^2 s^{-1}$ |
| bunches per proton beam | 2808 |
| protons per bunch | $1.1\ \times 10^{11}$ |
| turns per second | 11245 |
| collisions per second | 600 milions |
| length of each dipole | 15 m |
| weight of each dipole | $\approx 35\ t$ |
| dipole field | 8.33 T |

#### 2.1.1.1 LHC Collision Detectors

The detectors are installed in the collision points all around the LHC ring. There are six experiments installed at the LHC, in alphabetical order: ALICE (A Large Ion Collider Experiment), ATLAS (A Toroidal LHC Apparatus), CMS (Compact Muon Solenoid), LHCb (Large Hadron Collider beauty), LHCf (Large Hadron Collider forward) and TOTEM (TOTal Elastic and diffractive cross-section Measurement).

ALICE, ATLAS, CMS and LHCb are installed in four huge underground caverns build around the four collision points of the LHC, while LHCf and TOTEM are close to the main detectors, ATLAS and CMS respectively. ATLAS and CMS are the main experiments in the LHC, made for general purposes with the same physics goals but different technical solutions and design; the rest of the experiments are smaller and specialized in different topics.

This thesis have been realized in context of the CMS experiment. The main details about the CMS detector will be discussed in the following sections.

### 2.1.2 Performance Goals and Constraints

The LHC is designed to reach a center of mass energy up to 14 TeV. For any physics process the number of events generated by the LHC collisions is given by:

$$N_{event} = \mathcal{L}\sigma_{event} \tag{2.1}$$

where $\mathcal{L}$ is the instantaneous machine luminosity and $\sigma_{event}$ is the production cross section for this specific physics process. The machine luminosity depends on the beam parameters and for a Gaussian distributed beam is given by:

$$\mathcal{L} = F\frac{N_b^2 n_b f_{rev}\gamma_r}{4\pi\epsilon_n\beta*} \tag{2.2}$$

where $F$ is the geometric luminosity reduction factor due to the crossing angle at the interaction point (IP), $N_b$ is the number of particles per bunch, $n_b$ is the number of bunches per beam, $f_{rev}$ represents the revolution frequency, $\gamma_r$ is relativistic gamma factor, $\epsilon_n$ the normalized transverse beam emittance and $\beta*$ is the beta function at the collision point. The beam emittance and the $\beta*$ are determined from the single particle transverse motion described by the equation:

$$x(s) = A\sqrt{\beta(s)}cos[\psi(s)+\delta] \tag{2.3}$$

where $s$ is the path along beam direction and $A, \delta$ are constants of integration defined by boundary conditions. The amplitude function, $\beta$, describes the amplitude of the motion in the beam line. The phase depends on $\beta$ and advances as $d\psi/ds = 1/\beta$. The amplitude function at the IPs, where magnets are configured to focus the beams is designated as $\beta*$. The number of transverse oscillations per rotation is denoted as the tune ($\nu$). The phase space of the motion in the transverse plane is described by an ellipse in the $(x, x')$ plane where $x' = dx/ds$. This ellipse has a total area of $\pi A^2$. If we consider a particle ensemble populating the phase space, we define as emittance the area populated by this particle ensemble. This area depends only on the beam energy. For a Gaussian one dimensional beam, the emittance is defined as :

$$\epsilon = \pi\frac{\sigma^2}{\beta} \tag{2.4}$$

The geometric luminosity reduction factor is given by:

$$F = \left(1+\left(\frac{\theta_c\sigma_z}{2\sigma*}\right)^2\right)^{-1/2} \tag{2.5}$$

where $\theta_c$ is the full crossing angle in the IP, $\sigma_z$ is the RMS bunch length and $\sigma*$ the transverse RMS beam size at the IP. The LHC is designed to operate at a maximum luminosity of the order of $\mathcal{L} = 10^{34} cm^{-2} s^{-1}$. That implies nominal operation with large number of bunches (2,808 per beam) and bunch crossings spaced by 25 ns. To reach this luminosity, very large proton density is required. Therefore, proton-proton beams are used providing the highest beam currents.

The limitations to the maximum instantaneous luminosity come from several factors. The particle density per bunch is mainly limited by the non-linear beam-beam interactions between particles when beams collide with each other. Beam-beam interactions result in modification of the tune of the particles. which is expressed via the linear tune shift given by:

$$\xi = \frac{N_b r_p}{4\pi\epsilon_n}. \tag{2.6}$$

In this equation, $r_p$ is the classical radius of the proton ($r_p = e^2/4\pi\epsilon_0 m_p c^2$). The linear tune shift should not exceed 0.015 when summed over all IPs in the machine. Another parameter that affects luminosity is the mechanical aperture which is given by the beam screen dimensions. The beam screen in the LHC has a width of 2 $\times$ 22 mm and a height of 2 $\times$17.3 mm. Setting the aperture at $10\sigma$ in terms of the RMS beam size and accounting for imperfections in design and alignment results in a maximum nominal beam size of 1.2 mm. Combined with a maximum $\beta$-function of 180 m in the arcs, this implies a maximum emitance of $\epsilon = 3.75\ \mu m$. This parameter in combination with the linear beam-beam tune shift, limits the particle density to $N_b = 1.15 \times 10^{11}$.

Furthermore, the mechanical aperture limits the $\beta*$ value at the IPs resulting in lower peak luminosity. Other design parameters that affect the peak luminosity are related to the maximum dipole field, the maximum energy that can be stored in the machine, the heat load, the quality of the magnetic field and the beam instabilities due to electromagnetic interactions between particles and the conducting boundaries of the vacuum. The dipole field corresponding to a beam energy of 7 TeV is 8.33 T. However, the operating dipole field depends on the heat load and temperature margins inside the cryo-magnets and therefore on beam losses, causing high dipole field to require very low beam losses during operation. *Heat load* refers to heat deposition that is absorbed by the cryogenic system and it is usually due to energy losses and synchrotron radiation. Synchrotron radiation is given by Larmors formula:

$$P = \frac{1}{6\pi\epsilon_0} \frac{e^2 \alpha^2}{c^3} \gamma^4. \tag{2.7}$$

where $\alpha$ is the centripetal acceleration. Although the LHC is a proton collider, 7 kW have to be removed at 1.8K around the ring due to heating from synchrotron radiation which is an experimental challenge for the LHC.

Other parameters that limit the peak luminosity are related to the operation of the machine. The most important metric for LHC Physics program is the integrated luminosity for a run which is defined as:

$$\mathcal{L}_{int} = L_0 \tau_L [1 - e^{-T_{run}/\tau_L}] \tag{2.8}$$

where $L_0$ is the initial instantaneous luminosity, $\tau_L$ is the net luminosity lifetime and $T_{run}$ is the total length of the luminosity run. The luminosity lifetime depends on collisions that can degrade the beam and other effects like beam-beam interactions, radiation and scattering of particles in the residual gas. The average design luminosity lifetime for LHC is

$$\tau_L = 14.9\ h \tag{2.9}$$

The LHC is designed for long term operation. It will operate for about 200 days per year. One significant parameter for high integrated luminosity is the turn-around time, which is the time from the end of the run to the beginning of a new one. Ideally this time is about 1.15 hr due to magnet hysteresis, however experience in the operation of LHC and other accelerators has shown that a more realistic value is of the order of 7 hr. All those parameters limit the maximum integrated luminosity that the LHC provides in design conditions to 80 to 120 $\text{fb}^{-1}$ per year.

## 2.2 The CMS detector

The CMS detector has been built to reconstruct precisely the final states including muons, electrons, photons and jets, which will lead towards detection or exclusion of the SM Higgs boson and discovery of new physics. Neutrinos and other very weakly interacting particles escape without leaving signals, they can only be measured indirectly through the determination of missing transverse energy, which requires a hermetic detector. Therefore CMS must cover the solid angle as much as possible. For this purpose, new forward detectors have been added to the original CMS design.

The structure of the CMS detector is sketched in Fig. 2.4. Two endcaps close a cylindrical barrel part. The overall diameter is 14.6 m, the length 21.6 m, the weight about 12500 tons. The thickness of the electromagnetic calorimeter, expressed in radiation lengths, is larger than 25 $X_0$, while the one of the hadronic calorimeter, expressed in interaction lengths[1], ranges from 7 to 11 $\lambda_1$ depending on $\eta$.

The CMS cartesian coordinate system is a right-handed reference frame with the x-axis pointing towards the centre of the LHC ring, the y-axis pointing upwards and the z-axis parallel to the beam. The origin is located at the nominal interaction point. In this reference frame, let the quadri-momentum of a particle be $(E, p_x, p_y, p_z)$. The longitudinal momentum is $p_z$, the transverse momentum is $p_T = \sqrt{p_x^2 + p_y^2}$. The rapidity is defined as:

$$y = \frac{1}{2} \cdot ln \left( \frac{E + p_z}{E - p_z} \right) \tag{2.10}$$

If a particle is ultra-relativistic ($p \gg m$), its rapidity can be approximated by the pseudo srapidity $\eta$, defined as:

$$\eta = -ln \left( tan \frac{\theta}{2} \right) \tag{2.11}$$

$\theta$ being the angle between the $+z$ semi-axis and the particle momentum vector $\vec{p}$.

From the interaction point outwards, the CMS layout can be described as an '*onion-like*' sequence of subdetectors as shown in Fig. 2.4. The innermost one is the Inner Tracking System (see Sec. 2.2.1), made up of a silicon pixel vertex detector and of a silicon strip tracker. The former has 3 layers in the barrel and 2 disks in each endcap, the latter consists of 10 layers in the barrel region and 12 disks in the endcaps. The main goal of the tracker is the precise reconstruction of the position of primary and secondary vertices and the accurate measurement of the impact parameter of charged tracks. This is possible even in the case of a high track multiplicity, because of the very fine segmentation of the sensors.

The electromagnetic calorimeter (ECAL) (see Sec. 2.2.2) is located outside of the tracker volume. It is a homogeneous detector consisting of lead tungstate ($PbWO_4$) scintillating crystals that are read out by avalanche photo diodes or vacuum phototriodes. Its aim is the precise measurement of the energy and position of electrons and photons. The pseudo-rapidity coverage reaches $|\eta| < 3.0$. In the endcap region, a lead/silicon pre-shower detector is installed in front of ECAL in order to improve the resolution of electron and photon direction measurements and to help discriminate between photons and neutral pions. The hadronic calorimeter (HCAL)

[1]Nuclear interaction length is defined as the mean path length in which the energy of relativistic charged hadrons is reduced by the factor of $1/e$ as they pass through matter.

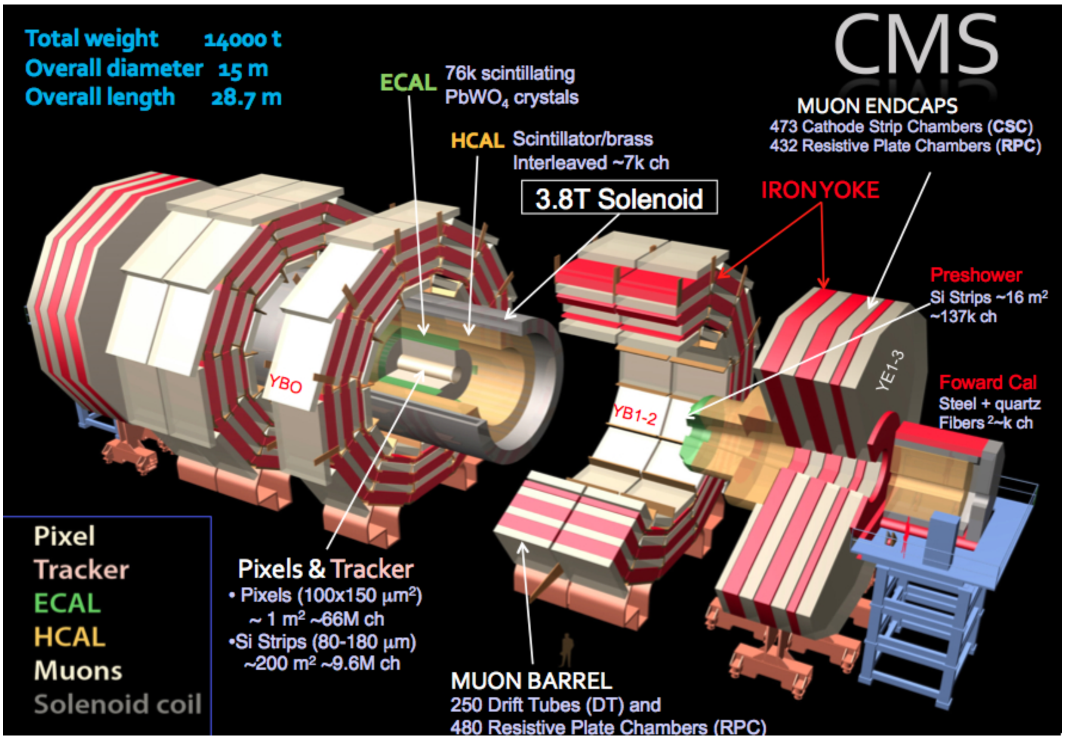


Figure 2.4: An overview of the CMS detector.

(see Sec. 2.2.3) surrounds ECAL. It is a sampling calorimeter consisting of brass absorber plates interspersed with scintillator layers. It is designed to reconstruct energy and position of hadrons and jets. The barrel (HB) and endcap (HE) parts have the same $\eta$ coverage as ECAL, while a very forward calorimeter (HF) extends up to $|\eta| = 5.3$.

A superconducting solenoidal magnet (CB) encompasses all of these subdetectors. It is 13 m long, its diameter is 5.9 m and it provides a uniform magnetic field of 3.8 T. It is cooled with liquid helium. The muon spectrometer is embedded in the iron return yoke (YB, YE) of the magnet. Drift tube (DT) detectors are installed in the barrel region, cathode strip chambers (CSC) in the endcaps, and resistive plate chambers (RPC) are placed both in the barrel and in the endcaps to increase the robustness of the muon trigger system and to provide bunch-crossing timing measurements. The overall pseudo-rapidity coverage of the muon detectors is $|\eta| < 2.4$.

Fig. 2.5 describes the interactions of various kinds of particles with the CMS subdetectors. Muons with sufficient transverse momentum ($p_T > 3$ GeV) can cross the entire detector and their tracks are reconstructed both in the inner tracker and

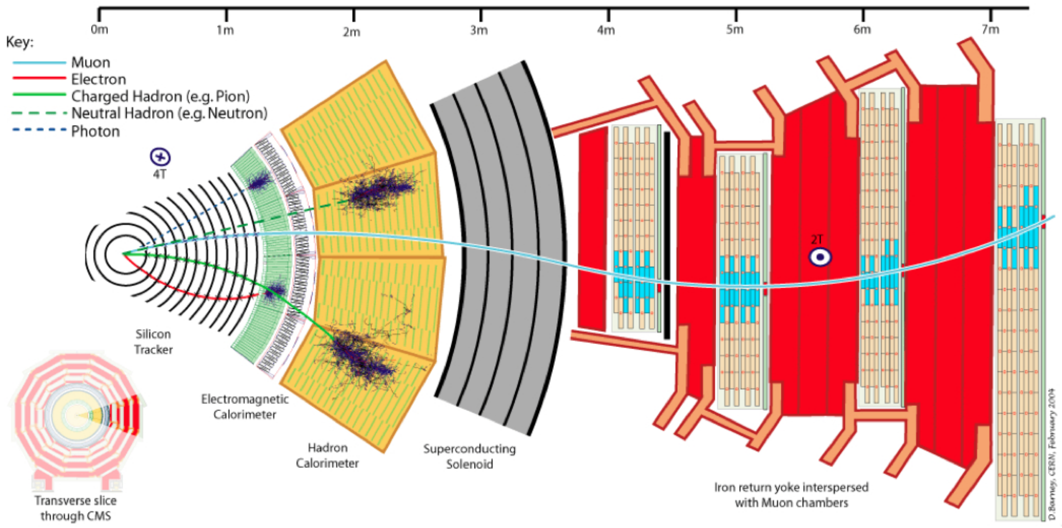


Figure 2.5: The CMS detector's transverse section.

in the muon chambers. They behave as minimum ionizing particles (MIPs) in the calorimeters, *i.e.* they deposit little energy (few hundreds of MeV) in them.

Electrons and photons loose all their energy in the ECAL crystals, producing electromagnetic showers. Electrons are charged particles, therefore their tracks are reconstructed in the tracker, unlike photons. Hadrons such as pions or neutrons produce large showers in the calorimeters. Unless they are very energetic, they release all their energy before reaching the muon chambers.

Details about the subdetectors and the online selection system are presented in the succeeding sections.

### 2.2.1 Inner Tracking System

The inner tracker is designed to reconstruct tracks of charged particles with high efficiency and momentum resolution and to allow the reconstruction of secondary vertices. It has a length of 5.8 m and a diameter of 2.5 m around the interaction point. It covers a pseudorapidity range of $|\eta| < 2.5$. Since it is located directly around the collision point, the tracker material must be very resistant to radiation. The trajectory of a particle with transverse momentum $p_T$ and charge $q$ moving through a magnetic field of strength B is a helix of radius R. These quantities are related by the following formula:

$$p_T[GeV] = 0.3 \cdot q \cdot B[T] \cdot R[m] \quad (2.12)$$

The transverse momentum resolution is given by:

$$\frac{\delta p_T}{p_T} = C_1 \otimes p_T C_2 \tag{2.13}$$

The term $C_2$ contains the multiple coulomb scattering effects, whereas $C_1$ depends on the detector geometry, in particular on the number of points (n) used to reconstruct a track, on its length (L) and on the resolution on the single point measurement ($\sigma_x$):

$$C_1 \propto \frac{\sigma_x}{\sqrt{n} \cdot B \cdot L^2} \tag{2.14}$$

The $C_2$ term is dominant for low energy particles. $C_1$ is minimal for tracks made of many hits and traveling a long path within the tracker volume. The single-point resolution $\sigma_x$ can be expressed as

$$\sigma_x = \sqrt{\sigma_{int}^2 + \sigma_{syst}^2} \tag{2.15}$$

where $\sigma_{int}$ is the intrinsic detector resolution and $\sigma_{syst}$ is the systematic error associated to the uncertainty on the exact position of a hit module.

The very fine granularity in the innermost part is an essential feature for the identification of the different vertices in a bunch crossing. While the primary vertex corresponds to the interaction point of the collision, secondary vertices can indicate other interactions that can occur during the same bunch crossing (pile-up), or the presence of long-live particles[2].

The tracker is composed by two subsystems: a silicon pixel detector in the innermost part, closest to the beam pipe, and a silicon strip detector of overall radius r = 1.1 m. The total coverage in pseudorapidity is -2.5< $\eta$ <2.5. The subdetectors are briefly discussed in following sections.

#### 2.2.1.1 The Silicon Pixel Detector

The pixel detector is the detector located nearest to the interaction point and faces very large particle flux in this region. The pixel tracker is composed of n-type silicon pixels laying on an n-type silicon substrate. The pixels are organized in modular detector units, called *modules*, and connected to read-out chips (ROC) by Indium

[2]Leptons coming from late decays indicate a background event in the $H \rightarrow ZZ^* \rightarrow 4\ell$, where $\ell = e, \mu$

bump-bonds. It contributes precise tracking points in $r$, $\phi$, z and therefore responsible for a small impact parameter resolution that is important for good secondary vertex reconstruction. The pixel system has a zero-suppressed analog pulse height read-out scheme that improves position resolution and helps separating signal and noise hits as well as identifying large hit clusters from overlapping tracks. To achieve this resolution, a pixel cell size of 100×150 $\mu m^2$ is utilized and the total number of pixels is 47923200 in the barrel, 17971200 in the endcaps.

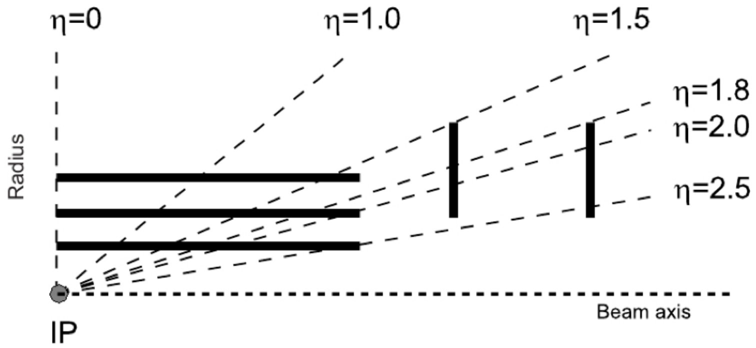


Figure 2.6: Hit coverage of the Silicon pixel detector.

The layout of the pixel system is shown in Fig. 2.6, where it consists of three layers of pixel modules placed at radii of 4.4, 7.3 and 10.2 cm and two endcap discs extending from 6 to 15 cm in radius placed at 34.5 cm and 46.5 cm from the nominal interaction point. The pseudorapidity range covered is -2.5< $\eta$ <2.5 and the arrangement of the barrel layers and endcap disks ensures the existence of three measurement points almost over full covered range.

#### 2.2.1.2 The Silicon Strip Tracker

The particle flux is much lower outside the pixel detector so silicon micro-strip detectors are utilized. The silicon strip tracker (SST) is displayed in Fig. 2.7 and consists of three different sub-systems and 10 layers of silicon microstrip detectors. The tracker inner barrel and disks (TIB/TID), extending in a radius of 55 cm, are composed of four barrel layers and three disks at each end. The SST provides up to 4 $r-\phi$ measurements with a position resolution of 23 $\mu m$ in the two inner layers and 35 $\mu m$ in the two outer layers. The TIB and TID are surrounded by the tracker outer barrel system (TOB). TOB consists of 6 barrel layers, providing a resolution of 53 $\mu m$ in the first four layers and 35 $\mu m$ for the two outer layers.

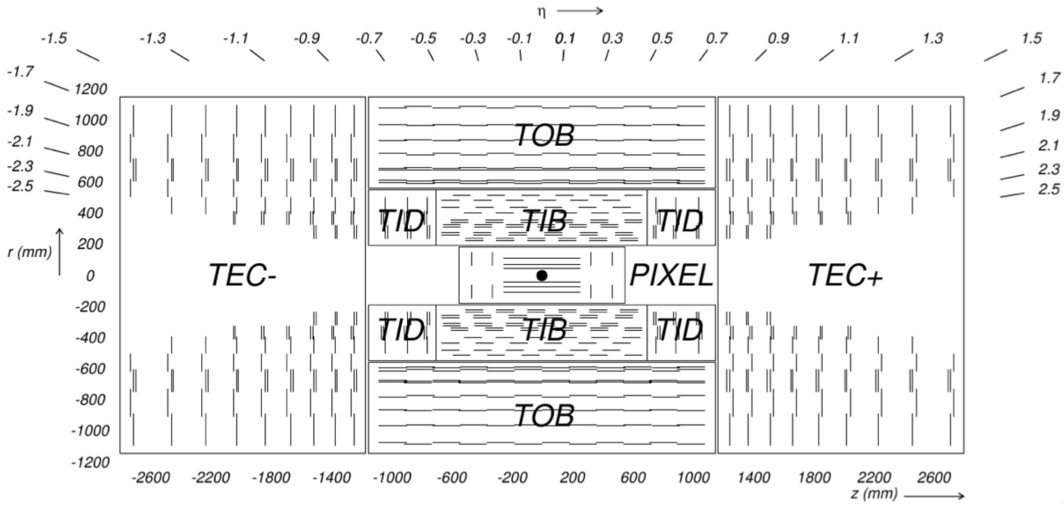


Figure 2.7: Schematic cross section of the CMS silicon tracker. Each line corresponds to a detector module while double lines correspond to back to back modules.

It extends up to z = 118 cm and beyond this z range, the tracker endcaps (TEC+,TEC-) provide the additional forward coverage up to $\eta$ <2.5. Each TEC provides 9 $\phi$ measurements per trajectory and extends to z = 282 cm. In addition the first two layers of TIB/TID and TOB, as well as rings 1, 2 and 5 of the TEC, carry a second micro-strip module with sensors in both sides with an angle of 100 mrad in order to provide a measurement of the second coordinate $z$ or $r$ in the barrel and discs respectively. Both sub detectors have wedge shaped modules arranged in rings, centered on the beam line, with strips pointing towards the beam line.

### 2.2.2 Electromagnetic Calorimeter

The calorimeters measure the energy of both neutral and charged particles. Electrons, positrons and photons deposit all their energy through electromagnetic interactions, by producing showers in the innermost calorimeter *i.e.* ECAL. It is a hermetic homogeneous calorimeter, made of 61200 lead tungstate (Pb$WO_4$) crystals mounted in the central barrel part accompanied by 7324 crystals in each of the two endcaps.

The layout of the CMS ECAL is presented in Fig. 2.8 & 2.9. A preshower detector is installed at the face of each of the two endcaps. Avalanche photo-diodes

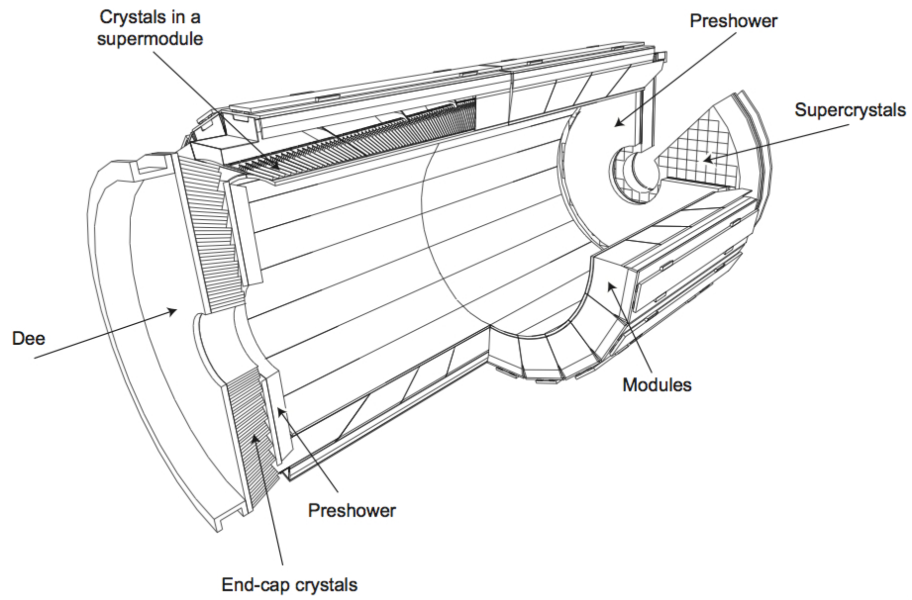


Figure 2.8: Layout of the CMS ECAL showing the arrangement of crystals, supermodules and endcaps with the preshower in front.

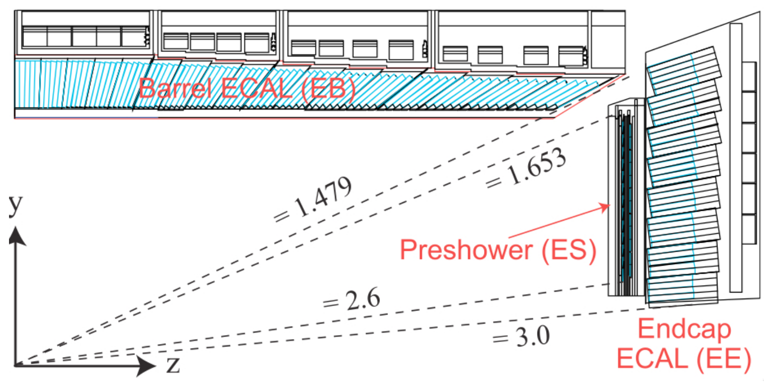


Figure 2.9: A schematic cross sectional diagram of the ECAL, showing the geometrical arrangement of the barrel ECAL, the endcap ECAL, and the preshower detector. The interaction point is located at the lower left edge of the diagram. The dotted lines show the values of the pseudorapidity at the given angle.

(APDs) are used as photo-detectors in the barrel and vacuum photo-triodes (VPT) in the endcaps.

The choice of high density crystals allowed CMS to build a compact calorimeter which provides fast response, high granularity and good energy resolution. The design of the electromagnetic calorimeter is motivated by the search for Higgs bosons in the di-photon final state where optimal position and energy resolution for photons is essential for Higgs discovery.

#### 2.2.2.1 Lead Tungstate Crystals

The choice of the material for crystals is very important for the performance of an electromagnetic calorimeter. For precise measurement of the energy, leakage outside the crystals has to be minimized. This is achieved by choosing a crystal material with low radiation length and molière radius. Lead tungstate crystals provide a radiation length of 0.89 cm and their high density leads to a compact design resulting in 25.8 radiation lengths in 23 cm crystals. The position resolution is optimized by requiring small transverse size of the electromagnetic shower.

The transverse profile of electromagnetic showers is expressed by the Molière radius[3] About 90% of the electromagnetic energy of a shower lies within a cylinder with radius equal to RM . The Molière radius of the lead tungstate crystals is 2.2 cm and combined with a barrel crystal front face of 2.2×2.2 cm$^2$ ensures that the core of the shower will be included in a 2×2 crystal area. Lead tungstate provides optimal scintillation time since about 80% of the light is emited in 25 ns which is the nominal beam crossing time separation.

#### 2.2.2.2 Calorimeter Resolution

For energies of electromagnetic showers below 500 GeV, where energy leakage from the end of the calorimeter is negligible, the resolution of the electromagnetic calorimeter can be modeled in three terms:

$$\left(\frac{\sigma}{E}\right)^2 = \left(\frac{S}{\sqrt{E}}\right)^2 + \left(\frac{N}{E}\right)^2 + C^2, \tag{2.16}$$

[3]The Molière radius $R_\mu$ (RM ) is a characteristic constant of a material, giving the scale of the transverse dimension of the fully contained electromagnetic showers initiated by an incident high energy electron or photon. It is defined as the mean deflexion of an electron of critical energy after crossing a width $1X_0$, where $X_0$ is defined as the radiation length, i.e. the average distance covered by an electron in a material through which it loose a fraction of its energy equal to $1/e$. A cylinder of radius $R_\mu$ contains on average 90% of the shower's energy deposition.

where S is the stochastic term, N is the noise term and C is constant term. The stochastic term describes statistics related fluctuations such as intrinsic shower fluctuations, photoelectron statistics, dead material in front of the calorimeter and sampling fluctuations.

The main contribution to the constant term C are detector non-uniformity, calibration uncertainty, radiation damage to the calorimeter and leakage from the outside of a crystal. The constant term can be reduced by utilizing radiation hard media and performing in-situ calibration. The CMS calorimeter accounts for both factors by utilizing a laser monitoring and calibration system.

The noise term is related to the electronics noise and estimated by measuring the contribution from electronics noise after summing over some Molière radii. One additional noise factor can come from pile-up where remnant energy from a previous crossing can be accounted in the measurement. The values of these three constants, measured with test beams, are listed in Tab. 2.2.

Table 2.2: Contributions to the energy resolution of ECAL.

| Contribution | Barrel ($\eta = 0$) | Endcap ($\eta$ =2) |
|---|---|---|
| Stochastic term | 2.7% | 5.7 % |
| Constant term | 0.55 % | 0.55% |
| Noise (low luminosity) | 0.155 GeV | 0.155 GeV |
| Noise (high luminosity) | 0.210 GeV | 0.245 GeV |

The crystals response depends strongly on their temperature, which must therefore be kept constant as a function of time. This is obtained with a cooling system capable of collecting the heat dissipated by the read-out electronics and of ensuring thermal stability. The nominal ECAL operating temperature is $18^o$.

### 2.2.3 The Hadron Calorimeter

The hadron calorimeter (HCAL) plays a major role in the detection of hadron jets, especially the neutral ones since pions and kaons are detected by also estimating their momenta with the silicon tracker. In addition, for adequate measurement of the missing transverse energy, hermetic coverage is needed up to $|\eta|$ <5. The CMS HCAL is a brass/scintillator sampling calorimeter. It is mostly installed between the ECAL and the solenoid magnet while its small part is installed outside the magnet and it consists of four different subsystems:

- **Barrel Hadron Calorimeter (HB):** located between ECAL barrel and the magnet covering up to $|\eta|$ <1.4.

- **Endcap Hadron Calorimeter (HE):** located inside the magnet, consisting of two endcaps complementing HB and extending the coverage up to $|\eta|$ <3.0.

- **Outer Hadron Calorimeter (HO):** located outside the magnet, in the barrel using the magnet as additional absorber providing the additional absorber length required for the barrel region.

- **Forward Hadron Calorimeter (HF):** placed 11.2 m from the nominal interaction point extending the coverage from $|\eta|$ >3 up to $|\eta|$ <5.2.

The layout of the CMS HCAL is displayed in Fig. 2.10. The length scale of hadronic calorimetry is designated as the interaction length ($\lambda_I$ )[4]. The HB absorber consists of a 40 mm thick front steel plate, followed by eight 50.5 mm thick brass plates, six 56.5 mm thick brass plates and a 75 mm thick steel plate. The total absorber thickness at incident angle of $90^o$ is $5.82\lambda_I$ while at $\eta = 1.3$ it is $10.6\lambda_I$. The electromagnetic calorimeter adds about 1.1 $\lambda_I$ of additional material.

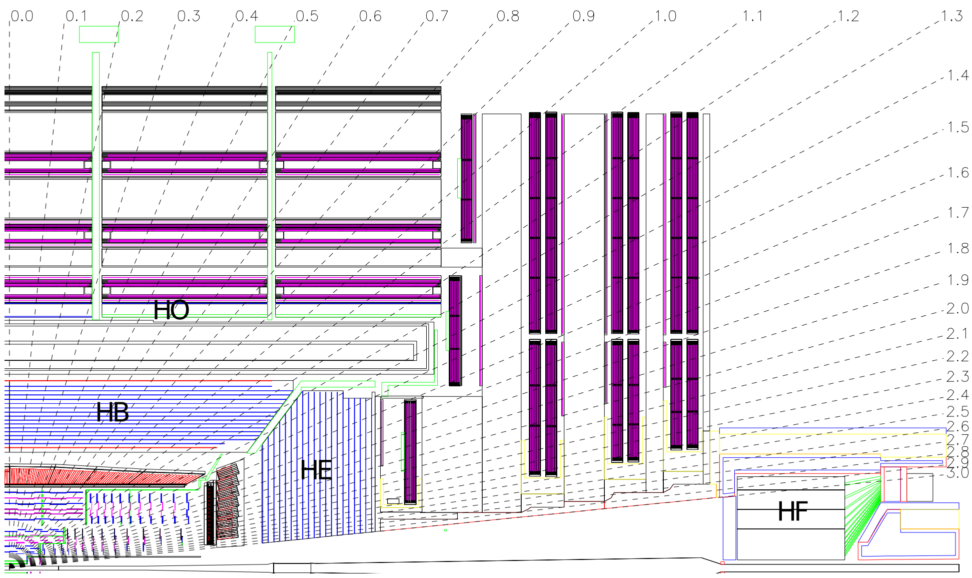


Figure 2.10: Longitudinal view of the CMS detector. The locations of the hadron barrel (HB), the endcap (HE), the outer (HO) and the forward (HF) calorimeters.

[4]Nuclear interaction length is defined as the mean path length in which the energy of relativistic charged hadrons is reduced by the factor of $1/e$ as they pass through matter.

The endcap part uses the same absorber but the plates have a thickness of 79 mm. The plastic scintillator tiles are placed between the absorber layers, resulting in 70000 tiles for the whole detector. The granularity of the tiles corresponds to $\Delta\eta \times \Delta\phi$ of 0.087×0.087 in the range of $|\eta| < 1.6$ and 0.17×0.17 in the region of $|\eta| > 1.6$. The HO utilizes the magnet as additional absorber corresponding to an additional $1.4\lambda_I$ of material at normal incidence and it consists of two scintillator layers with the same granularity as HB. The total depth in the central region sums to about $11.8\lambda_I$.

The light produced in the HB scintillators is transferred to the hybrid photo diodes (HPDs) via optical fibers. HPDs consist of a photo-cathode held at a HV-8 kV at a distance of approximately 3 mm from a pixelated silicon photo-diode and can provide a gain of 2000. The forward calorimeter (HF) design is very challenging, since in the LHC environment on average 760 GeV of energy are deposited in the forward calorimeters, compared to an average of 100 GeV in the rest of the detector. This flux introduces the need for radiation hard design. CMS opted for a Cherenkov based calorimeter using quartz fibers as an active material embedded in a steel absorber. The signal is generated when charged shower particles above the Cherenkov threshold generate light that is captured by photo-multipliers tubes (PMT). The HF is therefore more sensitive to the electromagnetic showers and some relativistic charged pions.

In contrast to the electromagnetic calorimetry, in case of hadronic calorimetry, the best achievable energy resolution is limited due to the nature of the hadronic interactions. During a hadronic interaction, a part of the energy is purely electromagnetic due to the presence of $\pi^o$ and $\eta$ mesons decaying to photon pairs and it is measured directly by the photo-detectors. Charged particles, on the other hand produce signal by ionization, excitation and nuclear interactions. In most of the cases, a significant fraction of the energy of the order of 20 - 35%, deposited in a sampling calorimeter is not visible resulting in degraded resolution. For the CMS hadronic calorimeter, the resolution is described as:

$$\left(\frac{\sigma}{E}\right)^2 = \left(\frac{99\%}{\sqrt{E}}\right)^2 + (4.5\%)^2, \tag{2.17}$$

for the HB, HO and HE and

$$\left(\frac{\sigma}{E}\right)^2 = \left(\frac{172\%}{\sqrt{E}}\right)^2 + (9.0\%)^2, \tag{2.18}$$

for the HF.

### 2.2.4 CMS Magnet

The CMS superconducting magnet provides a large bending power, allowing a precise measurement of the transverse momentum of charged particles. A further and independent $p_T$ measurement outside the solenoid is possible due to the bending power in the iron yoke. It has been designed to generate a uniform 3.8 T field in the inner region, with a stored energy of 2.6 GJ at full current. The magnet is operated at the temperature of 4 K, as low as to make a flat $NiTb$ cable superconducting and to produce a 20 kA current not subject to any appreciable loss. A vacuum cylinder isolates the magnet from the external environment. A 10000 t return yoke closes the B-field lines. It consists of 5 barrel layers and of 3 disks in each of the two endcaps. The ratio between stored energy and cold mass is large (11.6 KJ/kg), which causes a large mechanical deformation (0.15%) during the ramp-up phase. The parameters of the CMS magnet are summarized in Tab. (2.3).

Table 2.3: A summary of the main features of the CMS magnet.

| **General Parameters** | |
|---|---|
| Eta | Interaction length($\lambda_I$) |
| Magnetic Length | 12.5 m |
| Cold bore diameter | 6.3 m |
| Central magnetic induction | 4 T |
| Total Ampere-turns | 41.7 MA - turns |
| Nominal current | 19.14 kA |
| Inductance | 14.2 H |
| Stored energy | 2.6 GJ |
| **Cold Mass** | |
| Radial thickness of cold mass | 312 mm |
| Radiation thickness of cold mass | 3.9 $X_o$ |
| Weight of cold mass | 220 t |
| Maximum induction on conductor | 4.6 T |
| Temperature margin wrt operating temperature | 1.8 K |
| Stored energy/unit cold mass | 11.6 kJ/kg |
| **Iron Joke** | |
| Outer diameter of the iron flats | 14 m |
| Length of Barrel | 13 m |
| Thickness of the iron layers in Barrel | 300, 630, 630 mm |
| Mass of iron in Barrel | 6000 t |
| Thickness of iron disks in Endcaps | 250, 600, 600 mm |
| Mass of iron in each Endcap | 2000 t |
| Total mass of iron in return yoke | 10000 t |

### 2.2.5 The Muon System

The efficient and precise muon identification is one of the main requirements that influenced the design of CMS detector. Muons have a lifetime of about 2.19 $\times 10^{-6}$s [16], even longer at relativistic speed. Therefore they cross the full detector before decaying. In addition, *bremmstrahlung* is suppressed by a factor of $(m_e/m_\mu)^2$ with respect to electrons for muons below 100 GeV, which implies that the muon does not stop in the calorimeters but rather interacts via ionization. Muons are therefore expected to produce a track in the CMS tracker and then escape the calorimeter by depositing very small energy in it. In addition, for very energetic muons, the tracker cannot provide sufficient momentum resolution. It creates the need of a special muon system outside the calorimeters that can provide identification and momentum measurement.

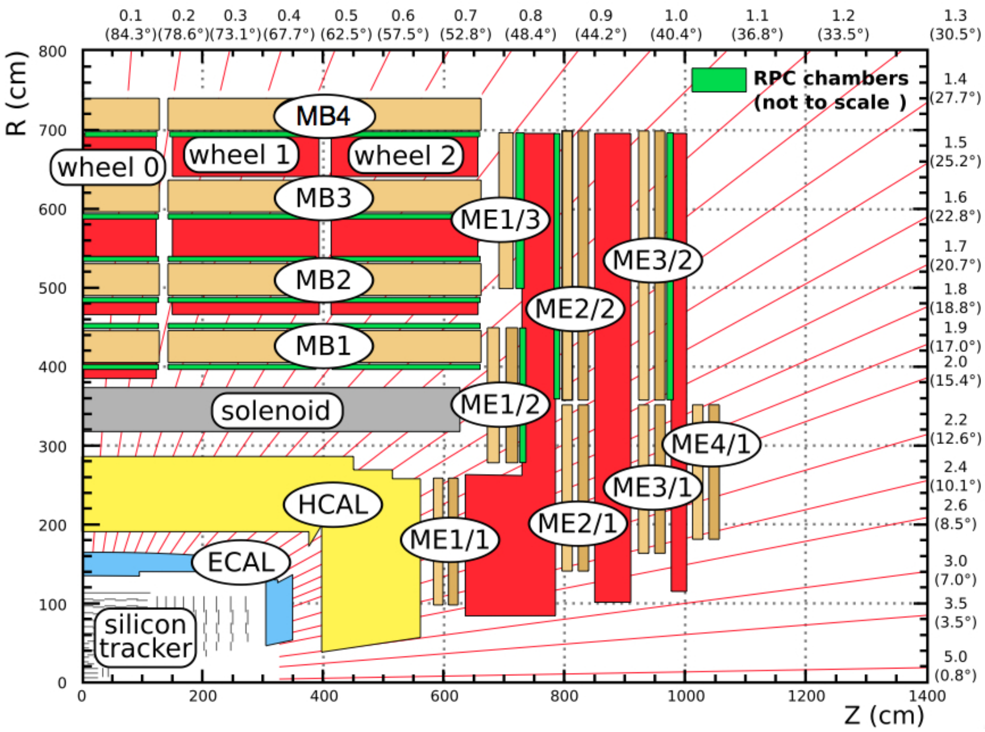


Figure 2.11: An r-z cross-section of a quadrant of the CMS detector with the axis parallel to the beam (z) running horizontally and radius (r) increasing upward. The interaction region is at the lower left corner. Shown are the locations of the various muon stations and the steel disks (red areas). The four drift tube (DT) stations are labeled MB ("muon barrel") and the cathode strip chambers (CSC) are labeled ME ("muon endcap"). Resistive plate chambers (RPC, in green) are in both the barrel and the endcaps of CMS.

The muon spectrometer has been designed to provide an efficient muon trigger and a precise measurement of muon momentum and charge, even without relying on information from the tracking system. Muon detectors are embedded in the iron return yoke of the magnet, as shown in Fig. 2.11. Particles other than muons and even muons with transverse momentum lower than $\simeq 3$ GeV, do not reach the muon chambers. Three subsystems compose the spectrometer are explained below:

#### 2.2.5.1 Drift Tube Chambers

In the CMS barrel, where the muon rate is under control, four layers of muon stations are used, occupied by drift tube (DT) Chambers covering up to $|\eta| <1.2$; where the residual magnetic field and the track occupancy are low. The DTs are divided in five wheels along the z-coordinate, each including 12 azimuthal sectors. Along the radial coordinate, four stations (MB1, MB2, MB3, MB4) are made of 12 chambers each (see Fig. 2.11), one per $\phi$ sector, except for MB4, which contains 14 chambers.

The basic constituent of a DT chamber is a cell, as shown in Fig. 2.12, having size of $42{\times}13$ mm$^2$. A cell is bounded by two parallel aluminium planes and by '$I-shaped$' aluminium beams serving as cathodes. The anodes are 50 $\mu$m stainless steel wires located in the centre of the cells. Muons passing through a cell ionise the gas mixture that fills the cell volume.

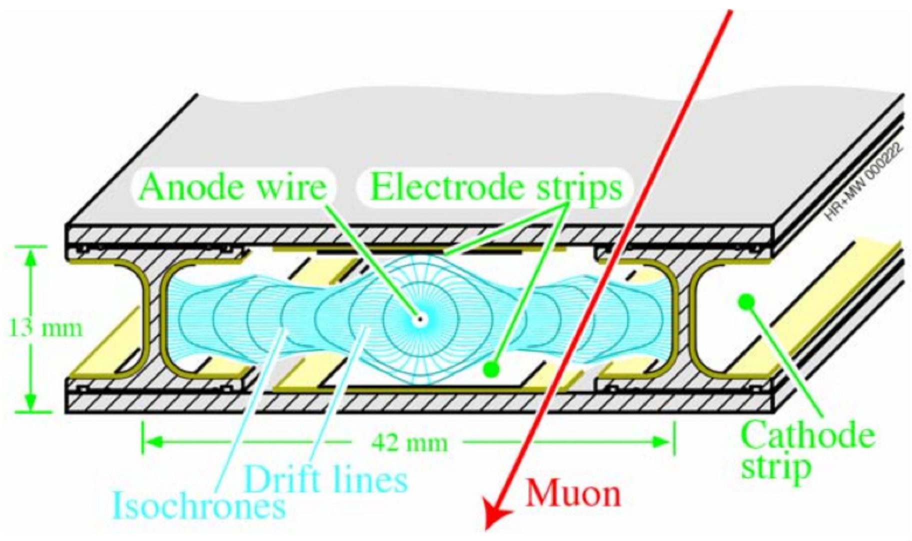


Figure 2.12: The individual drift tube cell and operation principle..

The drift time of the resulting electrons is used to measure the distance between the muon track and the wire. The linearity of relation between time and distance is enhanced by means of an additional field shaping, given by two positively biased insulated strips glued on the planes in correspondence to the wire.

The gas mixture within a cell is composed of Ar (85%) and $CO_2$ (15%). It guarantees good quenching properties and the saturation of the drift velocity, which is $\approx$ 5.4 cm/$\mu$s. This corresponds to a maximum drift time of $\approx$ 390 ns, or 15 bunch crossings. The efficiency of a single cell is $\approx$ 99.8%, its spatial resolution is $\approx$ 180 $\mu$m. Each chamber has a resolution of 100 $\mu$m in the r-$\phi$ plane and of $\approx$ 1 mrad along the $\phi$ coordinate.

#### 2.2.5.2 Cathode Strip Chambers

The cathode strip chambers (CSCs) are installed in the endcaps (see Fig. 2.11), providing full muon coverage up to $|\eta|$ <2.4. The CSCs are multi-wire proportional chambers consisting of six planes of anode wires interleaved among seven cathode panels. Wires run azimuthially, defining the tracks radial component, while strips are equipped on cathode panels and run lengthwise at a constant $\Delta\phi$ width.

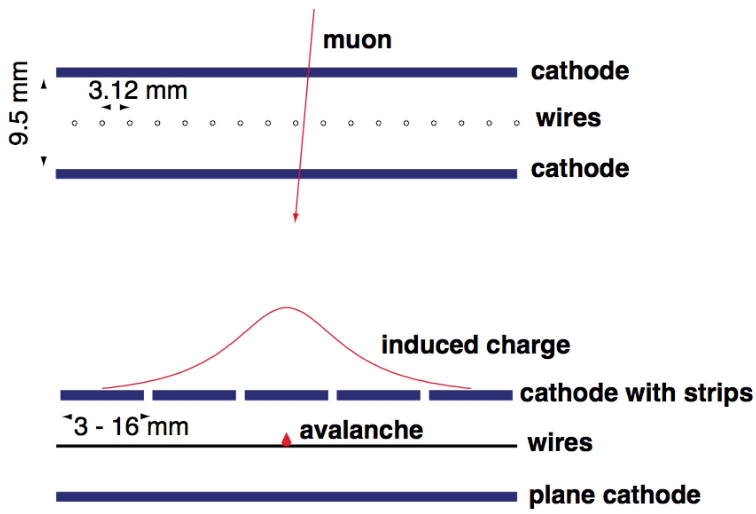


Figure 2.13: Working principle of a CSC chamber.

The angular position $\phi$ of the track is estimated by extrapolating the charge that is induced on the strips as shown in Fig. 2.13. The nominal gas mixture is 40 % Ar, 50 % $CO_2$ and 10 % $CF_4$. The addition of $CF_4$ is used to avoid polymerization of the wires. The wires give very fast signals that provide very good time resolution. A charged track passing through a chamber generates an avalanche that induces a charge on several cathode strips which gives very good position resolution. By interpolating among these strips one reaches a very fine spatial resolution of 50 $\mu$m. The resolution along the $\phi$ coordinate is 10 mrad.

The CSCs consist of four stations (ME1 to ME4) as shown in Fig. 2.11, the innermost one including three concentric rings, the other ones only two. The inner rings of stations ME2 to ME4 contain 18 chambers, all the other ones include 36 chambers. The CSCs can operate at high rates and in large and non-uniform magnetic fields without requiring precise monitoring of gas, pressure or temperature and can provide trigger and precision position measurement in the same device.

#### 2.2.5.3 Resistive Plate Chambers

The resistive plate chambers (RPC) are gaseous parallel plate detectors that combine adequate position resolution with very high speed. RPCs are located both in the barrel and in the endcaps as displayed in Fig. 2.11, which covers $|\eta| <2.1$.

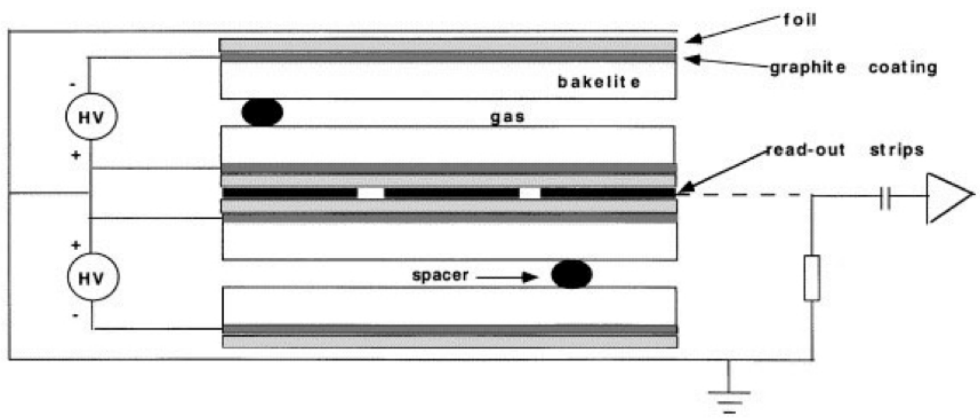


Figure 2.14: A schematic diagram of the RPC double gap chamber.

Their spatial resolution is limited, but their time resolution is very good, about 1 ns, a shorter time than the 25 ns *i.e.* LHC bunch spacing. Therefore RPC detectors are used to identify unambiguously a bunch crossing and to provide prompt trigger decisions. RPCs are made of two parallel plates of bakelite, a high-resistivity plastic material, with a few mm thick gas gap in between them and a graphite coat outside of them and shown in Fig. 2.14. Aluminum strips, separated from the graphite layers by an insulating PET (polyethylene terephtalate) film, read out the signals.

The gas mixture filling the gap consists of $C_2H_2F_4$ (95%) and of i-$C_4H_{10}$(5%). The geometrical layout of the RPC chambers depends on their position. In the barrel region, six layers of RPCs are there: four of them are attached to each side of the MB1 and MB2 DT chambers, the other two to the inner side of MB3 and MB4. In the endcaps, four disks of trapezoidal RPC are attached to the CSCs.

### 2.2.6 Trigger System and Data Acquisition

The trigger system and integrated data acquisition (DAQ) is active in CMS to record data quickly and efficiently. The LHC provides proton collisions at high interaction rates with a designed bunch crossing rate of 40 MHz. Each recorded event in CMS has a nominal size of 0.5 -1MB which makes impossible to store and process this huge number of events.

Therefore, a drastic rate reduction is achieved in real time using the trigger system. In CMS, this is achieved by splitting the whole workflow in three steps or '*levels*': L1, L2, L3. Each of them reads out and processes only a limited fraction of the available information. The level-one step is totally hardware-based, whereas L2 and L3 are sets of software requirements and are usually referred to as high level trigger (HLT). The HLT algorithm takes as input relatively few events, therefore it can analyze them in a more detailed way.

#### 2.2.6.1 The Level-1 Trigger

The L1 Trigger uses coarse information from the calorimeter and the muon system, while holding the high resolution data in pipelined memories in the front-end electronics until the trigger decision is taken. It consists of mostly custom-designed, programmable hardware capable of bringing down the event rate from the initial 40 MHz to 100 kHz. The maximum allowed latency is 3.2 $\mu$s, after which, if the L1 accepts the event, the data starts being processed by the HLT. Since it would not be possible to read out and analyze the whole information contained in an event, mostly because of the time needed by tracking algorithms, only calorimeters and muon chambers are involved in the L1 step, as shown in Fig. 2.15.

The calorimeter trigger finds out the four 'best' candidates of each of the following categories: electrons and photons, central jets, forward jets and jets identified on the basis of the shape of the deposited energy. These candidates are handed over to the global calorimeter trigger (GCT), along with the measured missing transverse energy.

The muon trigger is performed independently by DTs, CSCs and RPCs. The DT and CSC triggers carry out a local muon reconstruction by comparing the slopes of track segments built in subsequent detector layers. The RPC trigger compares a given muon track with predefined hit patterns depending on the track $p_T$. The four best muon candidates are passed to the global muon trigger system, which is in charge of matching those from DTs and CSCs with those from RPCs and of discarding low-quality tracks. The L1 electronics is installed partly directly on the detectors, partly in the underground control room about 20 m far from the experimental cavern.

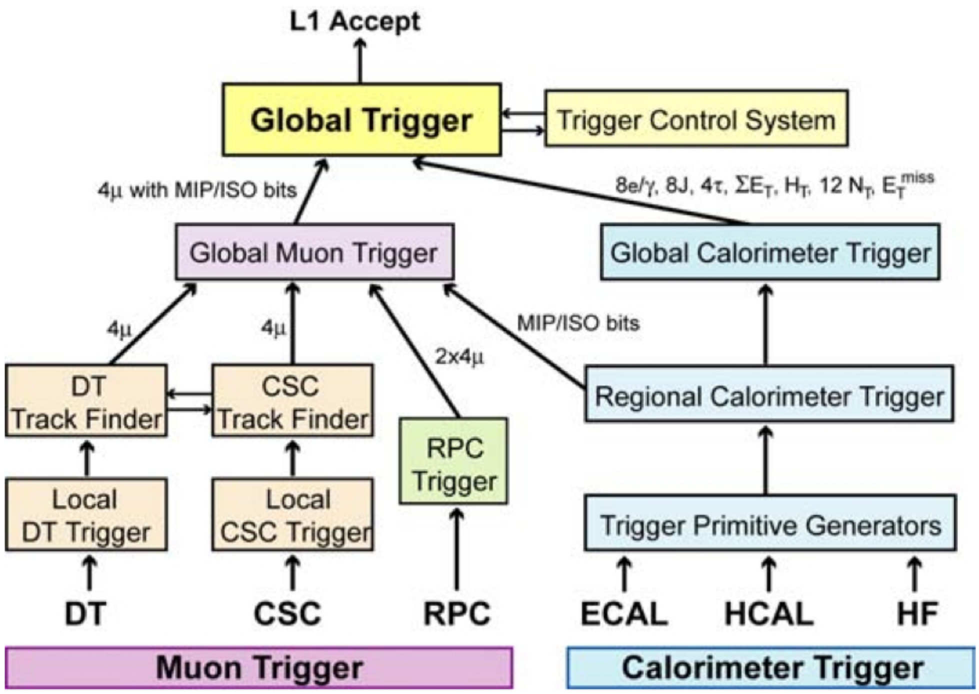


Figure 2.15: Schematic representation of the CMS L1 trigger system.

### 2.2.6.2 The High Level Trigger

The HLT is a software system running on a farm of about 1000 commercial processors, designed to reduce the event rate down to the final output of ≈100 Hz that can be written on tape. The HLT processes all events accepted by the Level-1 trigger in a single processor farm. The reconstruction and selection in the HLT takes place in steps and the selection is optimized step by step in order to reject events as quickly as possible.

The basic idea is to reconstruct those part of each physics object that can be used for selection while minimizing the overall CPU usage *e.g.* the reconstruction of a muon includes the reconstruction of a track in the muon spectrometer, the search of a matching tracker track, and the global track reconstruction. After each step, a set of selection criteria results in the rejection of a significant fraction of the events accepted by the previous step, which results in to reduction of required CPU time for forthcoming steps. Reconstruction and selection are therefore closely intertwined in the online environment of the filter farm.

As a convention, the term Level-2 Trigger is used to refer to algorithms and requirements of the first selection step in the HLT process. Typically, a Level-2 trigger, which has the full Level-1 rate as input, uses only information from the calorimeter and muon detectors. In contrast, Level-3 Trigger refers to a further selection step that includes the reconstruction of full tracks in the tracker. Because of the high number of channels, the complex pattern recognition and higher combinatorics, track reconstruction is a process that demands large amount of CPU time. Thus tracker-tracks are used only for the Level-2 pre-selected events.

The CMS detector hosts partial reconstruction of the information to minimize the CPU time required by the HLT. In many cases, the event acceptance decision by the HLT involves the reconstruction of quantities in only a limited region of the detector *e.g.* for an event accepted by the Level-1 trigger in the inclusive muon stream, only the parts of the muon chambers indicated by the Level-1 trigger results, and the corresponding region in the tracker, need to be considered for the validation of the muon. In HLT, the reconstruction of physics object is driven by the corresponding candidates identified by the Level-1 trigger. This approach leads to significant CPU savings.

A list of reconstruction algorithms and filters for one or more physics objects that starts any time, a Level-1 bit is enabled is called HLT path. For each luminosity scenario the set of trigger paths that, if enabled, contribute to a final OR of decisions which determines whether to reject or store an event, is called *HLT Menu*. A single trigger path can require the presence of one or more physics objects of a particular type that pass specific kinematic thresholds, and it can also mix different type of physics objects (cross triggers). The rate of expected events for a particular set of trigger paths given a luminosity scenario is studied on simulation. By increase in luminosity, the requirements on the trigger paths are becoming more stringent due to rate constraints, and the selection algorithms becomes more complex to cope with the requests of each physics analysis. Trigger paths with lower threshold than those necessary to face the event rate are kept in the HLT Menu with a prescale factor applied. This is done to have on storage the data sample required to measure and monitor the efficiency of the higher threshold trigger paths.

#### 2.2.6.3 The Data Acquisition System

The CMS data acquisition (DAQ) is responsible for conveying the data from about 650 read-out modules to the filter units that will process the events. Each module provides event fragments with a size of ≈ 2 kB. The CMS DAQ structure is outlined in Fig. 2.16. The detector sensors are read out by the so-called *Front−End Drivers* (FEDs) through a builder network having a bisectional bandwidth of 100 GB/s. The FEDs are situated in the underground counting room, ≈ 70 m far from the detector. Events are passed to the event filter systems at a maximum rate of 100 kHz. This large rate, corresponding to the L1 one, is due to the design choice of building the full event already after the L1 trigger stage, unlike in the standard multi-level trigger systems.

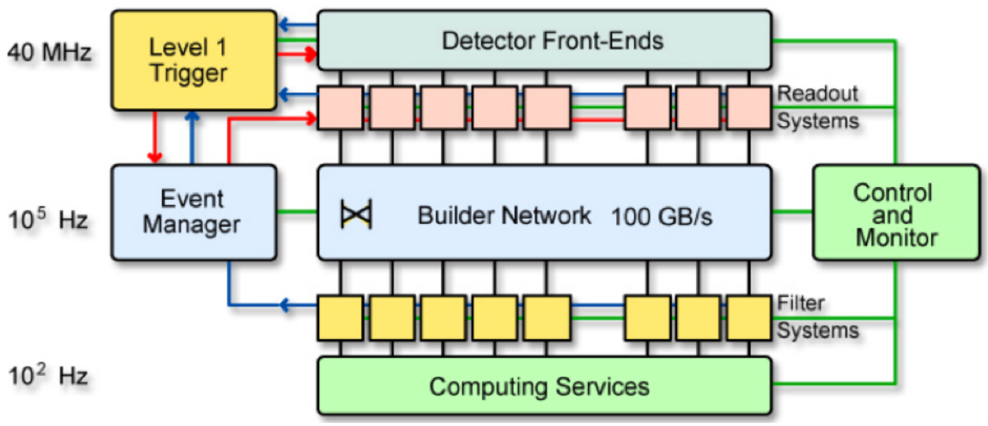


Figure 2.16: The structure of the CMS DAQ system.

### 2.2.7 CMS Computing Model

One of the great challenge for the CMS experiment is to manage the data storage and computational resources that are needed to achieve the physics goals of the experiment. The data volume that the experiment collects, and the computing resources that are needed to analyze the data are more than an order of magnitude larger than previous high energy physics experiments. The development of grid computing in the past ten years have allowed the choice of distributed computing as a solution to meet the challenge. The CMS computing model partitions the aggregate computing resources into three different tiers that serve specific purposes.

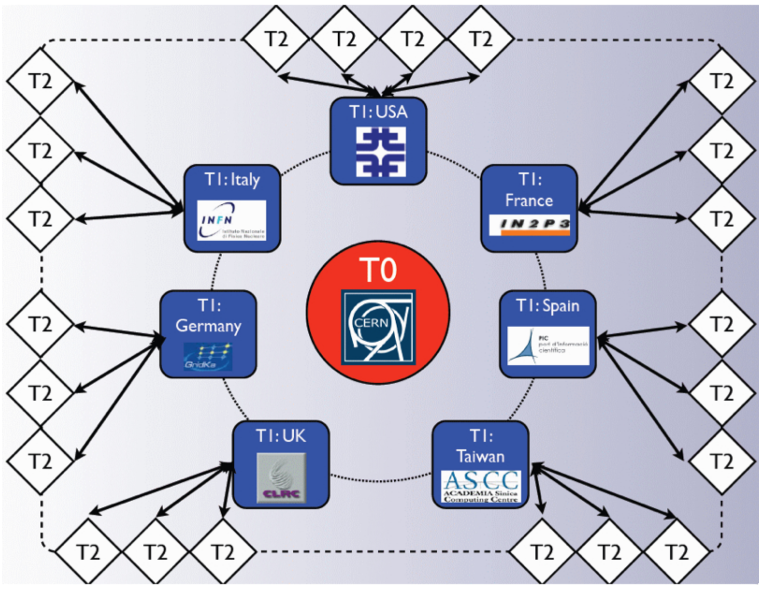


Figure 2.17: Overview of CMS computing framework.

The **Tier-0** center consists of a single large computing farm along with a mass storage system situated at the CERN Meyrin site. It is responsible for receiving the raw data from the storage manager system and converting it into the RAW data format to be stored permanently on the mass storage system at CERN. It also performs a prompt reconstruction, using the best available information on calibration and alignments at the time. The first copy of the RAW data and the prompt reconstruction is stored at the Tier-0 for custodial storage. A second permanently stored copy is transferred to one pre-designated Tier-1 site for custodial archiving.

The eight **Tier-1** centers currently in existence serve primarily two purposes. The first purpose is to archive the custodial copy of the data on their tape mass storage systems. The second purpose is to provide computing resources for reprocessing of the data. As a result, the Tier-1 sites are almost exclusively used for this purpose and analysis activities are severely restricted.

The roughly fifty **Tier-2** centers are primarily dedicated to performing physics analysis. They do not have any tape storage systems and have limited storage space. Roughly 50% of the computing resources of the Tier-2 centers are used for centralized monte carlo production, while the remaining resources are for user analysis. The centrally produced monte carlo data samples are subsequently transferred to a predesignated Tier-1 center for custodial storage.

# Chapter 3

# Event Simulation and Reconstruction

The physics and detector simulation is necessary in high energy physics to model complex physics processes, optimize analysis techniques and comprehend the performance of the numerous and complex sub-detectors of an apparatus such as CMS. Physics event generation and detector response simulation is performed using the monte carlo (MC) method [17]. The MC method uses random sampling applied to a theoretical model to predict its expected behavior in realistic conditions. It relies on computer simulations and can give correct solutions especially in cases where a deterministic solution cannot be derived.

Examples in high energy physics include event simulation where particles are produced in random direction and position but obey the theoretical constraints and also detector simulation, where the detector behavior during passage of particles through it, is modeled precisely including any external parameters such as electronic noise, noise of neighboring sub-detectors and other effects (e.g. temperature changes).

## 3.1 Physics Event Generation

The first step in the simulation process is the event generation, which refers to the procedure of simulating a collision using programs known as MC generators [18]. It is usually performed in many steps following a modular approach, often using different MC programs for each step.

### 3.1.1 Hard Scattering Process

The event generation is initiated by simulation of the hard scattering process. To illustrate the generation process we assume Z production at tree level and decay to lepton pairs, pp $\rightarrow Z \rightarrow \ell\ell$. This process has a matrix element $\mathcal{M}(q\bar{q} \rightarrow Z \rightarrow \ell\ell)$ and the total cross section taking into account the parton distribution functions is:

$$d\sigma = \frac{1}{3}\, f_q f_{\bar{q}}\, \frac{1}{2(xys)^2}\, |\mathcal{M}(q\bar{q} \rightarrow Z \rightarrow \ell\ell)|^2\, \frac{dcos\theta\; d\phi\; dx\; dy}{8(2\pi)^2} \tag{3.1}$$

where $f_q,\ f_{\bar{q}}$ are the parton distribution functions of the proton for each quark $q$ and $s$ is the square of the center of mass energy of the LHC, where $\sqrt{s}$= 7 & 8 TeV in accord with present analysis. The momentum fractions that each quark carries from the original proton are denoted as $x$ and $y$. For the calculation of the cross section, eq. 3.1 is integrated using MC method by picking uniform random numbers $(\theta, \phi, x, y, q)$ and calculating the average $< d\sigma >$ which is an approximation of the cross section integral. Each element d$\sigma$ is referred to as the event weight.

In case of the event generation, the purpose is not the calculation of the cross section but the creation of particles produced by a random collision due to the process under test, in this case *Z production*. To achieve this goal, the maximum event weight d$\sigma_{MAX}$ is calculated by scanning the phase space and then each infinitesimal element d$\sigma$ is normalized by calculating d$\sigma/d\sigma_{MAX}$. For each candidate event, the ratio of event weight over the maximum event weight d$\sigma/d\sigma_{MAX}$ is compared to a random number $g$ generated uniformly in the interval (0,1). Events for which the ratio exceeds the random number (d$\sigma/d\sigma_{MAX}$ > g) are accepted; the others are rejected. Before the output is converted to particles that will be simulated within the detector, additional processes, e.g. NLO effects, (radiation of gluons, quarks and photons ), evolution of jets (explained in succeeding section as *hadronization*) etc. need to be performed.

### 3.1.2 Parton Shower, Underlying Event and Hadronization

The next step is to add higher order effects by 'evolving' the event using parton shower simulation, which allows partons to split in pairs of other partons ($i.e\ g \rightarrow q\bar{q}, q \rightarrow gq$). The resulting partons can branch further, resulting in a large number of final quarks and gluons that are not allowed to exist in isolation due to color confinement. The succeeding act is the modeling of the underlying event (UE). The UE refers to the beam remnants of the proton after the partons contributing to the hard scattering have been pulled out. The beam remnants recoil against a very small transverse momentum, present due to the motion of the partons inside the proton. The resulting partons are then grouped together into color singlet composite hadrons using a phenomenological model known as '*hadronization*'. Fig. 3.1 shows the different steps in the event generation by using an example of a proton collision resulting in two quarks followed by parton shower and hadronization.

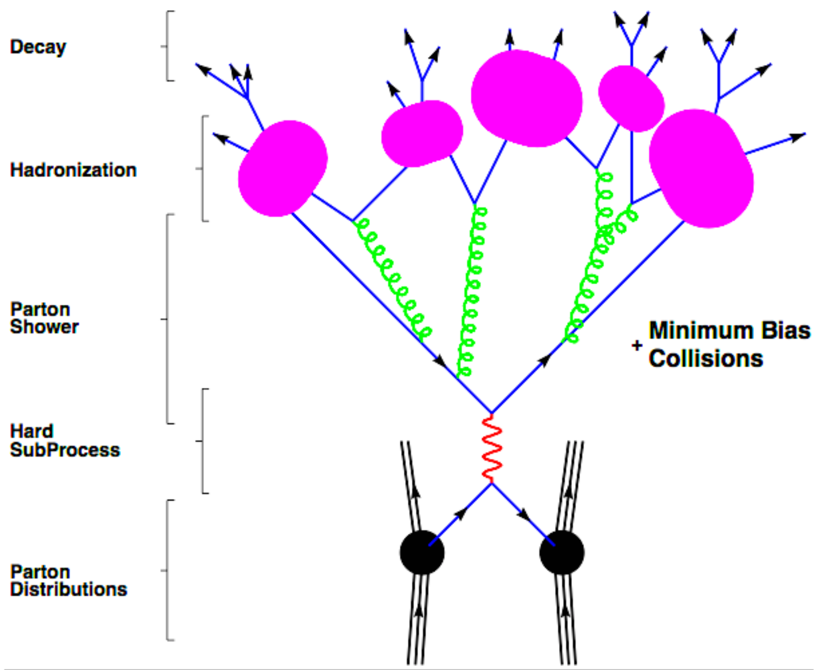


Figure 3.1: The basic structure of a showering and hadronization generator event is shown schematically.

The hadronization scale is in the non-pertubative regime. Therefore, crude phenomenological models which contain several parameters tuned with experimental data are used. The impact of the choice of the hadronization model is small for most physics processes because the hadronization scale is much smaller than the hard scales. Any resonances created during the hadronization process are decayed. Finally the possibility of multi-parton interactions where two or more partons per proton can interact is taken into account and is added to the simulated event.

### 3.1.3 MC Generator Programs

Several MC simulation programs are used to model the SM Higgs signal and background processes in this analysis according to the peculiarities of the different final states under study. A brief description of the respective generators is described in the following sections.

#### 3.1.3.1 PYTHIA

PYTHIA is a general multi-purpose MC event generator for lepton and hadron colliders and discussed in Ref. [19]. It consists of a sub-process library containing about 240 different 2 $\rightarrow$ n sub-processes, all at leading order. The standard processes include SM vector boson and vector boson pair production, QCD multijet production, SUSY, Higgs production and exotic physics. Initial and final state showers are added to provide more realistic configurations especially for the internal structure of jets.

The hadronization is also performed by using a phenomenological model known as the 'Lund model' and the underlying event is simulated by 2 $\rightarrow$ 2 scatterings between the remaining partons. PYTHIA serves either to generate a given hard process at leading order (LO), or, in cases where the hard processes are generated at higher orders, it is used only for the showering, hadronization, decays, and for adding the underlying event; the parton shower and hadronization code developed for PYTHIA is also used when interfaced to other generators such as POWHEG and MadGraph [20] [23].

#### 3.1.3.2 POWHEG

The POWHEG program is an improvement to PYTHIA since it utilizes NLO calculations combined with parton shower. The main idea of the POWHEG method is that the hardest emission (the one with the highest $p_T$) is simulated in accord with the exact NLO cross section. The hardest emission is excluded during the parton shower and subsequent emissions are vetoed if they are harder than the hardest emission. The POWHEG method provides a much better description of basic processes as compared to PYTHIA, such as vector boson and SM Higgs production and is used explicitly to describe final states with low multiplicity such as inclusive W/Z production. In addition, the $t\bar{t} \rightarrow 2\ell 2\nu 2$b samples are generated with POWHEG by using the CTEQ6M PDF [24] and it has been also used for generation of 'single top' [25] and $q\bar{q} \rightarrow ZZ^{*} \rightarrow 4\ell$ background processes.

#### 3.1.3.3 gg2ZZ

The gg2ZZ is used to generate the $gg \to$ ZZ $\to 4\ell$ (see Fig. 1.7b) contribution to the ZZ cross section, which provides an important background for the SM Higgs boson searches in the H→ZZ channel at the LHC. It calculates the loop-induced gluon-fusion process gg→ $Z^*(\gamma^*)Z^*(\gamma^*) \to \ell\bar{\ell}\ell'\bar{\ell'}$ and discussed in Ref. [21].The gg-induced process yields a correction of about 15% (at $\sqrt{s} = 14$ TeV) relative to the NLO QCD prediction for the $q\bar{q}$-induced process when only a $M_{\ell\ell}$, $M_{\ell'\bar{\ell'}} > 5$ GeV cut is applied. The gg→ $ZZ^* \to 4\ell$ events are then showered and hadronized using PYTHIA.

#### 3.1.3.4 MADGRAPH

MADGRAPH program is used to generate multi-parton amplitudes and events for some important background processes. One example is the WZ+jets background in current analysis where one lepton is produced from the W decay, 2 leptons from Z decay and one jet is eventually faking a $4^{th}$ lepton.

PYTHIA is very effective when describing simple $2 \to 2$ processes but with multiple partons, MadGraph generator provides a better description for final states with multiple partons utilizing calculations of diagrams of multiple final state objects at tree level. Given a user process, MadGraph automatically generates the amplitudes for all relevant sub-processes and produces the mappings for the iteration over the phase space. Once the events are generated, they are passed to PYTHIA for the parton shower and hadronization procedures. MadGraph has been used to produce 'W + jets', Z + jets ($m_{\ell\ell} > 50$), Z + jets ($10 < m_{\ell\ell} < 50$), WW $\to 2\ell 2\nu$ and WZ $\to 3\ell\nu$ background processes.

### 3.1.4 K-factors

Even if event generators are becoming more and more sophisticated, there are usually several calculations performed in higher orders that affect observable quantities in the experiment. To account for those additional effects, the specific observables of a generator are re-weighted to match the spectra of the observables of the higher order calculation. The weights that are produced via this process are referred as 'K-factors'. One example is the re-weighting of the $p_T$ of the Higgs boson to match the spectrum obtained by NNLO calculations.

## 3.2 Detector Simulation

The complexity of the CMS Detector requires very sophisticated simulation to properly reproduce the detector behavior in the presence of particles from proton collisions. The detailed simulation is performed using the GEANT4 [22] toolkit. GEANT4 relies on the accurate detector description including the full geometry, the materials of the detecting devices and the dead material (e.g. cables, support, cooling ) to simulate the particle response.

It takes input as particles from the event generator and then propagates them through the detector taking into account the measured magnetic field map (for charged particles) and any interactions between particle and material such as *bremmstralung*, multiple scattering and photon conversions. At the final stage, GEANT4 produces a set of simulated hits in the active material such as the energy loss of a particle in the sensitive volume of a detector. The simulated hits are then fed to emulators of the readout and trigger electronics to simulate the event and provide it in digitized format which is equivalent to the digital information produced by real data events. All subsequent stages, such as event reconstruction, use the same input collection and are the same when running on simulated events or data.

### 3.2.1 Simulation of Multiple Interactions

The number of interactions per crossing can significantly affect the performance of identification of interesting events. Therefore, the effects of pileup need to be simulated properly to account for the changes in performance and allow for studies to improve the performance for operation on higher luminosities. Pileup is simulated by over-laying events at the hit level.

The hard interaction events are mixed with additional simulated minimum bias events [1] by combining the hits between them. Both in-time (multiple vertices per event) and out-of-time (detector response remnants from previous crossings) are simulated. For out-of-time pileup, the time information is shifted by one bunch crossing allowing the slower detectors to be affected by the information in the other crossings. Along with the simulated hits, the generator information is also provided to allow for studies of the merged event.

The distribution of pile-up interactions in the data depends on the run period and the respective LHC configuration. However, the production of the simulated

[1] Minimum bias is a generic term which refers to events that are selected with a 'loose' trigger that accepts a large fraction of the overall inelastic cross section. All triggers produce some bias and the term 'minimum bias' is meaningful when one specifies the precise trigger used to collect the data.

samples is performed centrally before or during the data collection. To avoid multiple simulation production runs, the simulated samples are produced with a poissonian distribution of pile up interactions and that distribution is re-weighted to match the distribution of interactions in data.

## 3.3 Datasets and Triggers

### 3.3.1 Experimental Data

The analysis relies on data samples which are centrally organized in primary datasets (PDs) and its definition in terms of HLT paths (see Sec. 2.2.6.2) has been changing along with the increasing instantaneous luminosity delivered by the LHC. The data sample used in this analysis was recorded by the CMS experiment during 2011 for the run range from 160431 to 180252 and during 2012 for the run range from 190645 to 203002.

In other words, the analysis has been performed over data collected in years 2011 ($\mathcal{L}$ = 5.05 fb$^{-1}$ @ $\sqrt{s}$ = 7 TeV) and 2012 ($\mathcal{L}$ = 12.21 fb$^{-1}$ @ $\sqrt{s}$ = 8 TeV). The absolute $pp$ luminosity is known with a precision of 2.2% in 2011 and 4.4% in 2012. The CMS standard selection of runs and luminosity sections is applied which requires high quality data with a good functioning of the different sub-detectors. Thus, similar detector operation conditions are imposed for the validation of the data to be used for the analysis of the $4e$, $4\mu$ and $2e2\mu$ channels.

For the 2011 data, the analysis relies on the so-called 'DoubleElectron' and 'DoubleMuon' PDs [26]. These latter PDs are formed by an 'OR' between various trigger selections with symmetric or asymmetric trigger thresholds for the two leptons, with or without additional identification and isolation requirements. They also include triggers requiring three leptons above a low $p_T$ threshold.

In 2012, electron-muon cross-triggers are added to recover few percent of inefficiency in the 2e2$\mu$ channel at low Higgs boson masses, forming the so-called 'MuEG' PDs. In addition, tri-electron triggers for both 2011 and 2012 data has been used. The PDs and trigger paths used for this analysis are summarized in Tab. 3.1 and corresponds to different data taking periods. Tab. 3.2 shows all the trigger paths used with 2012 data. The naming convention of trigger paths displays the information about set of selection cuts used, named as very loose (VL), tight (T), very tight (VT) over lepton's isolation (Iso), identification (Id) in calorimeters (Calo) and trackers (Trk). Some additional comments:

- In 2011, when applying double muon triggers other then `HLT_Mu17_Mu8` one has to require 2 offline reconstructed muons having $p_T > 17$ GeV and $p_T > 8$ GeV.

- While running on data, $4\mu$ channel is obtained from DoubleMu datasets, $4e$ channel is obtained from DoubleElectron datasets and $2e2\mu$ channel have been obtained from DoubleElectron & DoubleMu PDs by vetoing DoubleElectrons triggers for 2011 data, while for 2012, MuEG dataset has been used in addition by vetoing DoubleElectrons and DoubleMuons triggers.

Table 3.1: Datasets and trigger paths used in the analysis. CaloTrk = CaloIdT_CaloIsoVL_TrkIdVL_TrkIsoVL

| Datasets | |
|---|---|
| 2011 | 2012 |
| /DoubleElectron/Run2011A-16Jan2012-v1<br>/DoubleMu/Run2011A-16Jan2012-v1<br>/DoubleElectron/Run2011B-16Jan2012-v1<br>/DoubleMu/Run2011B-16Jan2012-v1 | /DoubleElectron/Run2012A-13Jul2012-v1<br>/DoubleMu/Run2012A-13Jul2012-v1<br>/MuEG/Run2012A-13Jul2012-v1/<br>/DoubleElectron/Run2012A-recover-06Aug2012-v1<br>/DoubleMu/Run2012A-recover-06Aug2012-v1<br>/MuEG/Run2012A-recover-06Aug2012-v1<br>/DoubleElectron/Run2012B-13Jul2012-v1<br>/DoubleMu/Run2012B-13Jul2012-v4<br>/MuEG/Run2012B-13Jul2012-v1<br>/DoubleElectron/Run2012C-24Aug2012-v1<br>/DoubleElectron/Run2012C-PromptReco-v2<br>/DoubleMu/Run2012C-24Aug2012-v1<br>/DoubleMu/Run2012C-PromptReco-v2<br>/MuEG/Run2012C-24Aug2012-v1<br>/MuEG/Run2012C-PromptReco-v2 |
| Muon triggers | |
| `HLT_DoubleMu7`<br>`OR HLT_Mu13_Mu8`<br>`OR HLT_Mu17_Mu8` | `HLT_Mu17_Mu8` |
| Electron triggers | |
| `HLT_Ele17_CaloTrk_Ele8_CaloTrk`<br>`OR HLT_Ele17_CaloTrk_Ele8_CaloTrk`<br>`OR HLT_TripleEle10_CaloIdL_TrkIdVL` | `HLT_Ele17_CaloTrk_Ele8_CaloTrk`<br>`HLT_Ele15_Ele8_Ele5_CaloIdL_TrkIdVL` |
| Cross triggers | |
| | `HLT_Mu17_TkMu8`<br>`OR HLT_Mu8_Ele17_CaloTrk`<br>`OR HLT_Mu17_Ele8_CaloTrk` |
| Integrated luminosity | |
| 5.05 $fb^{-1}$ | 12.21 $fb^{-1}$ |

### 3.3.2 Simulated Samples

The SM Higgs boson signal samples, as well as samples for a large variety of electroweak and QCD-induced SM background processes, have been obtained using detailed MC simulations. All datasets were subject to full reconstruction. The signal and background samples have been used for the optimization of the event selection strategy prior to the analysis of the experimental data (see Sec. 3.5). They are further used in this analysis for the comparisons with the measurements, the evaluation of acceptance corrections and systematics, and for the background evaluation

Table 3.2: Trigger selections in 2012 data analysis. CaloTrk=CaloIdT_CaloIsoVL_TrkIdVL_TrkIsoVL and CaloTrkVT=CaloIdVT_CaloIsoVT_TrkIdT_TrkIsoVT

| # Channel | Purpose | HLT path | L1 seed | prescale |
|---|---|---|---|---|
| 4e | main | HLT_Ele17_CaloTrk_Ele8_CaloTrk | L1_DoubleEG_13_7 | 1 |
| | | HLT_Ele15_Ele8_Ele5_CaloIdL_TrkIdVL | L1_TripleEG_12_7_5 | 1 |
| 4$\mu$ | main | HLT_Mu17_Mu8 | L1_Mu10_MuOpen | 1 |
| | | OR HLT_Mu17_TkMu8 | L1_Mu10_MuOpen | 1 |
| 2e2$\mu$ | main | HLT_Ele17_CaloTrk_Ele8_CaloTrk | L1_DoubleEG_13_7 | 1 |
| | | OR HLT_Mu17_Mu8 | L1_Mu10_MuOpen | 1 |
| | | OR HLT_Mu17_TkMu8 | L1_Mu10_MuOpen | 1 |
| | | OR HLT_Mu8_Ele17_CaloTrk | L1_MuOpen_EG12 | 1 |
| | | OR HLT_Mu17_Ele8_CaloTrk | L1_Mu12_EG6 | 1 |
| Trigger paths used for lepton's measurements via tag & probe method [28], [29] | | | | |
| 4e and 2e2$\mu$ | Z T&P | HLT_Ele17_CaloTrkVT_Ele8_Mass50 | L1_DoubleEG_13_7 | 5 |
| 4e and 2e2$\mu$ | Z T&P low pT | HLT_Ele20_CaloTrkVT_SC4_Mass50_v1 | L1_SingleIsoEG18er | 10 |
| 4$\mu$ and 2e2$\mu$ | Z T&P | HLT_IsoMu24_eta2p1 | L1_SingleMu16er | |
| 4$\mu$ and 2e2$\mu$ | J/psi T&P | HLT_Mu7_Track7_Jpsi | | |
| | | HLT_Mu5_Track3p5_Jpsi | | |
| | | HLT_Mu5_Track2_Jpsi | | |

procedure where measurements in a 'background control' region are extrapolated to the 'signal' region. The various type of backgrounds contributing in current analysis has been briefly discussed in Sec. 1.4.

The individual Monte Carlo simulation datasets used for this analysis has been summarized in Tab. 3.3 along with MC simulation programs and respective cross-sections. All the signal and background processes cross sections are re-weighted to the NLO. In the case of SM Higgs boson production via the gluon fusion mechanism, the most recent NNLO+NNLL calculations of the cross sections are included in Ref. [27]. More details on the event generators and the background samples used in this analysis, as well as indications on the procedures used to re-weight the MC events where needed, are provided in the following section.

#### 3.3.2.1 Signal: $\mathrm{H} \rightarrow \mathrm{ZZ}^* \rightarrow 4\ell$

The Higgs boson samples used in the current analysis are generated with POWHEG which incorporates NLO gluon fusion ($gg \rightarrow \mathrm{H}$) and vector boson fusion $q\bar{q} \rightarrow q\bar{q}\mathrm{H}$. The CTEQ6M parton distribution (PDF) set is used for generation with the Higgs boson widths taken from Ref. [27]. Additional samples with WH, ZH and $t\bar{t}\mathrm{H}$ associated production are produced with PYTHIA. The Higgs boson is forced to decay to two Z-bosons, which are allowed to be off-mass shell, and both Z-bosons are forced to decay via $\mathrm{Z} \rightarrow 2\ell$. Generator level events are re-weighted according to the total cross section $\sigma(pp \rightarrow \mathrm{H})$ which comprises the gluon fusion contribution up to NNLO and NNLL taken from Refs. [27, 33, 34, 35, 36, 37, 38, 39, 41, 42] and the weak-boson fusion contribution at NNLO computed in Refs. [27, 43, 44, 45, 46, 47] The total

| Process | MC generator | $\sigma_{(N)NLO}$ 7 TeV | 8 TeV |
|---|---|---|---|
| **Higgs boson** H $\rightarrow$ ZZ $\rightarrow 4\ell$ | | | |
| $gg \rightarrow$ H | POWHEG | [1-20] fb | [1.2-25] fb |
| $VV \rightarrow$ H | POWHEG | [0.2-2] fb | [0.3-25] fb |
| **ZZ continuum** | | | |
| $q\bar{q} \rightarrow$ ZZ $\rightarrow 4e(4\mu, 4\tau)$ | POWHEG | 66.09 fb | 76.91 fb |
| $q\bar{q} \rightarrow$ ZZ $\rightarrow 2e2\mu$ | POWHEG | 152 fb | 176.7 fb |
| $q\bar{q} \rightarrow$ ZZ $\rightarrow 2e(2\mu)2\tau$ | POWHEG | 152 fb | 176.7 fb |
| $gg \rightarrow$ ZZ $\rightarrow 2\ell 2\ell'$ | gg2ZZ | 3.48 fb | 12.03 fb |
| $gg \rightarrow$ ZZ $\rightarrow 4\ell$ | gg2ZZ | 1.74 fb | 4.8 fb |
| **Other di-bosons** | | | |
| WW $\rightarrow 2\ell 2\nu$ | Madgraph | 4.88 pb | 5.995 pb |
| WZ $\rightarrow 3\ell\nu$ | Madgraph | 0.868 pb | 1.057 pb |
| $t\bar{t}$ **and single** $t$ | | | |
| $t\bar{t} \rightarrow \ell^+\ell^-\nu\bar{\nu}b\bar{b}$ | POWHEG | 17.32 pb | 23.64 pb |
| $t$ ($s$-channel) | POWHEG | 3.19 pb | 3.89 pb |
| $\bar{t}$ ($s$-channel) | POWHEG | 1.44 pb | 1.76 pb |
| $t$ ($t$-channel) | POWHEG | 41.92 pb | 55.53 pb |
| $\bar{t}$ ($t$-channel) | POWHEG | 22.65 pb | 30.00 pb |
| $t$ ($tW$-channel) | POWHEG | 7.87 pb | 11.77 pb |
| $\bar{t}$ ($tW$-channel) | POWHEG | 7.87 pb | 11.77 pb |
| **Z/W + jets** ($q = d, u, s, c, b$) | | | |
| W + jets | MadGraph | 31314 pb | 36257.2 pb |
| Z + jets, $m_{\ell\ell} > 50$ | MadGraph | 3048 pb | 3503.7 pb |
| Z + jets, $10 < m_{\ell\ell} < 50$ | MadGraph | 12782.63 pb | 915 pb |

Table 3.3: Monte Carlo simulation datasets used for the signal and background processes; Z stands for Z, Z$^*$, $\gamma^*$; $\ell$ means $e$, $\mu$ or $\tau$; V stands for W and Z; $\hat{p}_T$ is the transverse momentum for 2 $\rightarrow$ 2 hard processes in the rest frame of the hard interaction. Comment: $q\bar{q} \rightarrow ZZ^*$ samples at 8 TeV have lower cut in $m_{ll}$, 4 GeV instead of 12 GeV at 7 TeV. TuneZ2 is used for 7 TeV, while TuneZ2star is used for 8 TeV analysis. The low mass Drell-Yann was produced with a filter for the 8 TeV analysis.

cross section is scaled by the $BR$(H $\rightarrow 4\ell$) discussed in Refs. [27, 48, 49, 50, 53].

Fig. 3.2 (a) shows the H $\rightarrow ZZ \rightarrow 4\ell$ cross-section as a function of the Higgs mass $m_{\rm H}$ for $\sqrt{s} = 7$ TeV. For 2011 production, a total of 28 Monte Carlo samples were produced in the range 115 GeV/c$^2$ to 600 GeV/c$^2$, with a step of 10 GeV/c$^2$ up to 230 GeV/c$^2$, and then steps of 25 GeV/c$^2$ up to 600 GeV/c$^2$. In 2012 production, additional samples were produced from 650 GeV/c$^2$ to 1000 GeV/c$^2$, with a step of 50 GeV/c$^2$, as well as additional low mass samples with finer granularity.

In comparison to $\sigma(pp \rightarrow$ H$) \cdot BR$(H $\rightarrow$ ZZ$^{(*)} \rightarrow 2e2\mu$), the $4\mu$ and $4e$ channel

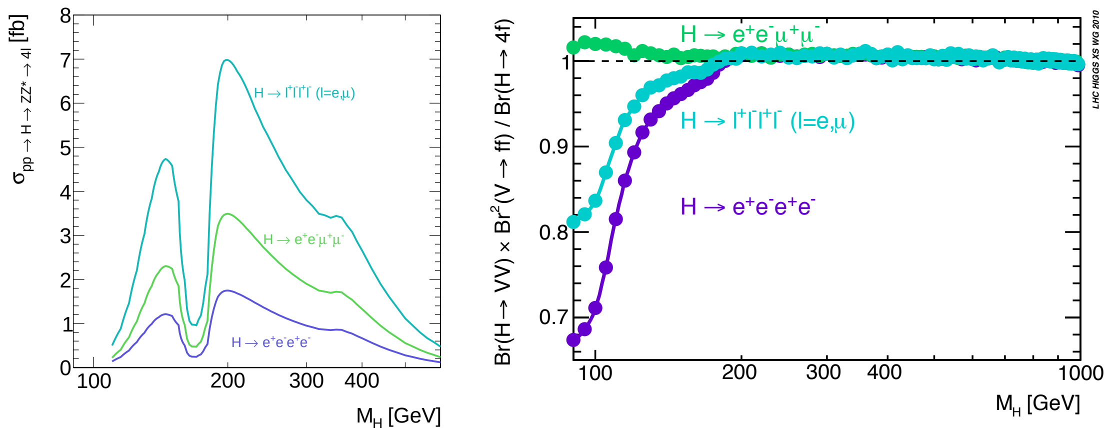


(a) (b)

Figure 3.2: Cross-section for SM Higgs in H $\to 4\ell$, H $\to 2e2mu$ and H $\to 4e$ (or $4\mu$) as a function of $m_{\rm H}$ in pp collisions at $\sqrt{s} = 7$ (a). Cross-section enhancement due to the interference of amplitudes with permutations of identical leptons originating from different Z-bosons, as a function of $m_{\rm H}$ (b).

cross-sections are enhanced in the case of off-shell Z boson due to an interference of amplitudes with permutations of identical leptons originating from different Z-bosons, as shown in Fig. 3.2 (b). This is correctly taken into account by Prophecy4f, discussed in Refs. [27, 48, 49].

The `POWHEG` MC program used to simulate the $gg \to$ H process results in a Higgs boson $p_T$ spectrum that differs significantly from the best theoretical calculation which is available at NNLL+NLO. A theoretical estimate of this $p_T$ spectrum is computed using the `HqT` [51] program, which implements such NNLL+NLO calculation. A re-weighting procedure has been studied to be applied to the simulated events but the effect is very small for this analysis in which no direct constraints are imposed on the transverse momentum of the $4\ell$ system, or on the hadronic recoil against this system (e.g. no jet veto or missing transverse momentum cut).

In the current analysis, only samples for gluon fusion production mechanism have been used and rescaled to the total cross section including all other production processes (weak-boson fusion, WH, ZH and $t\bar{t}$H associated production).

#### 3.3.2.2 Background: $q\bar{q} \to ZZ^* \to 4\ell$

The $q\bar{q} \to ZZ^* \to 4\ell$ samples have been produced with `POWHEG`, that include the complete NLO simulation, interfaced to `PYTHIA` for showering, hadronization, decays and the underlying event.

#### 3.3.2.3 Background: $gg \to ZZ^* \to 4\ell$

The gluon-induced ZZ background, although technically of NNLO compared to the first order Z-pair production, amounts to a non-negligible fraction of the total irreducible background at masses above the $2M_Z$ threshold. A full NNLO calculation for the ZZ production which would also take these gluon-induced diagrams into account is not available. Therefore the contributions are estimated by using the dedicated tool gg2ZZ, which computes the $gg \to ZZ$ at LO, which is of order $\alpha_s^2$, compared to $\alpha_s^0$ for the LO $q\bar{q} \to ZZ$. The hard scattering $gg \to ZZ^* \to 4\ell$ events are then showered and hadronized using PYTHIA.

The gg2ZZ tools provide the functionality to compute the cross-section after applying a cut on the mimimally generated invariant mass of the same-flavour lepton pairs (which can be interpreted as the $Z/\gamma$ invariant mass) $m_{\ell\ell}^{\min} = 10$ GeV/c$^2$.

The gg2ZZ generator gives the contribution for final states with unlike flavours of the lepton pairs, but it was also used to estimate the like-flavour background. This is an approximation which is only strictly valid when $m_{4\ell} \geq 2\,m_Z$. Below this threshold the relative amount of like-flavour events increases compared to unlike-flavour events.The differential cross-section for $gg \to ZZ^{(*)}$ as a function of the four lepton invariant mass for different flavour lepton pairs was provided in Ref. [54].

#### 3.3.2.4 Background: W/Z+jets$\to 2\ell$+jets

Z+jets$\to 2\ell$+jets sample was generated with MadGraph, with a statistics of $\approx 40$M events representing an equivalent integrated luminosity well above $\mathcal{O}(10)$ fb$^{-1}$. Both light ($q = d, u, s$) and heavy-flavor ($q = c, b$) jets are included in the sample. A generation cut on two-lepton invariant mass of $m_{2\ell} > 50\ GeV/c^2$ is imposed in the simulation. A total NNLO cross section of 3048 (3503.7) pb$^{-1}$ is used at 7 (8) TeV.

To separate the contribution of light flavor jets from heavy-flavor jets (from now on referred to as the $Zb\bar{b}/Zc\bar{c}$ sample), the Madgraph Z+jets sample was partitioned in Z+light jets and Z+heavy flavor jets using a filter selecting events with two b-jets or two c-jets in the final state. More detail is given in Sec. 3.5.

#### 3.3.2.5 Background: $t\bar{t} \to 2\ell 2\nu 2b$

A $t\bar{t} \to 2\ell 2\nu 2b$ sample is generated with POWHEG event generator using CTEQ6M. The theoretical NLO cross-section for the process is $\sigma_{NLO}(pp \to t\bar{t} \to 2\ell 2\nu 2b) =$ 17.32 (23.64) pb$^{-1}$ at 7 (8) TeV [55].

## 3.4 Lepton Selection

The reconstruction of the SM Higgs boson in the decay chain $H \rightarrow ZZ^* \rightarrow 4\ell$ imposes high-performance lepton reconstruction, identification and isolation as well as excellent lepton energy-momentum measurements. The identification of isolated leptons emerging from the event primary vertex allows for a drastic reduction of QCD-induced sources of misidentified 'fake' leptons. The precision in energy-momentum measurements translates in a precise measurement of Higgs boson mass ($m_{4\ell}$), one of the most discriminating observable for the Higgs boson search and background control.

In view of the modest fraction of the total production cross-section observable in the decay channel having 4 leptons in the final state, a very high lepton reconstruction efficiency is mandatory. For Higgs boson having mass $m_{\rm H} < 2m_Z$, one lepton pair at least couples to an off-shell $Z^*$ boson. The softest lepton in that pair typically has $p_T^\ell < 10$ GeV/c for masses $m_{\rm H} < 140$ GeV/c$^2$. To ensure sufficient discrimination against hadronic jets while preserving the highest possible reconstruction efficiency, is especially challenging for the reconstruction of leptons at very low $p_T^\ell$. Such very low $p_T^\ell$ values lie at the extreme edge of the domain which is controlled at the LHC using tag-and-probe [28], [29] methods and the efficiencies for reconstruction, identification and trigger for electrons and muons is measured with data based on a selection of events of inclusive single Z production.

The tag-and-probe technique combines the requirements of a mass constraint from a pair of basic objects (e.g. tracks for muons, or clusters of calorimetry cells for electrons) with a tight lepton selection applied on one leg (the '*tag*'), so to ensure sufficient purity. The other leg (the '*probe*') is used to measure the efficiency of a given reconstruction algorithm or identification criterium. The efficiency is defined as the ratio of the number of passing probes to the total number of probes before the cut.

In the case of the muons, this can be complemented by tag-and-probe using $J/\Psi$ production. In the low $p_T$ range, a full combination of information provided by the tracker and electromagnetic calorimetry (for electrons) or by the tracker and muon spectrometer (for muons) becomes essential for the reconstruction, identification and isolation of leptons. Otherwise, the single Z production is an ideal candle for this analysis, covering leptons in the $p_T$ range from $\mathcal{O}(10)$ to $\mathcal{O}(100)$ GeV/c.

For the completeness of present work, a brief overview of electrons/muons reconstruction, identification and isolation techniques has been presented in following sections. Their detailed explanation can be found in Ref. [62].

### 3.4.1 Electron Reconstruction

The electron reconstruction procedure is discussed in Ref. [56], which combines ECAL and tracker information. Electron candidates are reconstructed from clusters of energy deposits in the electromagnetic calorimeter (ECAL), which are then matched to hits in the silicon tracker. The standard CMS electron reconstruction algorithm is used from Refs. [56, 57, 58] for this analysis.

The energy deposited in the ECAL is measured in clusters of clusters (superclusters) which collect bremsstrahlung photons emitted in the tracker volume. Superclusters are used to search for hits in the innermost tracker layers which are used to seed electron tracks. This procedure is complemented by a tracker-driven approach allowing to improve the reconstruction efficiency at low $p_T$. Trajectories in the tracker volume are reconstructed using a dedicated modeling of the electron energy loss and fitted with a gaussian sum filter (GSF). A cleaning is performed to resolve ambiguous cases where several tracks are reconstructed due to the conversion of radiated photons in the tracker material. Electron candidates are preselected using loose cuts on track-cluster matching observables so to preserve the highest possible efficiency while removing part of the QCD background.

For the physics analysis, the electron candidates are required to have transverse momentum $p_T^e > 7$ GeV/c and should be within detector's geometrical acceptance having $|\eta^e| < 2.5$. The reconstruction efficiency for isolated electrons is expected to be above $\approx 90\%$ over the full ECAL acceptance, apart from some narrow 'crack' regions. Electron charge mis-identification has been measured on 2010 data using Z events and a charge mis-ID of $0.004 \pm 0.001$ ($0.028 \pm 0.003$) was measured in the ECAL barrel (ECAL endcaps) in very good agreement with the simulation, described in Ref. [59]. No significant $p_T$ dependency was observed in the range of on-shell Z boson decays, also in agreement with the expectation.

#### 3.4.1.1 Momentum Estimation

The four-momenta for an electron is obtained by taking angles from the associated GSF track, and the energy from a combination of tracker and ECAL information, as explained in Ref. [56]. The information from the track is measured at the distance-of-closest approach to the beam spot position in the transverse plane. Electron tracks are not re-fitted to the common primary vertex. In this analysis, the ECAL information is obtained via a Regression technique, described in Ref. [62]. The electron momentum scale and resolution can be controlled using Z boson (and J/$\psi$) decays to electrons.

Some discrepancies with respect to simulation are observed, especially in the low

$p_T$ part of the electron spectrum and in the endcaps. Based on Z → ee data and simulated events, these discrepancies are dealt by correcting the energy scale in data and then by determining the smearing needed to apply to the simulated samples so as to have the best match between data and simulation. The procedure consists of two steps:

**Absolute scale corrections for data:** The supercluster energy scale is tuned and corrected varying the scale in the data to match the Monte Carlo in Z→ee events. The data-MC difference is time dependent; moreover the time dependence is not the same in different pseudorapidity regions while it is very similar for showering and non showering electrons. This is done in two $R_9$ bins, since this variable categorizes two different kinds of clusters. The final energy scale correction is then derived as the product of the two corrections in n(run range) × 4(pseudorapidity region) × 2($R_9$) categories.

**MC energy smearing:** A method which applies direct smearing to the MC energies estimates more efficiently the effective resolution of the ECAL. The electron supercluster energy is modified by applying a Gaussian multiplicative factor centered in $1 + \Delta P$ and with a $\Delta\sigma$ resolution, where $\Delta P$ is the energy scale correction and $\Delta\sigma$ is the additional constant term in the energy resolution.

Both the data scale corrections and the smearings have been obtained by fits to the high statistics Z→ee control sample. The spectrum for electrons from Z is typically peaking at $p_T \approx 45$ GeV/c, while the electrons from H→ZZ→ $4\ell$ typically span from 7 to 50 GeV/c (higher for the high $m_H$ hypotheses). It has been demonstrated that a multivariate regression approach for determining the energy of an electron can significantly improve the resolution of the measurement. A technique has been employed for the analysis to improve the mass resolution for final states involving electrons. Details of the method and performance can be found in reference Ref. [62].

### 3.4.2 Electron Identification

The purity of the sample of electron candidates is enhanced for the analysis by applying identification requirements on top of the basic collection of reconstructed electron objects. Electron candidates are selected by using the newly developed electron identification tool using multivariate techniques mentioned in Ref. [70]. It makes use of three main categories of variables: observables that match the information of the calorimeters and the tracker including the preshower, purely-calorimetric and purely-tracking observables. The complete list of track-ECAL matching variables is presented below:

- $E_{tot}/p_{in}$, where $E_{tot}$ is the supercluster energy and $p_{in}$ is the track momentum at the innermost track position;
- $E_e/p_{out}$, where $E_e$ is the energy of the cluster closest to the electron track extrapolation to ECAL and $p_{out}$ the track momentum at the outermost track position;
- $\Delta\eta_{in} = \eta_{sc} - \eta_{in}^{extrap.}$, where $\eta_{sc}$ is the energy weighted position in $\eta$ of the supercluster and $\eta_{in}^{extrap.}$ is the $\eta$ coordinate of the position of the closest approach to the supercluster position, extrapolating from the innermost track position and direction;
- $\Delta\phi_{in} = \phi_{sc} - \phi_{in}^{extrap.}$, where $\Delta\phi_{in}$ is a quantity similar to the former one but in azimuthal coordinates.
- $\Delta\eta_{out} = \eta_e - \eta_{out}^{extrap.}$, where $\eta_e$ is the $\eta$ position of the cluster closest to the electron track extrapolation to ECAL ($\eta_{out}^{extrap.}$).
- $1./E_{tot} - 1./p_{4-mom}$ which measures the deviation of the supercluster energy and electron momentum obtained by combining the tracker and ECAL information $p_{4-mom}$.

In order to improve the electron-pion discrimination, the energy measured in the HCAL and in the preshower (ES) is also compared with the supercluster energy by using the ratios: $E_{HCAL}/E_{tot}$ and $E_{ES}/E_{tot}$. In addition, several shower shapes variables are used:

- $\sigma_{i\eta i\eta}$ the width of the ECAL cluster along the $\eta$ direction computed in the $5\times5$ block of crystals centered on the highest energy crystal of the seed cluster.
- $\sigma_{i\phi i\phi}$ as the former but in azimuthal coordinates.
- $\eta - width$ supercluster $\eta$ width.
- $\phi - width$ supercluster $\phi$ width.
- $(E_{5\times5} - E_{5\times1})/E_{5\times5}$, where $E_{5\times5}$ is the energy computed in block of crystals and $E_{5\times1}$ is the energy computed in the strip of crystals containing the cluster seed.
- $R9 = E_{3\times3}/E_{tot}$ energy sum of $3 \times 3$ crystal centered on the most energetic, divided by the supercluster energy.

Finally, to further improve the separation between electrons and charged hadrons, pure tracking observables are also used, both using the dedicated CMS electron tracking (GSF) or the standard KF tracks:

- $\mathrm{f}_{brem} = (p_{in} - p_{out})/p_{in}$ with the GSF track, which measures very well the bremsstrahlung emission which helps in discriminating against charged-hadron particles.

- $\chi^2_{GSF}$, $hits_{KF}$, $\chi^2_{KF}$

The information carried out by these variables is maximized by using a multivariate analysis (boosted decision trees or BDT) [70] where the signal and background samples for the training have been carefully chosen.

#### 3.4.2.1 Working Point Optimization

The identification of electrons relies on BDT multivariate technique that combines observables sensitive to the amount of bremsstrahlung along the electron trajectory, the geometrical and momentum matching between the electron trajectory and associated clusters, as well as shower-shape observables. An optimization procedure was performed in order to find the BDT working point to be used in this analysis. The multivariate identification was trained using a Higgs boson MC sample for the signal and a W + 1-fake electron data sample for background. The working point was optimized using a Z + 1-fake electron data sample. The cut values on the BDT output resulting from the optimization procedure are summarized below:

- $5 < p_T < 10$ GeV:
  - $|\eta| < 0.8 : BDT > 0.47$
  - $0.8 < |\eta| < 1.479 : BDT > 0.004$
  - $|\eta| > 1.479 : BDT > 0.295$
- $p_T > 10$ GeV
  - $|\eta| < 0.8 : BDT > 0.5$
  - $0.8 < |\eta| < 1.479 : BDT > 0.12$
  - $|\eta| > 1.479 : BDT > 0.6$

The electron identification efficiencies for single electrons as a function of the electron probe $p_T$ (with $p_T$ >7 GeV/c) are measured for data collected in 2011 and 2012 and shown in Fig. 3.3 for 8 TeV (2012) data, together with MC efficiencies. This is obtained by fitting signal simulation, where the probe electron is matched with a generated electron. In addition, the tail in data is constrained by what is obtained from MC. The efficiencies are computed in bins of $\eta$ coverage and all data taking periods are considered together. An overall good data/MC agreement in the barrel and the endcaps is observed. Only statistical errors are reported on the plots. The differences observed at low $p_T$ and in the endcaps between data and MC are mostly due to the background estimation (with higher background in the low $p_T$ and high $\eta$ regions) and the known discrepancies between data and MC of some of the variables used in the electron ID.

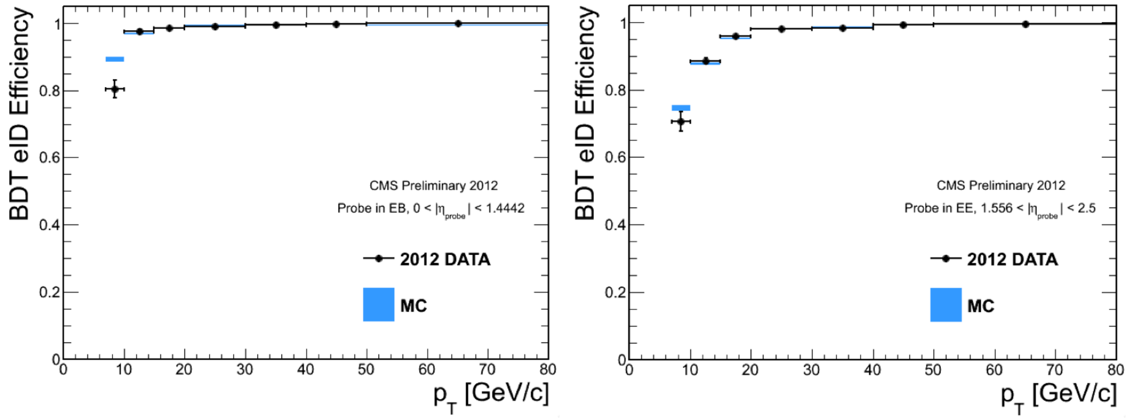


(a) (b)

Figure 3.3: Electron identification efficiencies computed with the tag-and-probe method as a function of the probe $p_T$ in two different $\eta$ bins: (a) $|\eta| < 1.442$ (barrel), (b) $1.556 < |\eta| < 2.5$ (endcap). Results are for 8 TeV data.

### 3.4.3 Muon Reconstruction

In the standard CMS reconstruction for pp collisions, muon tracks are first reconstructed independently in the inner tracker (*tracker track*) and in the muon system (*standalone-muon track*). Based on these objects, two reconstruction approaches are used in accord with Ref. [28] and briefly discussed below:

- **Global Muon reconstruction (outside-in).** For each standalone-muon track, a matching tracker track is found by comparing parameters of the two tracks propagated onto a common surface, and a *global-muon track* is fitted combining hits from the tracker track and standalone-muon track, using the Kalman-filter technique [64]. At large transverse momenta, $p_T \geq 200$ GeV/c, the global-muon fit can improve the momentum resolution compared to the tracker-only fit [65, 66].

- **Tracker Muon reconstruction (inside-out).** In this approach, all tracker tracks with $p_T > 0.5$ GeV/c and the total momentum $p > 2.5$ GeV/c are considered as possible muon candidates and are extrapolated to the muon system taking into account the magnetic field, the average expected energy losses, and multiple scattering in the detector material. If at least one muon segment (*i.e.* a short track stub made of DT or CSC hits) matches to the extrapolated track, the corresponding tracker track qualifies as a Tracker Muon. Track-to-segment matching is performed in a local (chamber) coordinate system, where local $x$ is the best-measured coordinate (in the $r$-$\phi$ plane) and local $y$ is the coordinate orthogonal to it. The extrapolated track and the segment are considered to be matched if the distance between them in local $x$ is less than 3 cm or if the value of the pull for local $x$ is less than 4, where the pull is defined as the difference between the position of the matched segment and the position of the extrapolated track, divided by their combined uncertainties.

The tracker muon reconstruction is more efficient than the global muon reconstruction at low momenta, $p \leq 5$ GeV/c because it requires only a single muon segment in the muon system, whereas global muon reconstruction is designed to have high efficiency for muons penetrating through more than one muon station and typically requires segments in at least two muon stations.

Due to the high tracker-track efficiency [67] and a very high efficiency of reconstructing segments in the muon system, about 99% of muons produced in $pp$ collisions and having sufficiently high momentum are reconstructed either as a global muon or a tracker muon, and very often as both. Candidates found both by the global muon and the tracker muon approaches that share the same tracker track are merged into a single candidate. Muons reconstructed only as standalone-muon tracks have worse momentum resolution and less favorable collision muon to cosmic-ray muon ratio than the global and tracker muons and are usually not used in physics analyses.

#### 3.4.3.1 Momentum Estimation and Corrections

In this analysis, momentum scale calibrations are applied to muons both in data and in simulations, derived from the $1/p_T$ distributions of muons from Z decays [68]. The corrections are designed to calibrate the overall momentum scale and to remove any dependency of the scale on the $p_T, \eta, \phi$ and charge of the muon, thereby improving also the momentum resolution. In addition, on simulation a smearing of the momentum measurement is applied to better match the momentum resolution in data. Detailed comparisons between data and MC, after mu-scale corrections on DATA and smearing on MC, is shown in Sec. 7.4.12 of Ref. [62].

#### 3.4.3.2 Ghost Muon Removal

The most recent changes in tracking techniques in official software framework of CMS results as an evolution of new class of muons, known as 'bad' or 'ghost' muons [62]. They appeared as following two flavors:

- **Split tracks**: the tracker track of a muon is broken in two, both are identified as muons. The signature is as follows: shared muon segments, small $\Delta R$, same sign.

- **Mismatch tracks:** the track of another particle in the event is also found to be compatible with the same muon hits. The signature is shared segments.

These 'ghost muons' have almost no influence in the signal region due to the application of particle flow muon identification criteria (see next section) that reject most of them. However, in the background control region where these criteria are relaxed, thus allowing 'ghost muons' to enter in this phase space, they could perturb the estimation of reducible background. A simple criteria was applied to reject 'ghost muons':

- Require a $\Delta R > 0.02$ between the muons. It rejects split tracks (and some low mass resonances).
- Require the non-global tracker muon to be arbitrated. It removes a large fraction of the mismatch tracks.

After these cuts, the residual contamination of 'ghost muons' in the background control region was estimated to be from 4 to 9% of the total events. It was decided to stay with this contamination, knowing that the overall background is low in $\mu$-channels and that a large uncertainty is assigned. For this analysis, we added an additional requirement, targeted to kill the remaining 'mismatch tracks' events:

- a muon is tagged as 'ghost' if it has more than 50% of shared segments.
- preference is always given to the muons passing the particle flow muon identification criteria.
- for same-sign muons with $\Delta R < 0.03$ we pick the best according to $\sigma(p_T)/p_T$. For other cases, we pick the muon with the largest number of segments. Final ambiguities, if any, are resolved by choosing the muon with highest $p_T$.
- a global muon or tracker muon with with two arbitrated matches is never cleaned.

It has been checked that the impact of all these 'ghost muons' cleaning requirements have an impact on H→ZZ→ $4\mu$ of the order of 0.03%, thus negligible.

### 3.4.4 Muon Identification

The combination of different algorithms provides a robust and efficient muon reconstruction. A given physics analysis can achieve the desired balance between identification efficiency and purity by applying a selection based on various muon identification variables. For this analysis, the *particle flow muon* selection has been used. The CMS particle-flow event reconstruction is explained in Ref. [73], which combines the information from all sub-detectors to identify and reconstruct individual particles produced in the collision.

The particle-flow event reconstruction has been done after muon reconstruction. The reconstructed muons, referred to as 'reco muons' contains a significant amount of misidentified (un-decayed) charged hadrons. In order to have a pure sample of muon candidates, identification requirements must be applied to the original 'reco muon' (tracker and global muons) collection. A standard choice of possible selections is presented in Ref. [74] and referred as soft, global and tight muon selections. The particle-flow algorithm makes use of some of these identification tools and together with the use of the measurement of energy released in the calorimeter, defines an alternative set of selections which are appropriate for and needed by the particle-flow algorithm. These selections have been optimized to identify muons in jets with high efficiency and low fake rate, as missed or fake muons can seriously bias jet and $MET$ measurements.

As a consequence, this selection is able to retain non-isolated muons, including hadron decays in flight, usually considered as a background in typical muon analyses. It is loose enough to preserve the muon efficiency, both for low-$p_T$ and high-$p_T$ muons and also emphasizes that additional muon selections can be performed after particle-flow reconstruction without any residual bias. This is achieved by applying selection criteria, which differ in strictness depending on whether the muon candidate is isolated or not, and whether its momentum is compatible with the energy deposition in the calorimeters assigned to the candidate by the particle-flow event reconstruction.

For muons that are successfully reconstructed as a track in the inner tracker, the performance of the reconstruction in the muon system and the identification criteria for particle flow muons has been measured in 2011 and 2012 data using the tag-and-probe method using di-muons from Z (for $p_T > 15$ GeV) and J/$\psi$ decays (for $p_T < 15$ GeV). The reconstruction and identification efficiency for particle flow muons measured from data, and the corresponding values obtained applying the same procedure on simulated Z and J/$\psi$ events are shown in Fig. 3.4 for 8 TeV data. The simulated events used for comparisons in the all data taking periods have been reconstructed with the same software algorithms as the data, and are weighted as function of the number of reconstructed primary vertices to match the multiplicity observed in data. The efficiencies are computed in bins of $\eta$ coverage and all data taking periods are considered together. An overall good data/MC agreement in the barrel and the endcaps is observed.

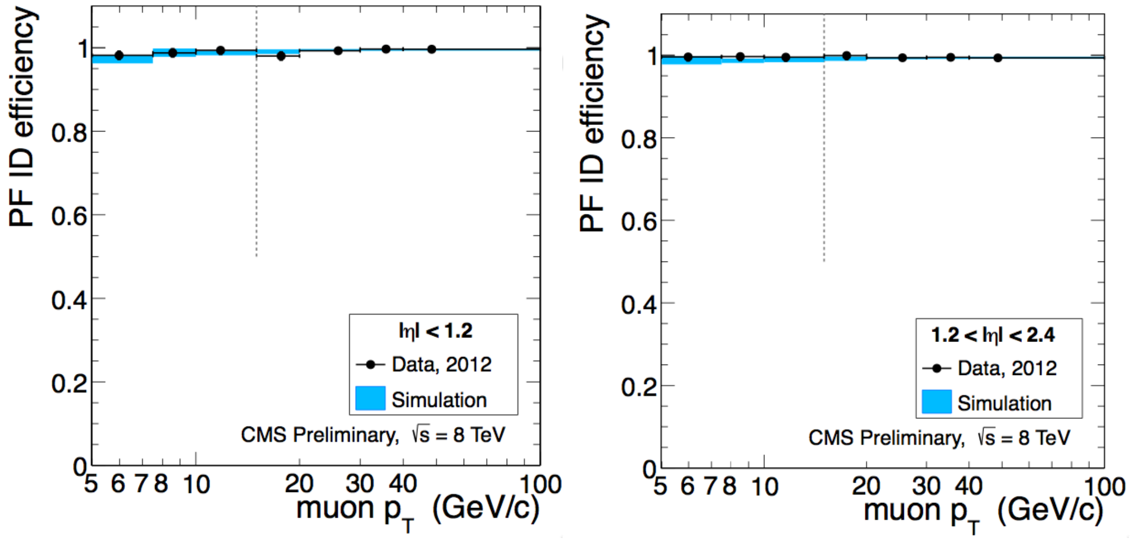


(a) (b)

Figure 3.4: Muon reconstruction and identification efficiency for particle flow muons, measured with the tag-and-probe method on 2012 data as function of muon $p_T$, in the barrel (left) and endcaps (right).

### 3.4.5 Leptons Isolation

Lepton isolation is a powerful tool to determine whether a lepton is inside or very close to a jet, and therefore to discriminate between signal and background events. In general, the muons and electrons from the H $\rightarrow$ ZZ decays are well isolated with respect to other tracks in the event. The prime idea at the base of the isolation technique is that, if one considers a certain region around the track of a reconstructed lepton, one can define an observable that quantifies the amount of energy of the particles detected into this region. Then a cut is applied on this variable.

A particle-based approach is used for the isolation of electrons and muons and particles reconstructed by the PF algorithm are used to calculate the isolation deposits around muons and electrons. Charged particles, photons and neutral hadrons are used to define the isolation variable. The relative particle flow isolation is defined by performing the scalar sum of the transverse momentum of the particle flow candidates reconstructed in a cone of $\Delta R = 0.4$, where $\Delta R = \sqrt{\Delta\eta^2 + \Delta\phi^2}$ in $(\eta, \phi)$ space and defined as:

$$\mathrm{RelPFiso} = \frac{\sum^{\mathrm{chargedhadron}} \mathrm{p_T} + \sum^{\mathrm{neutralhadron}} \mathrm{E_T} + \sum^{\mathrm{photon}} \mathrm{E_T}}{\mathrm{p_T^{lepton}}} \tag{3.2}$$

The isolation can get worsened from the extra energy from pileup entering the isolation cone due to the multiple interactions per bunch-crossing in ideal LHC conditions.

In case of electrons, the optimal efficiency in the barrel of the association of the brem clusters particle flow photons to the reconstructed particle flow electrons make possible to exploit the full cone area, while in the endcap some inefficiency in the particle flow electron identification makes necessary the usage of some internal vetoes to remove the electron footprint. Then, the particle-based isolation of a GSF electron requires the following vetoes on the candidates in the cone:

- barrel and endcap:
  1. veto all the reconstructed particle flow electrons (in the most of the cases, this requirement removes the particle flow electron correspondent to the GSF electron, with all its brem clusters).
  2. veto all the charged hadrons that share the same GSF track or the closest CTF track with the electron.
- endcap:
  1. veto all the charged hadrons in a cone $\Delta R$=0.015 around the electron.
  2. veto all the photons in a cone $\Delta R$=0.08 around the electron.

with these vetoes the footprint of the electron in both barrel and endcap is reduced to less than 1%, given in Ref. [70]. The best working point for both electrons and muons over the whole $\eta$ range was $RelPFiso < 0.4$.

The isolation efficiency has been measured on data using the tag-and-probe method for muons and electrons. The probes are identified electrons satisfying the BDT requirements as described in previous sections and muons should pass the Particle Flow identification. The passing criterion for probes is $R_{iso} < 0.4$ and $|SIP3D| < 4$, where $|SIP3D|$ is the significance of 3D impact parameter with respect to primary vertex. An overall good agreement observed between data and expectations from MC simulation as discussed in Ref. [62].

### 3.4.6 Pile up Corrections

Isolation variables are among the most pile-up sensitive variables in this analysis. Pile-up causes the mean energy deposited in the detector to increase, leading to the rise of the mean isolation values. Thus, the efficiency of a cut on isolation variables strongly depends on pile-up conditions.

In order to have a pile-up robust analysis, the isolation variable has to be corrected. The degradation of isolation performances due to pile-up can be partly mitigated associating the charged particle flow candidates to the primary vertices. It has been done by filtering the sample of charged particle flow candidates associated with the other primary vertices excluding the one with the highest $\sum p_T^2$ of the associated tracks.

However, the neutral component (neutral hadron and photons), for which this association can not be trivially done, need a special treatment. Among several correction methods, the one using `FastJet` [60, 61] energy density ($\rho$) in the event has been chosen to estimate the mean pile-up contribution within the isolation cone of a lepton. A $\rho$ variable is defined for each jet in a given event and the median of the $\rho$ distribution for each event is taken. The correction to the neutral component of the isolation variable is then applied in accord with the formula:

$$\sum_{neutral}^{corr} p_T = max\left(\sum_{neutral}^{uncorr} p_T - \rho \cdot A_{eff}, 0\ GeV\right) \tag{3.3}$$

where the effective area ($A_{eff}$ ) of a given component is defined as the ratio between the slope of the average isolation $iso$ and $\rho$ as a function of number of vertices. The latest recommendations by electron and muon physics groups has been used regarding computation of $\rho$ and $A_{eff}$. The methodology has been discussed in more detail in Sec. 3 of Ref. [62]. The muon identification efficiency as a function of the number of reconstructed primary vertices in the pile-up scenario of 2012 data taking is shown to be stable for data & MC as shown in Fig. 3.5.

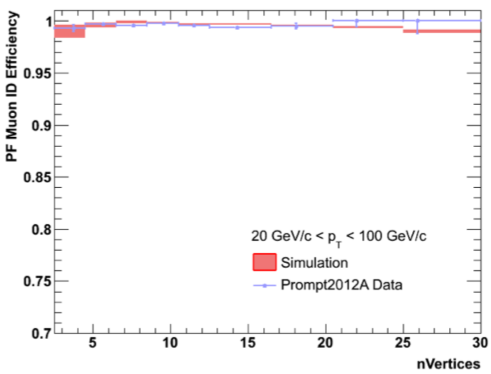


Figure 3.5: Muon reconstruction and identification efficiency for Particle Flow muons, measured with the tag-and-probe method on 2012 data as function of the number of reconstructed primary vertices.

## 3.5 Studies about the MC Simulation

MC generator level study has been performed over the most relevant background processes and the Higgs signal, which results to comprehend topological and kinematical differences among various Higgs signal and background processes of individual final states (4e, 4$\mu$, 2e2$\mu$) by understanding the signatures of relevant decays. Due to unavailability of official exclusive $Zb\bar{b}$, $Zc\bar{c}$ MC samples, a filter was developed to get these samples exclusively from inclusive Drell-Yan Z+jets samples. It differentiates heavy flavor jets (b & c) and light flavor jets (u, d, s) samples because Z+jets gives different end products depending upon the ancestral nature of jets. Basically, filter works by dealing with MC PdgId's [2] and selects at least one pair of $Zb\bar{b}$ or $Zc\bar{c}$ or Z+light jet from Drell-Yan Z+jets samples.

The efficiency of filter to select $Zb\bar{b}$, $Zc\bar{c}$ or Z+light jets from two Drell-Yan samples having different cut on invariant mass of dileptons, is reported in Tab. 3.4. It shows that contribution of Z + heavy flavor jets (b/c) is directly proportional to cut on invariant mass of di-leptons, that is applied while generating the events, so the Z + heavy flavor contribution increases with increasing the invariant mass of di-leptons. The use of exclusive samples result as more precise understanding or measurements of the individual background processes in $4\ell$ signal region. The filter considers partons [3] from following ancestral origins:

- **Matrix Element**

  - status 3 parent with precisely 2 'grandparents' that has the same identity as the status 2 parton in question. This is not the actual ultimate progenitor, but this is the signature of matrix element decays. The ultimate progenitor is the parent of the status 3 parton.

- **Flavor Excitation**

  - almost the same as the matrix element classification, but has only one outgoing parton product instead of two.

- **Gluon Splitting**

  - parent is a quark of a different flavor than the parton in question, or a gluon, which can come from either initial state radiation or final state radiation.

[2] It is a particle identity number assigned by Particle Data Group in cooperation with Monte Carlo authors.

[3] In current study, it is a status 2 quark, typically b or c. The status convention can change in accord with MC generator used.

- **True Decay**

  - decays from a resonance like top, Higgs, etc.

Table 3.4: Filter efficiency for two different Drell-Yan samples.

| DYJetsToLL-TuneZ2-M-50_7TeVmadgraph-tauola | |
|---|---|
| **Flavor** | **Efficiency (%)** |
| $Zb\bar{b}$ | 4.45 |
| $Zc\bar{c}$ | 24.65 |
| Z + jets | 70.88 |
| DYJetsToLL_M-10To50_TuneZ2_7TeV-madgraph | |
| $Zb\bar{b}$ | 2.06 |
| $Zc\bar{c}$ | 25.47 |
| Z + jets | 72.45 |

### 3.5.1 Key Observables from MC Simulation

The production mechanism of background samples contributing in $4\ell$ signal phase space has been explained briefly in Sec. 1.4. The detailed understanding of various kinematical observables at MC generator level is required to understand and estimate the background contribution in Higgs signal phase space. The comprehensive review of various physics observables helps to find effective discriminants for signal to background rejection or it can lead to the development of new observables which can be used to get better control over backgrounds.

The MC generator level analysis have contributed to design the analysis strategy. In order to comprehend the final state topologies and distributions of important physics observables, I have studied the $Zb\bar{b}$, $Zc\bar{c}$, Z+jets, $t\bar{t}$, WZ+jets and the Higgs signal samples individually.

Each sample was divided in different classes corresponding to their individual decay modes and relevant final state topologies. In order to build four leptons candidates from the Higgs signal, ZZ, $Zb\bar{b}$, $Zc\bar{c}$ and Z + light jet(s) events, I have defined main classes of events as follows:

- In case of Higgs signal and *irreducible ZZ background*, each Z is decaying to di-leptons, giving four leptons as final state.

- The two opposite sign same flavor (OSSF) leptons came from Z in case of reducible backgrounds ($Zb\bar{b}$ & $Zc\bar{c}$) while other 2 leptons were considered from $b\bar{b}$, $c\bar{c}$ decay chain. In case of $t\bar{t}$, two OSSF leptons came from $W^+/W^-$ and other two leptons taken from decay chain of $b\bar{b}$.

- The heavy flavor quarks ($b$, $\bar{b}$, $c$ or $\bar{c}$) don't decay directly to leptons so depending upon their branching ratio to end up as leptons, other two leptons have been considered from decay chain of $D^+$, $D^-$, $D^0$, $\bar{D}^+$, $D_s^+$, $D_s^-$, $B^+$, $B^-$, $B^0$, $B_s^0$ mesons for the formation of four lepton candidate.

- In case of WZ+jets, two OSSF leptons considered from Z decay, $3^{rd}$ lepton from $W^+/W^-$ and $4^{th}$ lepton is selected as any stable lepton without any ancestral requirement. Z+light jets can give four leptons at MC level by considering two OSSF leptons from Z decay and other two leptons were selected similarly as $4^{th}$ lepton of WZ+jets.

One of the main focus was to understand mutual differences of important kinematical observables ($p_T, \phi, \eta$, energy, invariant mass of di-leptons & four leptons etc.) in case of background and Higgs signal samples.

The invariant mass distribution of four lepton candidates built from individual background processes and Higgs signal is shown in Fig. 3.6. The contribution of each signal and background process is normalized to unity. The long tails displayed by contributing samples towards low mass region are due to the contribution of underlying events, which can give more than one $4\ell$ combinations from an event. Secondly, the leptons considered to make $4\ell$ candidates are not required to cross any $p_T$ threshold, so low $p_T$ leptons results as the formation of low mass $4\ell$ candidate. In low mass range, the four lepton mass spectrum is mostly populated with $4\ell$ candidates coming from individual background processes. It makes very challenging task to differentiate the signatures of Higgs signal from corresponding background processes for low mass Higgs searches.

In parallel, it displays the impulse to development of effective background estimation methodologies by paying particular attention to low mass Higgs searches, where mass of four lepton candidate can act as an important discriminant. On the way to the development of effective discriminators to get better signal to background rejection, additional physics observables have been studied for SM or electroweak processes contributing in $H \rightarrow ZZ^* \rightarrow 4\ell$ phase space, as given below:

- Transverse momentum distribution of four lepton candidates built from corresponding background and Higgs Signal samples is shown in Fig. 3.7 but it is not offering better signal to background rejection.

- Fig. 3.8 shows the transverse momentum distributions of the four highest $p_T$ leptons in an event for all considerable background processes along with 3 Higgs signal samples, having masses $m_H = 125$ GeV/c$^2$, $m_H = 200$ GeV/c$^2$,

$m_H = 350$ GeV/c$^2$. It is observed that leptons coming from direct Z decays or W decays have highest $p_T$ as compared to other leptons which are actually mis-identified jets or coming from long decay chains of b, $\bar{b}$, c or $\bar{c}$ quarks.

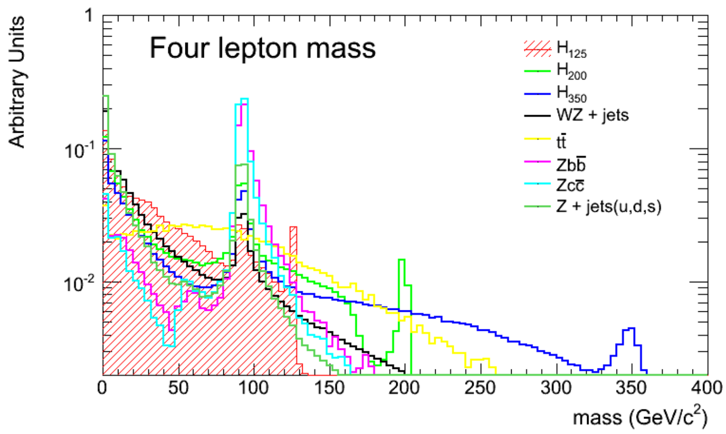


Figure 3.6: Four lepton's invariant mass distribution for significant background processes in context of H $\rightarrow$ ZZ$^*$ $\rightarrow 4\ell$ along with 3 Higgs signal samples.

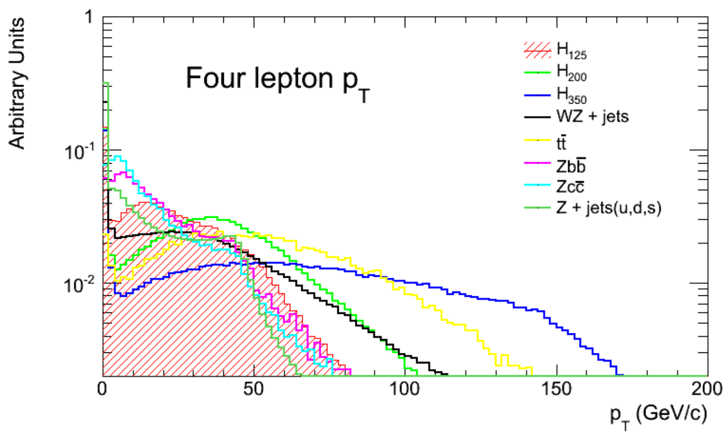


Figure 3.7: The transverse momentum distribution of four lepton candidates for relevant background processes in context of H $\rightarrow$ ZZ$^*$ $\rightarrow 4\ell$ along with 3 Higgs signal samples.

MC studies contributed to select most efficient physics observables like $p_T$, invariant mass of four leptons etc. These physics observables are used as discriminating tools while reconstructing the Higgs signal or background final states for getting better signal to background rejection and to improve the relative Higgs signal selection efficiency as well.

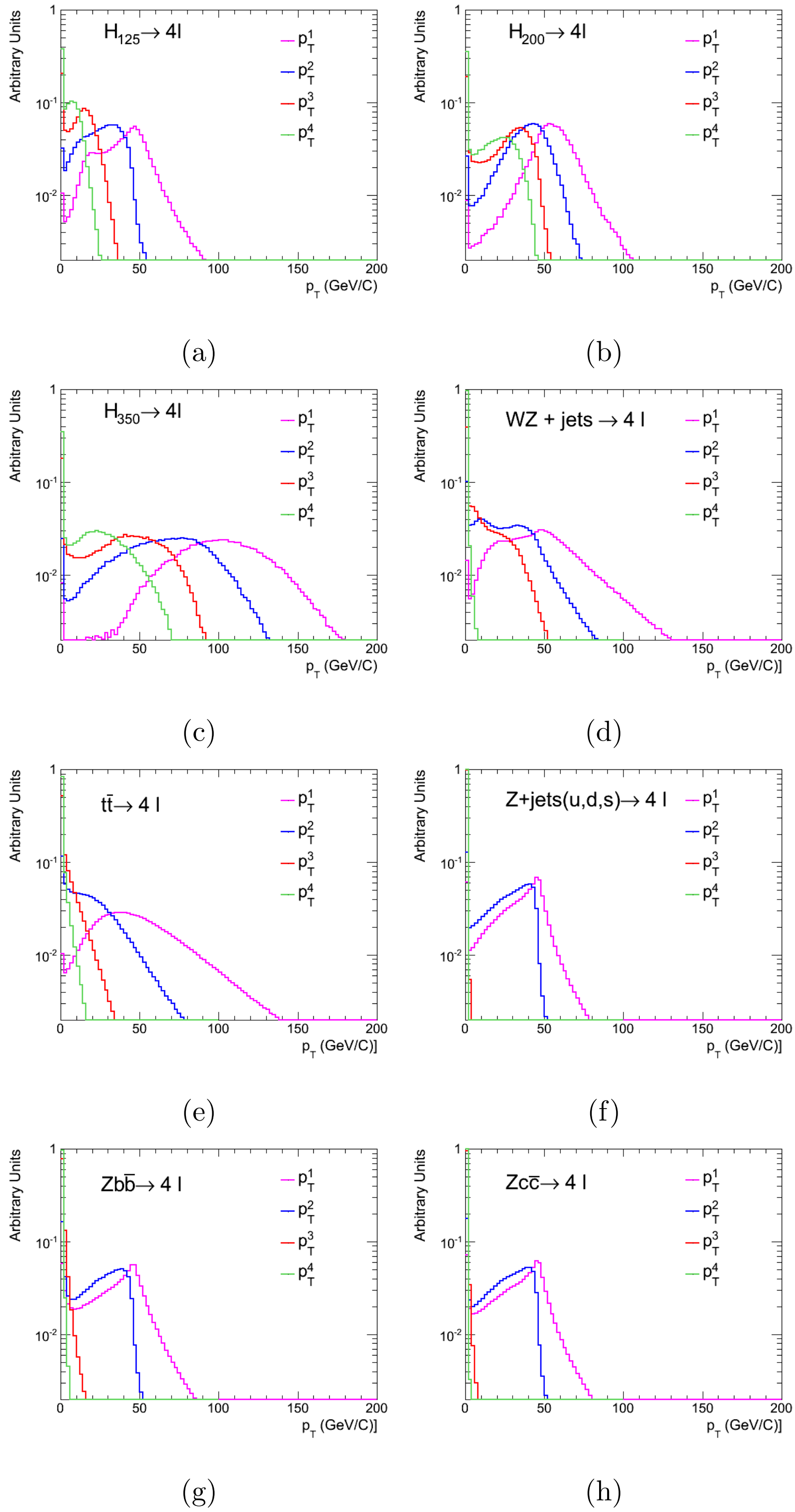


Figure 3.8: Transverse momentum distributions of 4 highest $p_T$ leptons in an event for $\mathrm{m_H} = 125\ \mathrm{GeV/c^2}$ (a), $\mathrm{m_H} = 200\ \mathrm{GeV/c^2}$ (b), $\mathrm{m_H} = 350\ \mathrm{GeV/c^2}$ (c), $\mathrm{WZ + jets}$ (d), $\mathrm{t\bar{t}}$ (e), $\mathrm{Z + light\ jets\ (u, d, s)}$ (f), $\mathrm{Zb\bar{b}}$ (g) and $\mathrm{Zc\bar{c}}$ (h).

# Chapter 4

# Event Selection & Background Control

The accurate control and evaluation of considerable background processes in respective decay mode of Higgs boson plays a key role to derive the reliable results. On the way to the estimation of background processes in H$\to$ ZZ$^*$ $\to 4\ell$ decay channel, proper understanding of the properties of the Higgs signal is equally important for the precise evaluation of background processes in signal phase space.

The prime motive of current chapter is to get a better signal to background rejection as well as to increase the Higgs signal selection efficiency. It will present the development of event selection strategy to analyze the real data events like backgrounds of H$\to$ ZZ$^*$ $\to 4\ell$ decay channel and to estimate their contribution in signal phase space. In parallel, the event selection technique for physics analysis of the data in context of Higgs signal phase space of H$\to$ ZZ$^*$ $\to 4\ell$ will be presented.

The studies presented in succeeding sections have been performed over proton-proton collision data recorded by the CMS detector at the LHC, corresponding to integrated luminosities of 5.05 fb$^{-1}$ @ $\sqrt{s} = 7$ TeV (2011) and 12.21 fb$^{-1}$ @ $\sqrt{s} = 8$ TeV (2012) collected by the CMS detector during 2011 & 2012. More details about Data & MC samples have been presented in Sec. 3.3.

## 4.1 General Event Selection

Some important distributions of physics observables in context of Higgs signal and background processes have been shown in Chapter 3. Those studies have contributed in the development of event selection strategy for Higgs signal and background phase spaces along with dedicated studies about leptons reconstruction, isolation, identification and measurements (see Sec. 3.4 & Sec. 3 of [62]).

The event selection starts by the requirement of at least one good primary vertex (PV) fulfilling the following criteria:

- high number of degree of freedom ($N_{PV} > 4$),
- collisions restricted along the $z-$axis ($z_{PV} < 24$ cm),
- small radius of the PV ($r_{PV} < 2$ cm).

On the basis of the studies performed over the lepton's performances on simulation and data, choices have been made to define the 'leptons candidates' that will be used in the current analysis. The analysis selections will act over *loose leptons* and *good leptons* as described below:

**Good leptons**: Some additional quality selections have been imposed over *loose leptons* to extract good leptons, which gives leptons whose ancestral origin could be most likely a Higgs signal. The uses of *good leptons* contributes to reject leptons from background-like ancestral origins. The corresponding quality selections are given below:

- electrons should pass the electron identification criteria as described in Sec. 3.4.2 and muons should meet the particle flow muons requirements (see Sec. 3.4.4).
- relative particle flow isolation should be less than 0.4 (see Sec. 3.4.5).
- the significance of the impact parameter to the event vertex, $\mathrm{SIP_{3D}}$, is required to satisfy $\mathrm{SIP_{3D}} = \frac{|\mathrm{IP}|}{\sigma_{\mathrm{IP}}} < 4$ for each lepton, where IP is the lepton impact parameter in three dimensions at the point of closest approach with respect to the primary interaction vertex and $\sigma_{\mathrm{IP}}$ is the associated uncertainty.

**Loose leptons**: The lepton's quality criterion have been relaxed to get loose leptons. This class of leptons is used in the estimation of reducible & instrumental backgrounds (see Sec. 4.3.2) and should fulfill below mentioned requirements:

- electrons should be within the geometrical acceptance of $|\eta^e| < 2.5$, with $p_T^e > 7\ GeV/c$ having 0 or 1 expected missing inner hits.
- muons (global or tracker) should satisfy $|\eta^\mu| < 2.4$, $p_T^\mu > 5\ GeV/c$.
- both electrons and muons should satisfy loose requirements on the transverse ($d_{xy} < 0.5$ cm) and longitudinal ($d_z < 1$ cm) impact parameter with respect to the primary vertex.

- non-global tracker muons must be arbitrated[1].
- it is required that $\Delta R > 0.02$ between the leptons to be sure that they are well separated.

An $e/\mu$ cross cleaning procedure is applied before building *good leptons* candidates. *Loose electrons* are discarded if they satisfy $\Delta R(e, \mu) < 0.05$, where the muons considered are *loose muons* passing Particle Flow or Global muons criterion.

The event selection sequence have to run on those events which are passing the above mentioned selection cuts. The objective of this selection sequence is:

- to preserve the Higgs signal as much as possible.
- to bring down the QCD multi-jets and Z/W + light jets contributions to a level comparable to, or below, the contribution of the main backgrounds in this analysis, namely the reducible ($t\bar{t}$, $Zb\bar{b}/Zc\bar{c}$) and the irreducible $ZZ^*$.

This has to be done while preserving the maximal signal selection efficiency as well as developing the phase space to define control regions enriched in background events for the evaluation of background processes. By reducing the number of extra leptons in signal-like events, it allows to solve the problem of combinatorial ambiguities caused by the presence of more than four leptons in an event. It consists of a selection of the final set of four leptons through minimal identification and transverse momentum requirements, loose isolation and kinematic cuts.

### 4.1.1 Final State Radiation Recovery

A Z decay into a lepton pair can be accompanied by final state radiation (FSR), $Z \to \ell^+\ell^-\gamma$. If the photon transverse momentum, $p_T^\gamma > 2$ GeV/$c$ then about 8% (15%) of the Z decays in to muons (electrons) are affected. The detailed methodology of FSR recovery technique, including photon reconstruction, identification and isolation has been mentioned in detail in Sec. 5 of Ref. [62]. As the photon emission is most often collinear with one of the leptons, electron measured energies automatically include the energy of a large fraction of the emitted photons in the associated electromagnetic super-cluster because of electron's reconstruction algorithm.

On the other hand, muon measured momenta do not include the contribution coming from emitted photons. Final state radiation is therefore expected to degrade

[1] *Arbitration* is a set of selections, which is developed to solve the pattern recognition problem of assigning segments to tracks because sometimes two (or more) tracks are very near to each other and it is quite possible that the same segment or set of segments is associated to more than one track. This can happen for muons in jets. The methodology about 'Arbitration algorithm' is discussed in Ref. [63]

the Z mass resolution when measured with the sole muon pairs, and in turn degrade the Higgs boson mass resolution when measured with the four leptons momenta, especially in the $4\mu$ and in the $2e2\mu$ final states and, to a lesser extent, in the 4e final state. It is also expected to reduce the efficiency of the lepton isolation cut when the emitted photon is in the lepton isolation cone.

An excellent Higgs boson mass resolution and a large selection efficiency are essential ingredients in view of the small production cross section in the $4\ell$ channels, in particular to discriminate the Higgs boson signal from the ZZ continuum. It is necessary to recover the FSR photons with large efficiency and purity, to remove the energy of the recovered photons from the lepton isolation cones, and to measure the mass of the Higgs boson candidate from the momenta of the leptons and the recovered photons. An efficient recovery thus requires photon identification and reconstruction in the vicinity of other particles, down to photon transverse momenta of the order of the Higgs mass core resolution, *i.e.* down to a couple of GeV/$c^2$. Less energetic photons are expected to degrade the mass resolution in an insignificant manner, and are increasingly difficult to reconstruct and separate from the background.

The way to build Z candidates with or without FSR photon is defined in Sec. 4.1.2. The FSR algorithm have been studied in detail over data in context of Z decays in two or four leptons and in topologies compatible with the Z + X reducible background hypothesis (see Sec. 5 of Ref. [62]). Significant improvement is observed in the reconstruction of the Z peak from data as it becomes steeper. The observed rate on Z→ $\ell\ell$ events is 1.9% while the efficiency gain is 0.9%. The performance of the FSR recovery algorithm in accord with individual final states is shown in Tab. 4.1 with corresponding rate, purity and efficiency gain for signal and background.

Table 4.1: Rate, purity and efficiency gain for signal and ZZ background.

| final state | rate (%) | purity (%) | efficiency gain |
|---|---|---|---|
| H→ ZZ(all) | 6.0 | 80 | 2.0 |
| H→ ZZ → $4\mu$ | 9.1 | 82 | 3.0 |
| H→ ZZ → $2e2\mu$ | 5.0 | 78 | 0.6 |
| H→ ZZ → 4e | 1.4 | 72 | 1.8 |
| SM ZZ (all) | 6.7 | 81 | 2.1 |
| SM ZZ → $4\mu$ | 10.1 | 83 | 3.0 |
| SM ZZ → $2e2\mu$ | 6.5 | 77 | 0.6 |
| SM ZZ → $4e$ | 1.8 | 72 | 1.8 |

### 4.1.2 Z Boson Reconstruction

In accord with present analysis and production modes of contributing SM and electroweak processes (see Sec. 1.4), at least one Z boson can be reconstructed in each sample. The event selection methodology begins by reconstructing a Z boson by following two approaches in accord with FSR photon availability:

**Without FSR Photon:** It is also known as the *'default way'* to get Z boson and it is reconstructed from:

- a pair of *'good lepton'* candidates having opposite charge and matching flavor ($e^+e^-$, $\mu^+\mu^-$).
- reconstructed mass $m_{\ell\ell}$ should be closest to the nominal Z boson mass (taken here to be 91.2 GeV/$c^2$) and denoted as $Z_1$.
- the invariant mass of selected di-lepton pair should be more than 40 $GeV/c^2$ and less than 120 $GeV/c^2$.

**With FSR Photon:** If a FSR photon candidate is selected in an event, the isolation sum may have to be modified and FSR recovery technique (see Sec. 4.1.1) needs to be implemented for the Z boson reconstruction. In the present work, only photons with $p_T^\gamma > 2$ GeV/c and well in the tracker acceptance ($|\eta| < 2.4$) are considered, and tentatively assigned to a lepton and to a Z candidate. The association to a lepton goes as follows:

- photons are considered only if the minimum $\Delta R$ distance with respect to any of the $Z$ leptons is smaller than $< 0.5$.
- if the distance of the photon to the closest lepton is between 0.07 and 0.5, the probability that this photon arise from pile-up or, to a lesser extent, from an underlying event, becomes appreciable, because of the large annulus area. To enrich the photon sample in genuine FSR photons, the $p_T^\gamma$ cut is tightened to 4 GeV/$c$ and the photon is required to be somewhat isolated from other particles:
  - the relative PF isolation including pileup contribution is required to be smaller than 1.0.
- for selecting pair with $m_{\ell\ell}$ closest to nominal Z mass, make di-lepton pairs from leptons passing ID and SIP cuts, but not yet isolation cut.
- for each photon attached that has either lepton of the Z candidate as closest lepton, test if the $\ell\ell + \gamma$ candidate would satisfy the two criteria:
  - the invariant mass of $m_{\ell\ell\gamma}$ should be more than 4 GeV/c$^2$ and less than 100 GeV/c$^2$.

  - $|m_{\ell\ell\gamma} - 91.188| < |m_{\ell\ell} - 91.188|$.
- if multiple photons satisfy these criteria, then best one is selected in accord with below mentioned logic:
  - if there's at least one photon with $p_T > 4$ GeV/c, pick the one with highest $p_T$.
  - if all photons have $p_T < 4$ GeV/c, pick the one that has the smallest $\Delta R$ to its closest lepton.
- if a FSR photon was selected, exclude that photon from the photon isolation sum of the lepton of that Z, if it was in the isolation cone and outside the isolation veto.
- both leptons should pass the isolation requirement and corresponding $Z\rightarrow\ell\ell$ or $Z\rightarrow\ell\ell\gamma$ will be considered as Z boson for further analysis.
- it implies that the choice of the best Z1 is done only out of Z1 candidates for which both leptons satisfy the isolation criteria, and the same happens for Z2.
- the invariant mass of $m_Z$ should be more than 40 GeV/c$^2$ and less than 120 GeV/c$^2$.

The Z boson reconstruction in above mentioned way ensures that the leptons in the preselected events are on the high efficiency plateau for the trigger. The reconstructed Z mass peak ($Z \rightarrow ee$ and $Z \rightarrow \mu\mu$) has been shown in Fig. 4.1 for 7 & 8 TeV, which is displaying a good Data-MC agreement. The contribution of Z+light jet sample is higher in $Z\rightarrow ee$ case as compared to $Z\rightarrow \mu\mu$ because the probabilities of electrons to be faked by jets is higher as compared to muons, which results as a wider Z peak in case of $Z\rightarrow ee$ decay. The background control samples for the Z+jet, $Zb\bar{b}/c\bar{c}$ and $t\bar{t}$ backgrounds are obtained as subsets of the event sample that remain after the Z boson reconstruction. In other words, after this step, the analysis strategy is divided in methods for two different phase space as:

- Irreducible ZZ and Higgs signal (see Sec. 4.2).
- Reducible & Instrumental backgrounds (see Sec. 4.3.2).

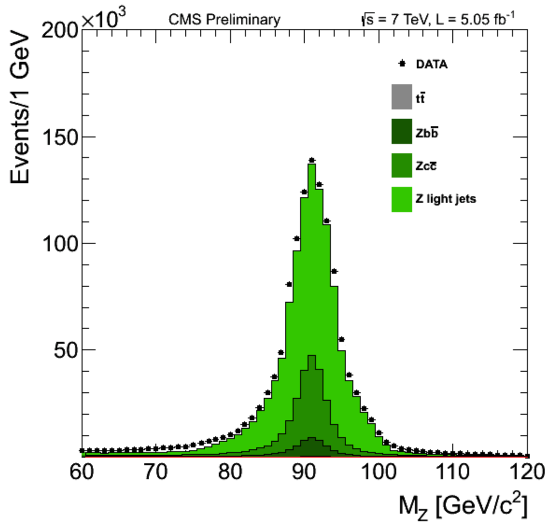


(a)

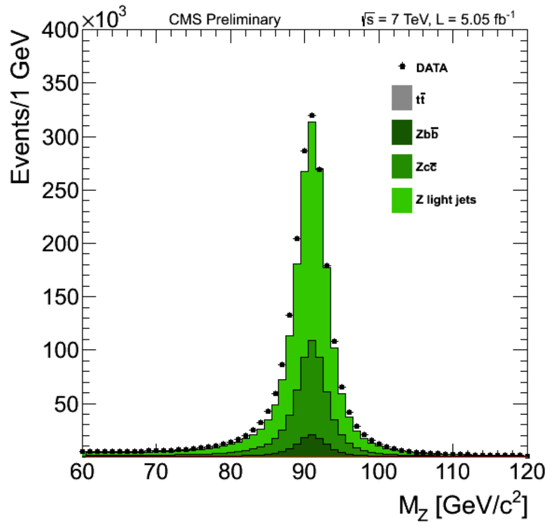


(b)

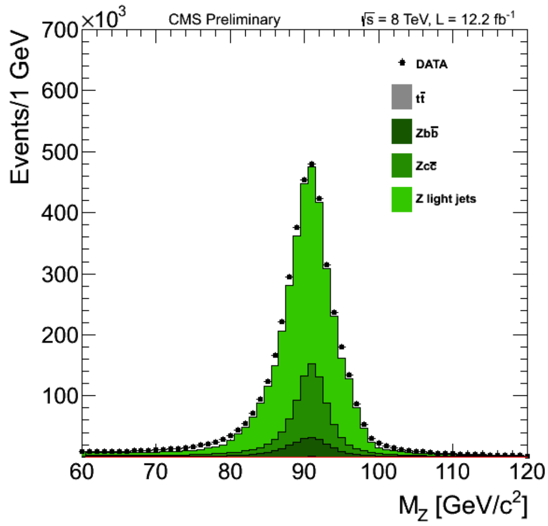


(c)

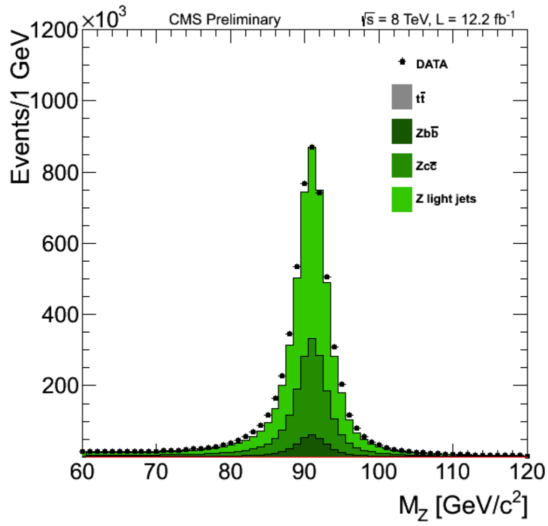


(d)

Figure 4.1: Comparison of Z1 invariant mass in (a) ee 7 TeV, (b) $\mu\mu$, 7 TeV (c) ee 8 TeV, (d) $\mu\mu$, 8 TeV, between data and Monte Carlo expectations. The samples correspond to data collected in 2011 ($\mathcal{L} = 5$ fb$^{-1}$ @ 7 TeV) and 2012 ($\mathcal{L} = 12.21$ fb$^{-1}$ @ 8 TeV)

.

## 4.2 Irreducible ZZ and Higgs signal Phase space

It has been shown in Sec. 1.4 that experimental signatures of ZZ continuum are similar with the Higgs boson signal samples, so the ZZ continuum will be estimated directly in Higgs signal phase space. The analysis rely on MC simulation to evaluate the ZZ background contribution in signal phase space. After getting one reconstructed Z boson (as given in Sec. 4.1.2), the further analysis will follow the below mentioned selection steps:

1. **Three or more leptons**: another *good lepton* candidate of any flavor or charge is required.
2. **Four or more leptons and a matching pair**: a fourth *good lepton* candidate with the flavor of the third lepton candidate from the previous step, and with opposite charge is added.
3. **Choice of the 'best $4\ell$' and $Z_1$, $Z_2$ assignments:** make a second lepton pair known as $Z_2$ from all the $\ell^+\ell^-$ combinations remaining after $Z_1$ selection.
    - the invariant mass of selected pair should be more than 4 GeV/c$^2$ and less than 120 GeV/c$^2$.
    - if more than one $Z_2$ combination satisfies above criteria, the one built from leptons of highest $p_T$ is chosen.
    - it is required that any two leptons from the four selected should have $p_{T,i} > 20$ GeV/c and $p_{T,j} > 10$ GeV/c.
4. **QCD suppression**: the reconstruction mass of opposite-sign and same-flavor lepton pairs must satisfy $m_{\ell\ell} > 4$ GeV/c$^2$.
5. **$\mathbf{m_{4\ell}}$, Z and $\mathbf{Z^{(*)}}$ kinematics:** In accord with various ranges of cuts over $m_{4\ell}$, $m_{Z1}$ and $m_{Z2}$, three sets of kinematic cuts are introduced to maximize the sensitivity in different ranges of Higgs boson mass hypothesis and to measure ZZ continuum as well:
    - **$Z \rightarrow 4\ell$ phase space:** The invariant mass of $m_{Z1}$ should be more than 40 GeV/c$^2$ and less than 120 GeV/c$^2$, whereas $m_{Z2}$ is required to stay in 4 GeV/c$^2$ to 120 GeV/c$^2$. The mass window for $m_{4\ell}$ is from 70 GeV/c$^2$ to 110 GeV/c$^2$.
    - **Baseline Higgs phase space:** It is defined by requiring mass window over $m_{Z1}$ from 40 GeV/c$^2$ to 120 GeV/c$^2$ and $m_{Z2}$ should stay in between 12 GeV/c$^2$ and 120 GeV/c$^2$. The corresponding $m_{4\ell}$ should be greater than 100 GeV/c$^2$. This selection provides the best sensitivity for masses $m_{\mathrm{H}} < 130$ GeV/c$^2$

- **High-mass phase space:** This region is sensitive for ZZ cross section measurement and high mass Higgs searches. It is defined by requiring $m_{Z1}$ and $m_{Z2}$ between 60 GeV/$c^2$ to 120 GeV/$c^2$. The corresponding $m_{4\ell}$ should be greater than 100 GeV/$c^2$.

The first step allows for control of the three-lepton event rates which include WZ di-boson production events. The first three steps are designed to reduce the contribution of the instrumental backgrounds from QCD multi-jets and Z + jets, whilst preserving the maximal signal selection efficiency and the phase space for the evaluation of background systematics.

One of the main focus to select $3^{rd}$ and $4^{th}$ leptons as *good leptons* is to reject leptons coming from the decays of the heavy flavor jets (b,c). Such leptons are likely to be accompanied by hadronic products from the fragmentation and decay processes initiated in the b-quark jets. Moreover, because of the long lifetime of b-hadrons, they are likely to have a large impact parameter with respect to the primary vertex. In general, lepton isolation and lepton impact parameter measurements allow for a powerful rejection of reducible backgrounds.

By reducing the number of jets misidentified as leptons, fewer combinatorial ambiguities arise when assigning the leptons to candidate Z bosons. The choice of the best combination of four leptons completes the first three steps. The step four contributes for killing low mass resonances as well as multiple hadron decays.

The events satisfying the high-mass selection are a subset of those satisfying the baseline selection. The enlarged phase space of the baseline selection for the Higgs boson signal is needed at very low masses given the very small cross section $\times$ branching ratio, at the price of a larger background. The increased acceptance for the signal becomes small for mass ($< 10\%$ in relative compared to the baseline selection) above $\approx 130$ GeV/$c^2$ where reducing the phase space to better suppress the background become advantageous. For Higgs boson masses above $\approx 2 \times m_Z$, further restricting the phase space of the pair of Z boson can be made without significant loss of acceptance for the signal, with the benefit of a slight reduction of the $ZZ^*$ background.

Fig. 4.2 and 4.3 are showing the status of all dominant background processes along with Higgs signal in accord with selection chain as described above for 4e, $4\mu$, $2e2\mu$ final states at 7 and 8 TeV respectively. A continuos decrement of contributing background processes is observed with each selection cut and a reasonable agreement is achieved between data and simulated samples of signal and background for three final states.

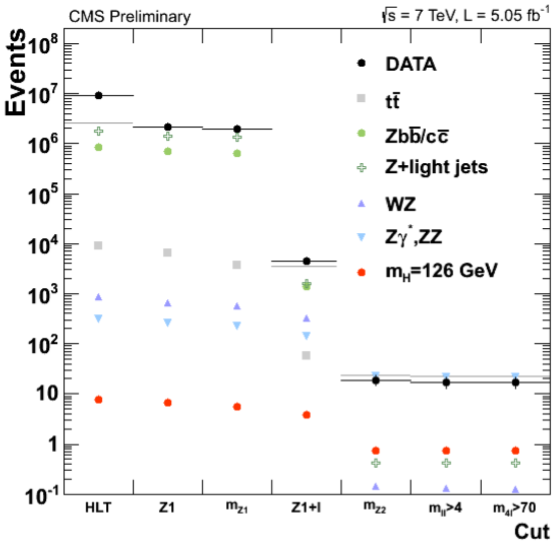


(a)

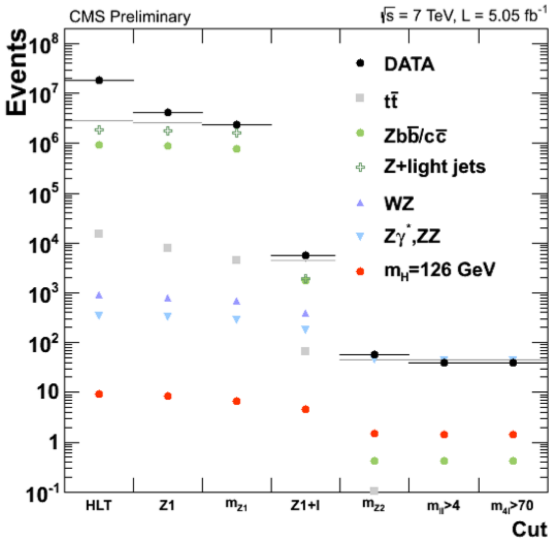


(b)

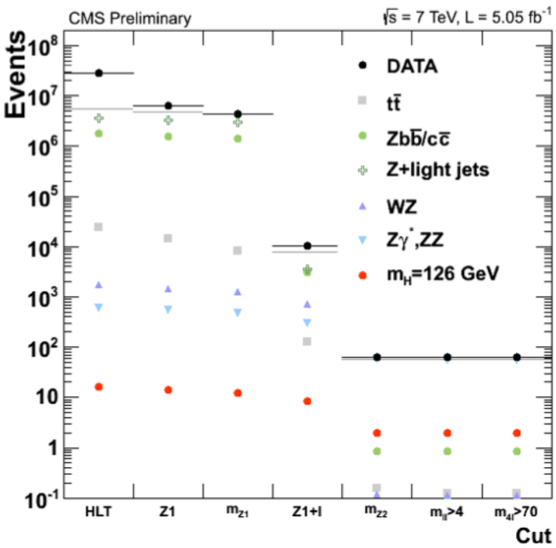


(c)

Figure 4.2: Event yields in the (a) 4e, (b) $4\mu$ and (c) $2e2\mu$ channels as a function of the event selection steps. The MC yields are not corrected for background expectation. The samples correspond to data collected in 2011 $\mathcal{L} = 5.05$ fb$^{-1}$ @ 7 TeV.

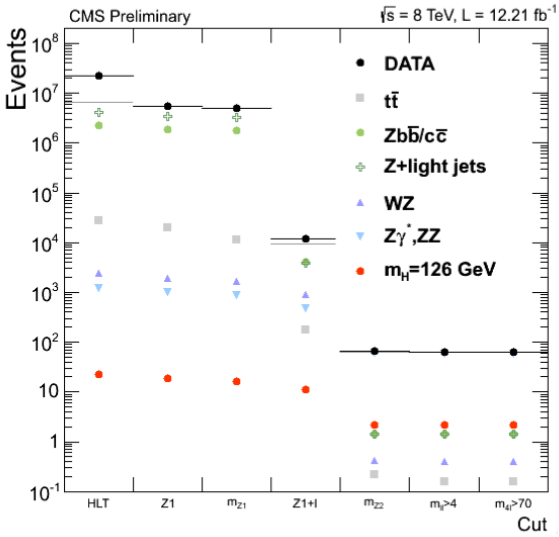


(a)

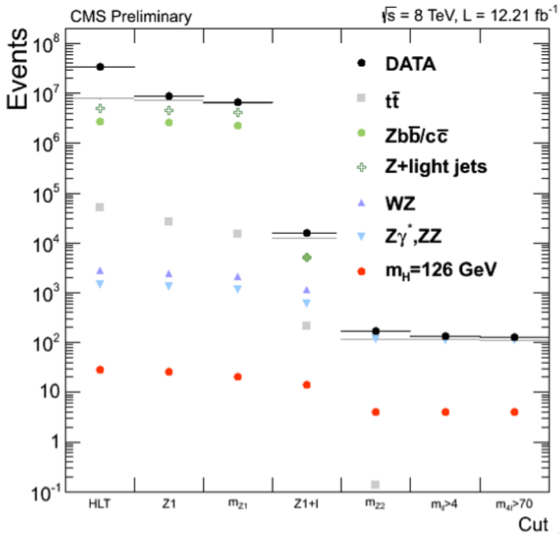


(b)

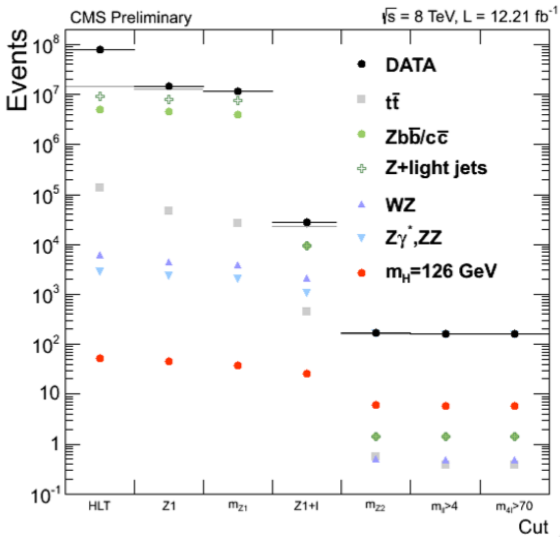


(c)

Figure 4.3: Event yields in the (a) 4e, (b) $4\mu$ and (c) $2e2\mu$ channels as a function of the event selection steps. The MC yields are not corrected for background expectation. The samples correspond to data collected in 2012 $\mathcal{L} = 12.21$ fb$^{-1}$ @ 8 TeV.

## 4.3 Background Evaluation and Control

The low branching ratio of $H \rightarrow ZZ^* \rightarrow 4\ell$ decay channel and small number of observed events in Higgs signal region, requires a precise evaluation of the background processes. The analysis relies on other methods, based on experimental data, for the control of the background and the evaluation of associated systematic uncertainties.

In accord with the event yields evaluated from MC simulations, the background is overwhelmingly composed of the $ZZ^*$ continuum. Only a small contamination remains from the reducible and instrumental backgrounds. The $t\bar{t}$ and WZ backgrounds appear negligible, i.e. they both represent $< 1\%$ of the total background rate expected for the baseline selection. The MC event yields in Higgs signal region do not allow to conclude on the situation for Z+light jets, and $Zb\bar{b}/Zc\bar{c}$ backgrounds because of less MC statistics. These backgrounds must be evaluated from data. In particular the small contamination from Z + light jets and $Zb\bar{b}/Zc\bar{c}$ which is expected to be concentrated mostly at low $m_{4\ell}$ is considered (see Fig. 3.6).

The typical procedure to evaluate background from data, consists of choosing a wide background control region outside the signal phase space, which gets populated by relaxing the event selection cuts and verifies that the event rates in data change according to the expectation from simulation. If a specific background contribution has to be determined, the corresponding control region must be chosen carefully since any of the other reducible backgrounds might rapidly become dominant if the event selection is relaxed, thus making the extrapolation to the signal phase space difficult.

### 4.3.1 Evaluation of the $ZZ^*$ Continuum

The number of expected events from continuum production of ZZ, from the processes $q\bar{q} \rightarrow ZZ$ and $gg \rightarrow ZZ$, are estimated from simulation as well as their PDFs for the 4 lepton invariant mass that is used in the fit to extract the signal. The NLO cross sections has been used for these processes, which are reported in Tab. 3.3. The analysis selection was implemented on these simulated processes to get the expected event yields, separately for 7 TeV and 8 TeV.

#### 4.3.1.1 ZZ Event Yield

The expected rate in any given four leptons mass range $[m_1, m_2]$ is obtained directly from the absolute rate predicted by the MC model simulation:

$$N^{\mathrm{ZZ}}_{\mathrm{expect}}\,[m_1, m_2] = \int_{m_1}^{m_2} \left(\frac{dN}{dm_{4\ell}}\right)_{\mathrm{MC}} dm_{4\ell} \tag{4.1}$$

When used for comparisons with data, the method is affected by the full systematics uncertainties on the pp integrated luminosity and the theory errors as well as systematic errors on acceptance within analysis cuts.

#### 4.3.1.2 Model for ZZ continuum background

For ZZ background estimation, a functional form has been used as described in Ref. [62], that models the raising of the phase space at the kinematical threshold of the two Z bosons, and the flat phase space below such threshold. So the $pp \to ZZ \to 4\ell$ backgrounds are modeled using the functional form very similar to that of the signal:

$$qq \to \mathrm{ZZ@NLO}: \frac{dN}{dm_{4\ell}} = C(m_{4\ell}) \cdot N^{MC}(m_{4\ell}) \cdot F_{ZZNLO}(m_{4\ell}), \tag{4.2}$$

$$\mathrm{gg} \to \mathrm{ZZ}: \frac{dN}{dm_{4\ell}} = C(m_{4\ell}) \cdot N^{MC}(m_{4\ell}) \cdot F_{gg2ZZ}(m_{4\ell}). \tag{4.3}$$

where the overall data-to-MC correction factors $C(m_{4\ell})$ are assumed to be the same as for the Higgs events with $m_H = m_{4\ell}$. The validity of this assumptions is addressed later in section on systematic errors (see Sec. 5.1.1).

The functions $F_{ZZNLO}(m_{4\ell})$ and $F_{gg2ZZ}(m_{4\ell})$ are parameterized separately for $4e$, $4\mu$, and $2e2\mu$ using the simulated distributions as follows:

$$f_1(m, \vec{a}) = \left(0.5 + 0.5\mathrm{erf}\left(\frac{\mathrm{m} - \mathrm{a}_1}{\mathrm{a}_2}\right)\right) \cdot \frac{a_4}{1 + e^{(m-a_1)/a_3}} \tag{4.4}$$

$$f_2(m, \vec{b}) = \left(0.5 + 0.5\mathrm{erf}\left(\frac{\mathrm{m} - \mathrm{b}_1}{\mathrm{b}_2}\right)\right) \cdot \left(\frac{b_4}{1 + e^{(m-b_1)/b_3}} + \frac{b_6}{1 + e^{(m-b_1)/b_5}}\right) \tag{4.5}$$

$$f_3(m, \vec{c}) = \left(0.5 + 0.5\mathrm{erf}\left(\frac{\mathrm{m} - \mathrm{c}_1}{\mathrm{c}_2}\right)\right) \cdot \frac{c_4}{1 + e^{(m-c_1)/c_3}} \tag{4.6}$$

$$F_{ZZNLO}(m, \vec{a}, \vec{b}, \vec{c}) = f_1 + f_2 + f_3 \tag{4.7}$$

$$F_{gg2ZZ}(m, \vec{a}, \vec{b}, \vec{c}) = f_1 + f_2 \tag{4.8}$$

The studies about $ZZ$ background shape fits are shown in Fig. 4.4; which didn't find any systematic uncertainties that would distort the $ZZ \to 4\ell$ mass distributions in a substantial way over the mass range corresponding to the Higgs boson width. Therefore, all uncertainties on the $ZZ$-background are included as uncertainties in normalization, whose absolute scale may depend on the Higgs boson mass $m_H$ being probed in the search. The results and relevant uncertainties in ZZ estimation are mentioned in Sec. 5.1 .

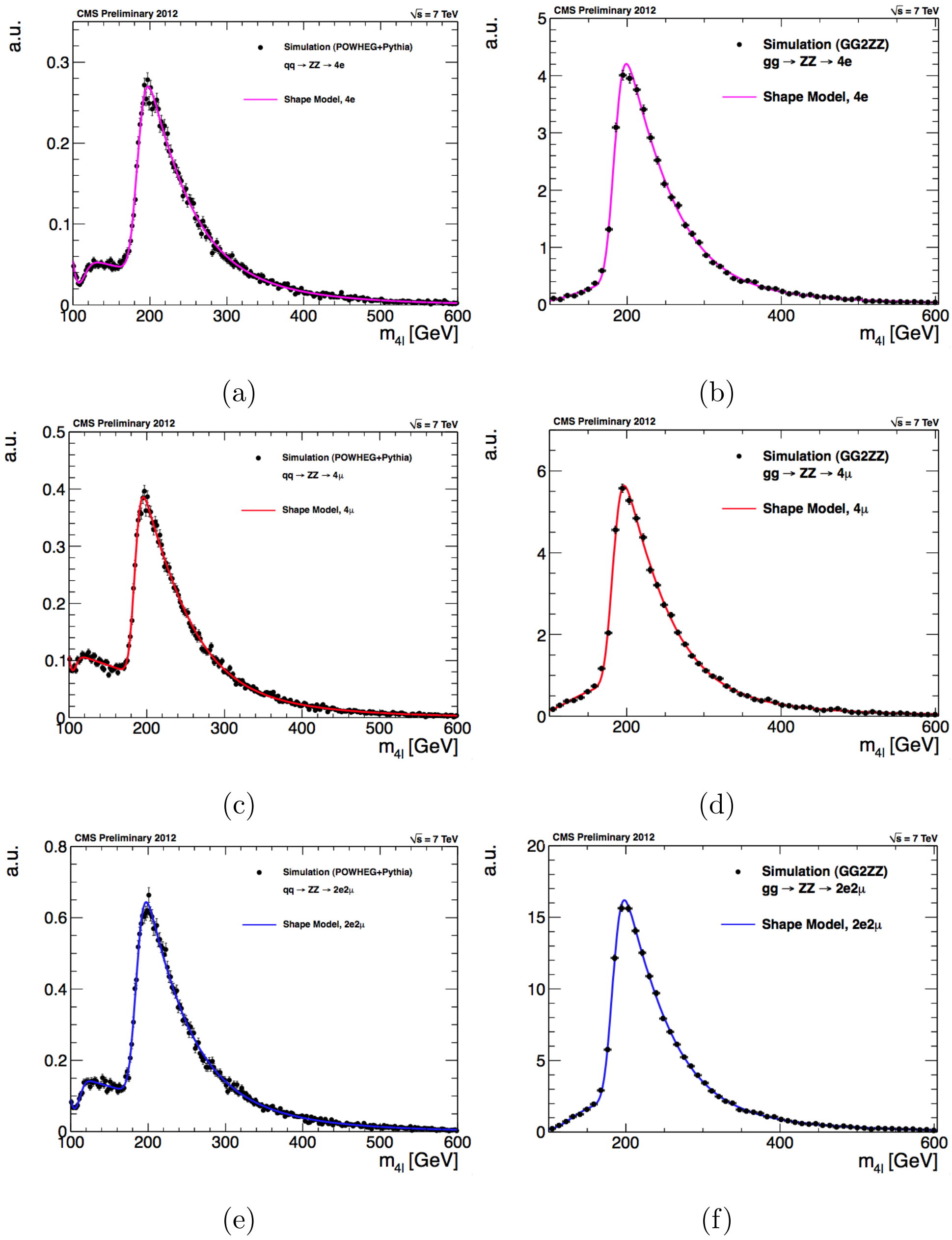


Figure 4.4: Probability density functions describing the NLO ZZ (left) and gg → ZZ (right) background shape for 4e (top), $4\mu$ (middle), and $2e2\mu$ (bottom) final states. The distributions correspond to $\sqrt{s} = 7$ TeV.

### 4.3.2 Reducible & Instrumental Background Estimation

The production mechanism of these backgrounds have been discussed in Sec. 1.4. The inclusive method here presented allows for an inclusive measurement of all the main instrumental and reducible backgrounds, that remain after the first Z boson reconstruction, at the same time. The reducible backgrounds for the $H \to ZZ \to 4\ell$ analysis are processes which contain one or more non-prompt leptons in the four-lepton final state. The main sources of non-prompt leptons are non-isolated electrons and muons coming from decays of heavy-flavour mesons, mis-reconstructed jets (usually originating from light-flavour quarks) and electrons from $\gamma$ conversions. In succeeding sections, their contribution will be measured via *fake rate* method by considering *fake leptons*. The 'fake lepton' represents any jet mis-reconstructed as a lepton and any lepton originating from a heavy meson decay. In a similar way, any electron originating from a photon conversion will be considered as 'fake electron'.

In particular, the rate of these background processes is estimated by measuring the probability for fake electrons $f_e$ and fake muons $f_\mu$ which do pass predefined loose selection criteria to also pass the final selection criteria. These probabilities are applied in dedicated control samples in order to extract the background yield expected in the signal region and referred as 'fake ratios'. The loose lepton selection criteria are defined in Tab. 4.2 & 4.3 and obtained from the final lepton selection criteria by relaxing the identification and isolation criteria.

Table 4.2: Definition of loose selection criteria for muon-like objects used for the measurement of muon fake ratio.

| Parameter | Selection |
|---|---|
| Type | Global OR (Tracker & arbitrated) |
| Ghost muon cleaning | Yes |
| $\|SIP_{3D}\|$ | <100 |
| $\|d_Z\|$ | $< 1.0$ |
| $\|d_0\|$ | $< 0.5$ |
| $p_T$ | $\geq 5$ GeV/c |
| $\|\eta\|$ | $\leq 2.4$ |

Table 4.3: Definition of loose selection criteria for electron-like objects used for the measurement of electron fake ratio.

| Parameter | Selection |
|---|---|
| Type | GSF Electrons |
| $e/\mu$ cross object cleaning cone $\Delta R$ | 0.05 |
| Missed inner pixel hits | $< 2$ |
| $\|SIP_{3D}\|$ | <100 |
| $\|d_Z\|$ | $< 1.0$ |
| $\|d_0\|$ | $< 0.5$ |
| $p_T$ | $\geq 7$ GeV/c |
| $\|\eta\|$ | $\leq 2.5$ |

#### 4.3.2.1 Fake Rate Method

In order to measure the lepton fake ratios $f_e$, $f_\mu$ another phase space have been defined as $Z(\ell\ell) + \ell$ region, whereas samples of $Z(\ell\ell) + e$ and $Z(\ell\ell) + \mu$ events are expected to be completely dominated by final states which include $Z$ boson and fake leptons. This phase space has been built in accord with below mentioned selection:

- One Z boson is reconstructed from two opposite charge same flavor leptons as given in Sec. 4.1.2.
- FSR recovery included in Z reconstruction, wherever needed.
- The invariant mass of reconstructed Z boson ($m_Z$) should be close to nominal Z mass and it should follow: 40 GeV/c$^2$ $< m_Z <$ 120 GeV/c$^2$.
- The two leptons from Z should have $p_T > 20/10$ GeV/c.
- Exactly one additional reconstructed lepton which satisfies loose selection criteria as defined in Tab. 4.2 and 4.3 in accord with its leptonic flavor.
- The missing transverse energy $E_{\mathrm{T}}^{\mathrm{miss}} <$ 25 GeV/c.

The events are required to have a low missing transverse energy in order to suppress the contamination from $WZ$ and $t\bar{t}$ processes. In case of this selection, it is expected to measure the fake ratios in a sample with a composition of background processes that is similar to the composition of backgrounds present in the signal region. Since the third lepton is expected to dominantly be a fake lepton it is used as a probe lepton to measure the fake ratio and known as *fakeable object*. For calculating fake rate probability the *fakeable object* should satisfy following cuts:

- identification and isolation requirements in accord with its leptonic nature.
- $\Delta R > 0.05$ from all reconstructed muons.
- invariant mass of $3^{rd}$ lepton with opposite charged lepton from Z should be $>$ 4 GeV/c$^2$.

Then single-lepton fake rate is defined as the ratio of the number of fakeable object passing these cuts to the total number of fakeable objects. This ratio is computed as a function of the lepton $p_{\mathrm{T}}$ in Barrel and Endcap regions, in accord with their $\eta$ distribution. The fake ratios have been calculated for individual data taking periods (assigned as `A` and `B` for 2011 and `A`, `B` and `C` for 2012).

The studies have been performed over electron and muons separately (in case of Endcap and Barrel regions) to comprehend the effect of increasing luminosity over fake rate measurements. It can be appreciated in Fig. 4.5c, 4.5d, 4.5e and 4.5f that the fake ratios are not showing significant difference between 2012(`A+B`) and 2012 `C` data taking periods and are stable for electrons and muons. The final estimation of reducible background in the 8 TeV analysis is therefore performed using fake ratios measured on the full 2012(`A+B+C`) period.

It can be observed from Fig. 4.5 and 4.6 that the fake ratios have shown dependance on the lepton $\mathrm{p_T}$ - in particular, the fake ratios increase in the region of high $p_T$. This effect is caused by the fact that the criteria used to suppress the WZ and $t\bar{t}$ processes is not sufficient in this region of $p_T$. It has been taken into account as one of the source of systematic uncertainty.

The fake ratios are observed higher in Endcap region as compared to Barrel region because the probability for leptons to be misidentified by jets increase with increase in $|\eta|$ values. This behavior is not well satisfied in some $\mathrm{p_T}$ bins because of less statistics in those particular bins, which leads to fluctuations in fake rate values. The corresponding values of error bars associated to fake rate values increases in higher $p_T$ bins. This effect is more conspicuous in case of muons as compared to electrons because the probability of muons to be misidentified by jets is lower as compared to the probability of electrons to be misidentified by jets. It results as less statistics in case of muons and higher error bars in corresponding $p_T$ bins.

The final numerical values of fake ratios both for electrons and muons in different $\mathrm{p_T}$ ranges have been shown over 2011 (`A+B`) and 2012 (`A+B+C`) data in Tab. 4.4, 4.5, 4.6, 4.7. These values are applied over $3^{rd}$ and $4^{th}$ leptons in dedicated control regions as studied in Sec. 4.3.2.2.

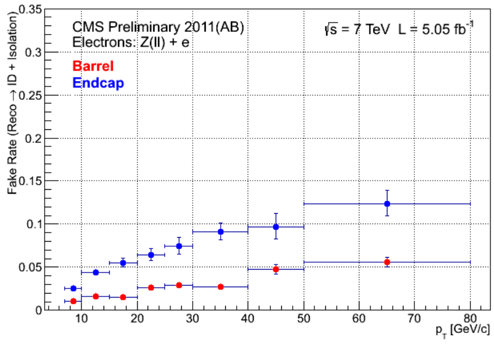


(a)

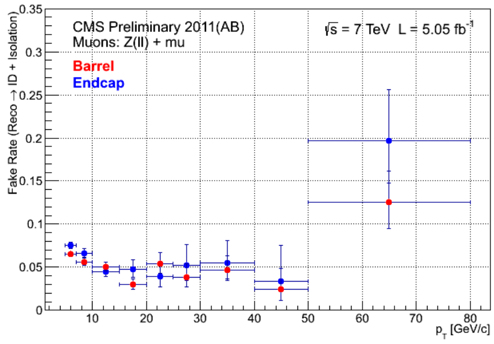


(b)

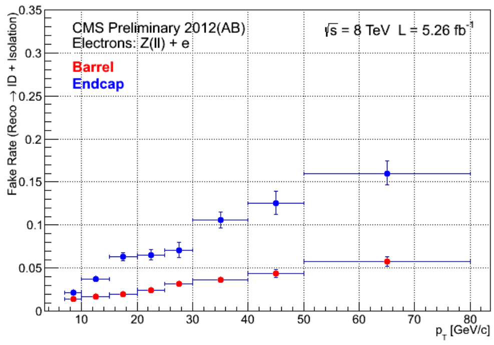


(c)

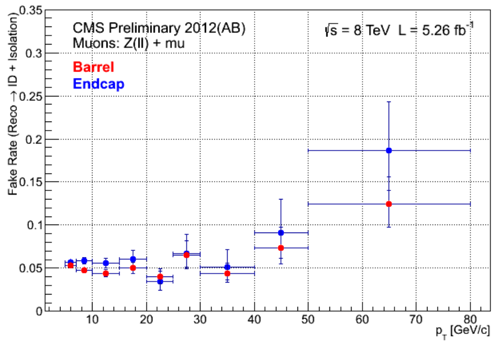


(d)

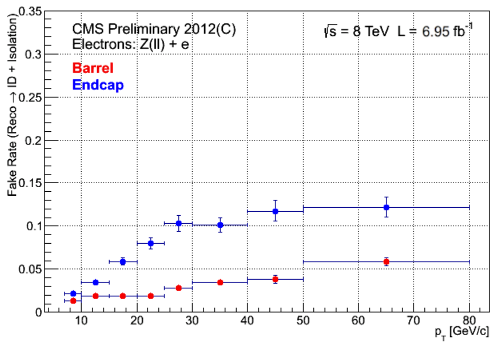


(e)

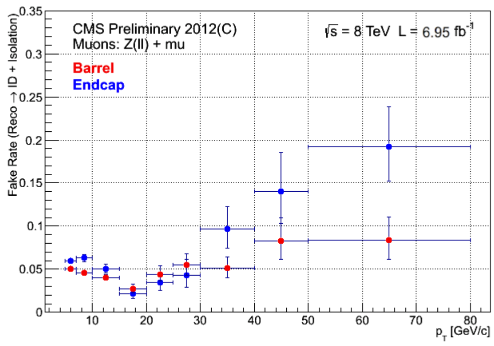


(f)

Figure 4.5: Fake rate measured for a probe lepton which satisfy loose selection, in the $Z(\ell\ell) + e$ (left) and $Z(\ell\ell) + \mu$ (right) samples as defined in the text. The fake rates correspond to data collected in 2011(`A+B`) (a) and (b), 2012 (`A+B`) (c) and (d), 2012 (`C`) (e) and (f).

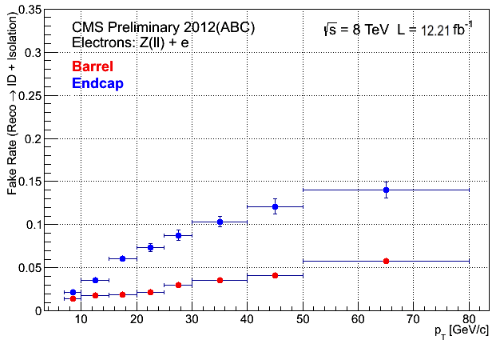


(a)

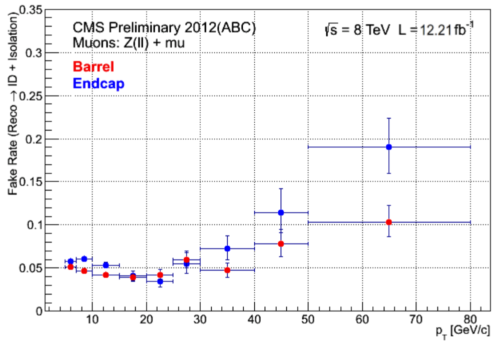


(b)

Figure 4.6: Fake rate measured for a probe lepton which satisfy loose selection, in the $Z(\ell\ell) + e$ (left) and $Z(\ell\ell) + \mu$ (right) samples as defined in the text. The fake rates correspond to data collected in 2012 (`A+B+C`) data taking periods.

Table 4.4: Muon Fake ratio's over 2011(`A+B`) data

(a) Z($\ell\ell$)+$\mu$ (Barrel)

| $p_T$ range | Fake ratio |
|---|---|
| $p_T$ [5-7] | 0.065 |
| $p_T$ [7-10] | 0.056 |
| $p_T$ [10-15] | 0.050 |
| $p_T$ [15-20] | 0.029 |
| $p_T$ [20-25] | 0.054 |
| $p_T$ [25-30] | 0.038 |
| $p_T$ [30-40] | 0.047 |
| $p_T$ [40-50] | 0.025 |
| $p_T$ [50-80] | 0.125 |

(b) Z($\ell\ell$)+$\mu$ (Endcap)

| $p_T$ range | Fake ratio |
|---|---|
| $p_T$ [5-7] | 0.075 |
| $p_T$ [7-10] | 0.066 |
| $p_T$ [10-15] | 0.045 |
| $p_T$ [15-20] | 0.047 |
| $p_T$ [20-25] | 0.039 |
| $p_T$ [25-30] | 0.051 |
| $p_T$ [30-40] | 0.055 |
| $p_T$ [40-50] | 0.033 |
| $p_T$ [50-80] | 0.197 |

Table 4.5: Electron Fake ratio's over 2011(A+B) data

(a) Z($\ell\ell$)+e (Barrel)

| $p_T$ range | Fake ratio |
|---|---|
| $p_T$ [7-10] | 0.010 |
| $p_T$ [10-15] | 0.015 |
| $p_T$ [15-20] | 0.015 |
| $p_T$ [20-35] | 0.026 |
| $p_T$ [25-30] | 0.029 |
| $p_T$ [30-40] | 0.027 |
| $p_T$ [40-50] | 0.047 |
| $p_T$ [50-80] | 0.055 |

(b) Z($\ell\ell$)+e (Endcap)

| $p_T$ range | Fake ratio |
|---|---|
| $p_T$ [7-10] | 0.025 |
| $p_T$ [10-15] | 0.044 |
| $p_T$ [15-20] | 0.055 |
| $p_T$ [20-25] | 0.064 |
| $p_T$ [25-30] | 0.074 |
| $p_T$ [30-40] | 0.091 |
| $p_T$ [40-50] | 0.096 |
| $p_T$ [50-80] | 0.123 |

Table 4.6: Muon Fake ratio's over 2012(A+B+C) data

(a) Z($\ell\ell$)+$\mu$ (Barrel)

| $p_T$ range | Fake ratio |
|---|---|
| $p_T$ [5-7] | 0.052 |
| $p_T$ [7-10] | 0.047 |
| $p_T$ [10-15] | 0.042 |
| $p_T$ [15-20] | 0.039 |
| $p_T$ [20-25] | 0.042 |
| $p_T$ [25-30] | 0.059 |
| $p_T$ [30-40] | 0.047 |
| $p_T$ [40-50] | 0.077 |
| $p_T$ [50-80] | 0.1033 |

(b) Z($\ell\ell$)+$\mu$ (Endcap)

| $p_T$ range | Fake ratio |
|---|---|
| $p_T$ [5-7] | 0.058 |
| $p_T$ [7-10] | 0.060 |
| $p_T$ [10-15] | 0.053 |
| $p_T$ [15-20] | 0.040 |
| $p_T$ [20-25] | 0.034 |
| $p_T$ [25-30] | 0.054 |
| $p_T$ [30-40] | 0.072 |
| $p_T$ [40-50] | 0.114 |
| $p_T$ [50-80] | 0.189 |

Table 4.7: Electron Fake ratio's over 2012(A+B+C) data

(a) Z($\ell\ell$)+e (Barrel)

| $p_T$ range | Fake ratio |
|---|---|
| $p_T$ [7-10] | 0.0138 |
| $p_T$ [10-15] | 0.017 |
| $p_T$ [15-20] | 0.019 |
| $p_T$ [20-25] | 0.021 |
| $p_T$ [25-30] | 0.029 |
| $p_T$ [30-40] | 0.035 |
| $p_T$ [40-50] | 0.040 |
| $p_T$ [50-80] | 0.058 |

(b) Z($\ell\ell$)+e (Endcap)

| $p_T$ range | Fake ratio |
|---|---|
| $p_T$ [7-10] | 0.021 |
| $p_T$ [10-15] | 0.035 |
| $p_T$ [15-20] | 0.060 |
| $p_T$ [20-35] | 0.073 |
| $p_T$ [25-30] | 0.087 |
| $p_T$ [30-40] | 0.103 |
| $p_T$ [40-50] | 0.120 |
| $p_T$ [50-80] | 0.140 |

#### 4.3.2.2 Control Regions

The current background estimation method performs an inclusive treatment of all the main reducible backgrounds at the same time. A control region is defined as a subset of the events that satisfy the first step of the event selection i.e. first Z reconstruction. This control region have also to satisfy below mentioned conditions to populate the background-like events:

- to avoid the signal contamination in this control region, it requires an additional pair of *loose leptons* of same sign and same flavor (SS-SF: $e^{\pm}e^{\pm}, \mu^{\pm}\mu^{\pm}$).
- SS-SF leptons are requested to pass $\mathrm{SIP_{3D}}$ cut but lepton identification or isolation requirements are not imposed so that we can select more background-like events.
- reconstructed invariant mass of the SS-SF leptons & $\mathrm{m_{Z1}}$ have to satisfy the baseline or the high-mass selections as given in Sec. 4.2 and the reconstructed four-lepton invariant mass is required to satisfy $m_{4\ell} > 100\ \ \mathrm{GeV/c^2}$.

From this set of events the inclusive number of reducible backgrounds in the signal region is obtained by taking into account the probability for the two additional leptons to pass the isolation and identification analysis cuts, which is obtained from the fake rate measurement.

#### 4.3.2.3 Extraction to the Signal Region

By starting from the control sample described above, the final reducible background contribution expected in the signal region is calculated by the following expression:

$$N^{\mathrm{Z+X}}_{\mathrm{expect}} = \quad N^{\mathrm{DATA}} \times (\tfrac{\mathrm{OS}}{\mathrm{SS}})^{\mathrm{MC}} \times \quad \epsilon_1(p_T, \eta) \times \epsilon_2(p_T, \eta) \tag{4.9}$$

where:

- $N^{\mathrm{DATA}}$ is the number of events in the control region,
- X represents pair of fakeable leptons,
- $(\frac{\mathrm{OS}}{\mathrm{SS}})^{\mathrm{MC}}$ is a correction factor between opposite sign and same sign control samples. The MC correction factor is applied to consider the effect of signal-like fakeable lepton pairs, which are having opposite sign and same flavor (OS-SF) but not considered in background control region to avoid signal contribution.
- $\epsilon_i(p_T, \eta)$ is the fake rate probability for each of additional pair of *loose leptons* ($i = 1, 2$) in function of $p_T$ and $\eta$.

#### 4.3.2.4 MC Correction Factors

It is calculated individually for 7 and 8 TeV by defining one more control region, which is dedicated to select signal-like fakeable lepton pairs. The second control region is defined in same manner as explained in Sec. 4.3.2.2 but it will consider Z + OS-SF leptons instead of Z + SS-SF.

Fig. 4.7, 4.8, 4.9 and 4.10 are showing the comparison between data and MC for samples selected with Z + SS-SF and Z + OS-SF in accord with all final states at 7 and 8 TeV of data. The four lepton mass spectrum having electrons as final states have more number of events because electrons have more possibility to be misidentified by jets as compared to muons and a reasonable agreement is achieved between data and MC. Similarly in case of Fig. 4.8 and 4.10 $2\mu 2e$ final state have more events than $2e2\mu$.

The differences in rates has been taken from MC by subtracting the ZZ contribution because ZZ continuum will results into augmentation of signal like events (OS-SF lepton pairs). The total number of events in Z + OS-SF and Z + SS-SF samples are divided to compute the correction factor in eq. 4.9 for the final estimation of backgrounds via data-driven method. The calculated values of MC correction factors at 7 and 8 TeV are reported in Tab. 4.8.

Table 4.8: $(\frac{\text{OS}}{\text{SS}})^{\text{MC}}$ correction factor.

| **sample** | **7 TeV** | **8 TeV** |
|---|---|---|
| 4e | 0.99 | 1.15 |
| $4\mu$ | 1.16 | 1.18 |
| $2\mu 2e$ | 1.03 | 1.12 |
| $2e2\mu$ | 1.28 | 1.24 |

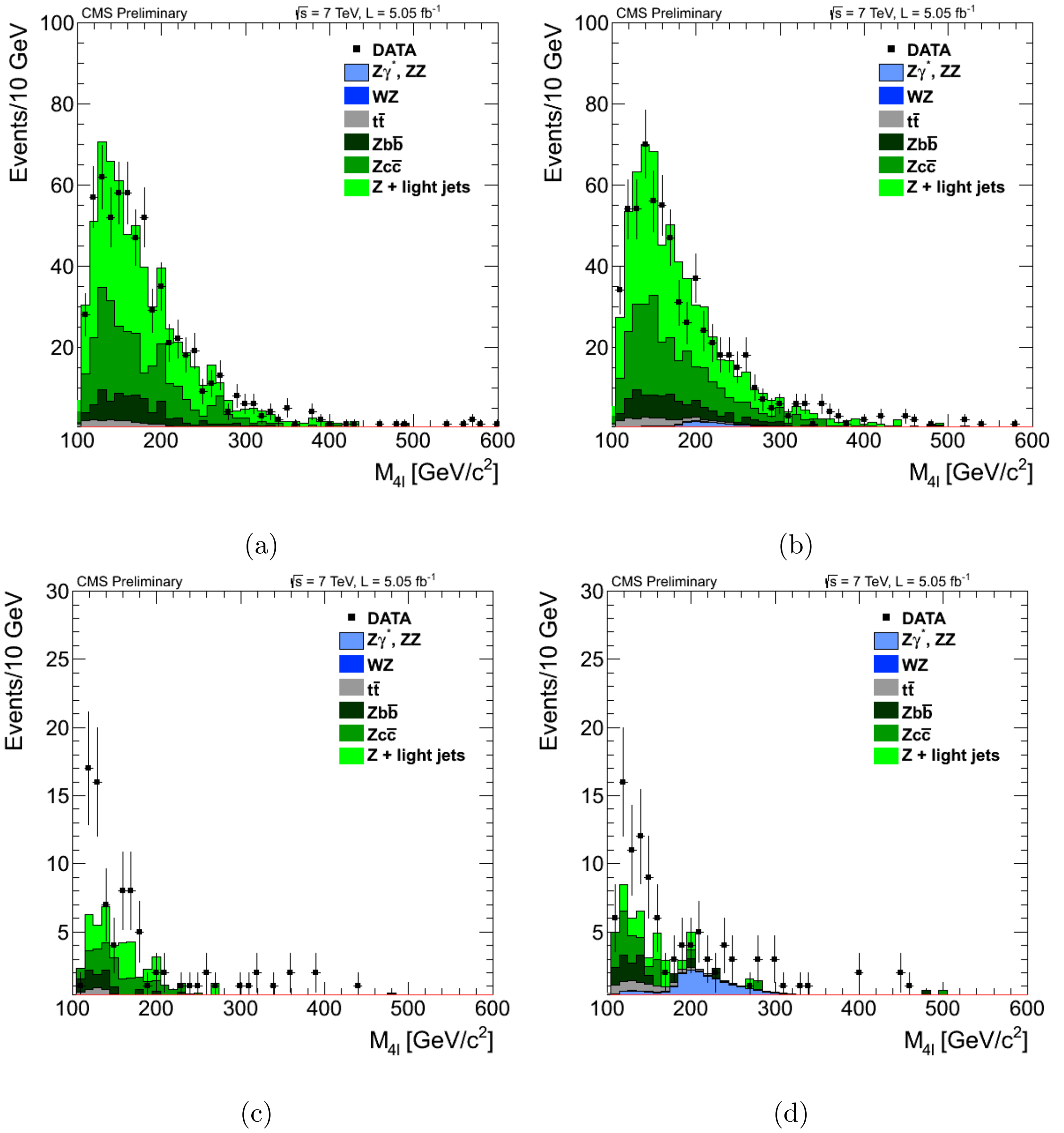


Figure 4.7: DATA-MC comparison of the SS-SF (on the left) and OS-SF (on the right) samples in the Z+X background control samples. (a) and (b) represents $4e$, (c) and (d) shows $4\mu$ final states.The distributions correspond to data collected in 2011 ($\mathcal{L} = 5$ fb$^{-1}$ @ 7 TeV).

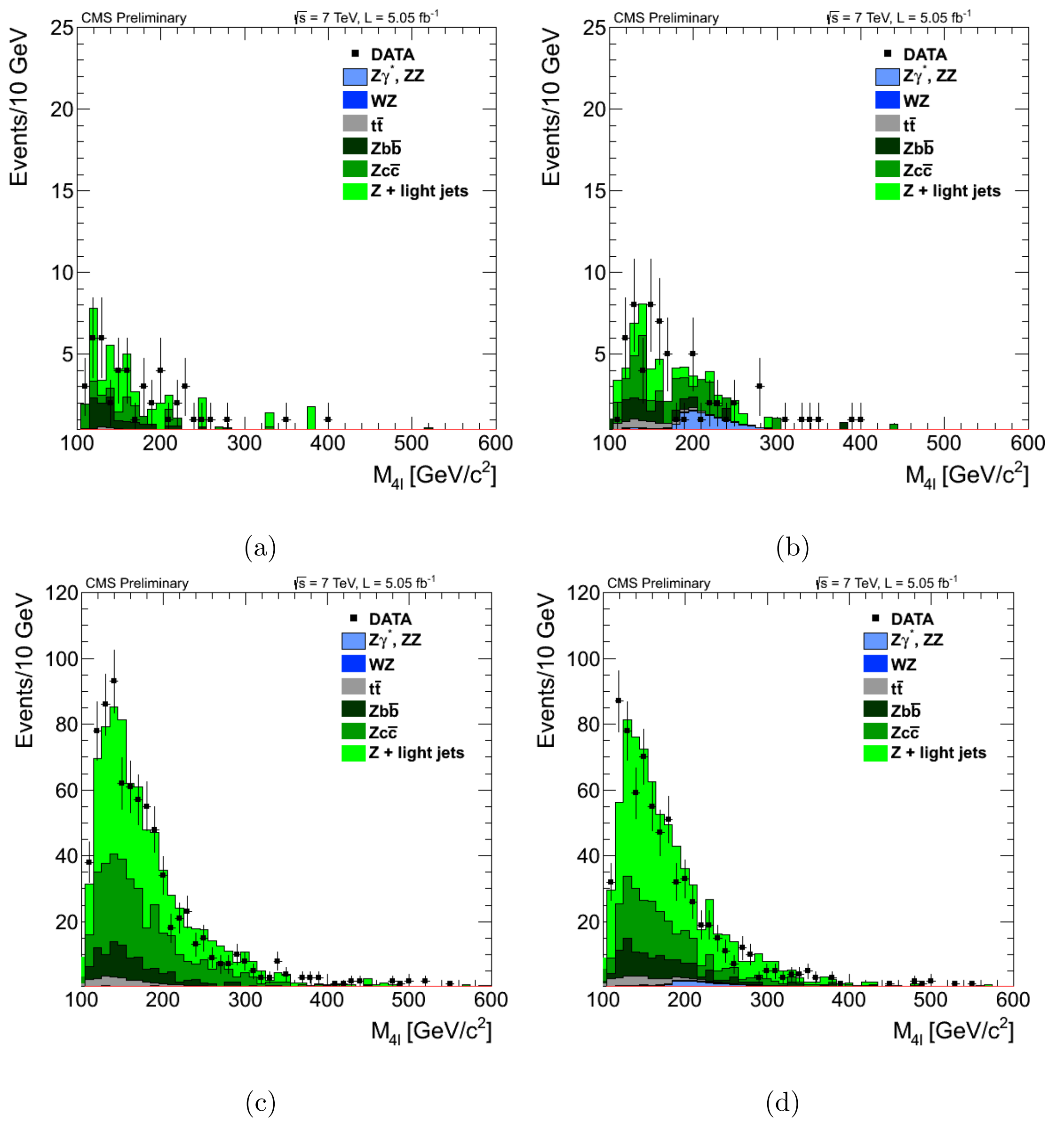


Figure 4.8: DATA-MC comparison of the SS-SF (on the left) and OS-SF (on the right) samples in the Z+X background control samples. (a) and (b) represents 2e2$\mu$, (c) and (d) shows 2$\mu$2$e$ final states. The distributions correspond to data collected in 2011 ($\mathcal{L} = 5$ fb$^{-1}$ @ 7 TeV).

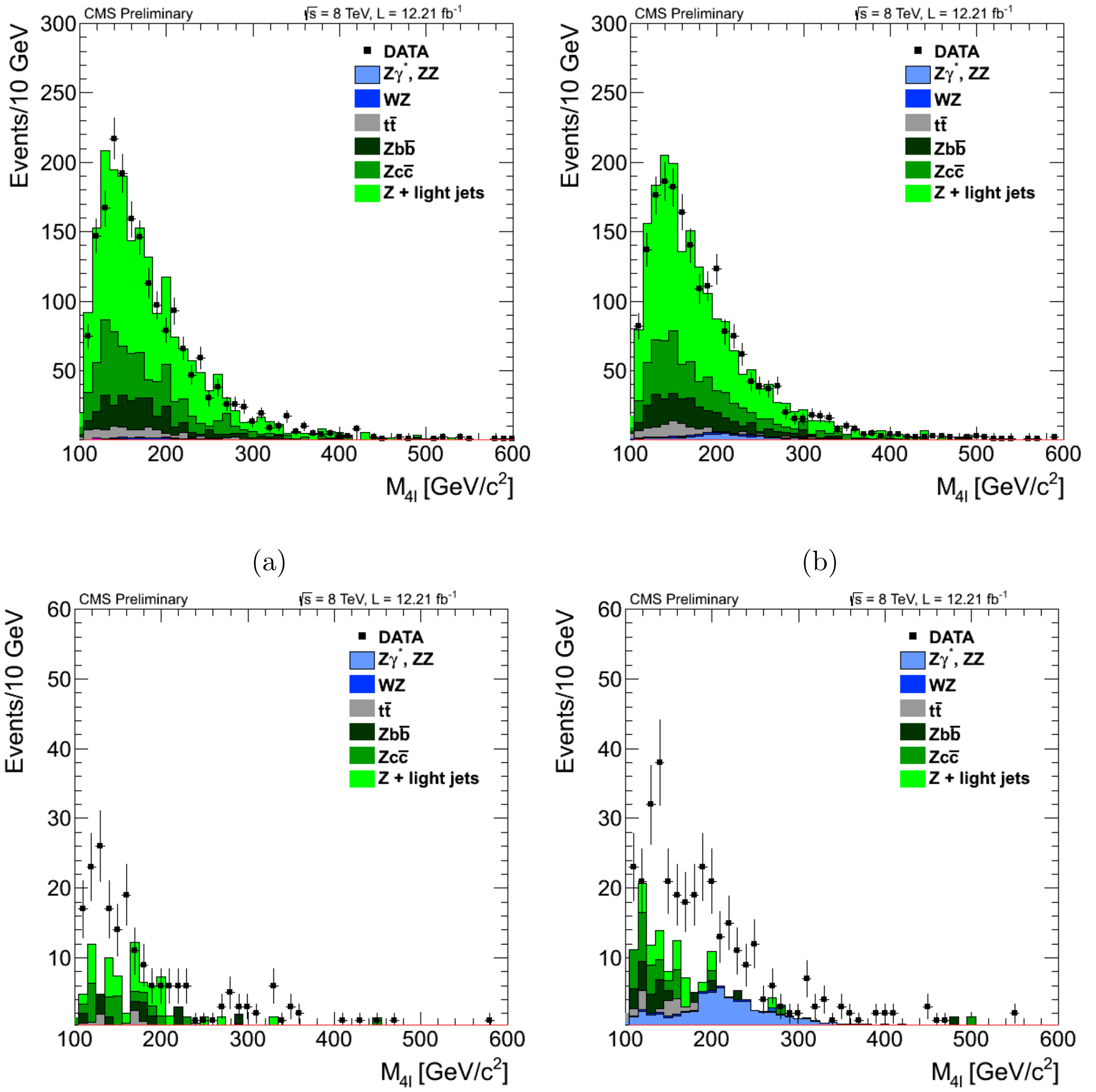


(a) (b)

(c) (d)

Figure 4.9: DATA-MC comparison of the SS-SF (on the left) and OS-SF (on the right) samples in the Z+X background control samples. (a) and (b) represents $4e$, (c) and (d) shows $4\mu$ final states. The distributions correspond to data collected in 2012 ($\mathcal{L} = 12.21$ fb$^{-1}$ @ 8 TeV).

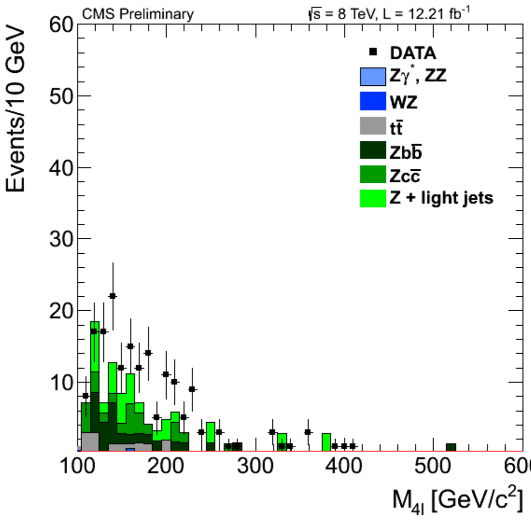


(a)

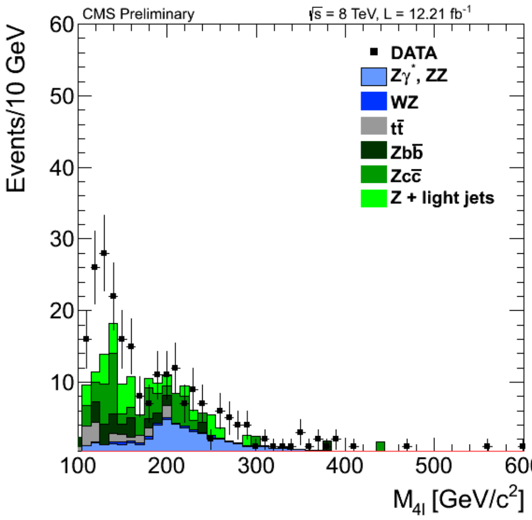


(b)

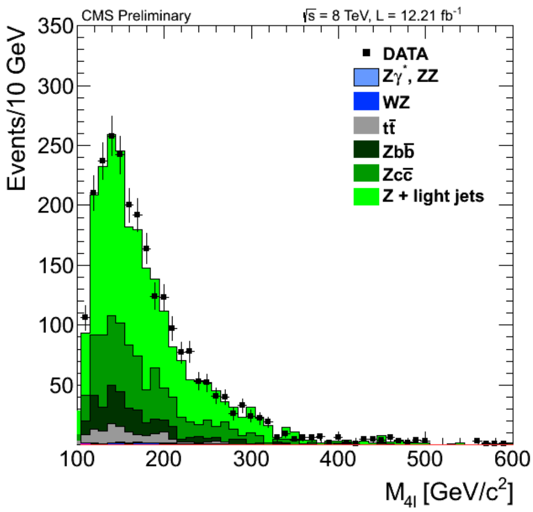


(c)

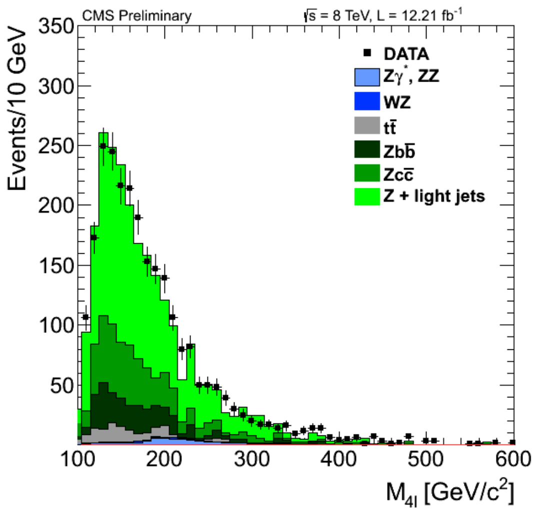


(d)

Figure 4.10: DATA-MC comparison of the SS-SF (on the left) and OS-SF (on the right) samples in the Z+X background control samples. (a) and (b) represents $2e2\mu$, (c) and (d) shows $2\mu 2e$ final states. The distributions correspond to data collected in 2012 ($\mathcal{L} = 12.21$ fb$^{-1}$ @ 8 TeV).

## 4.4 Alternate Event Selection Methodology

The current section is focussed to examine the possibility for increasing the Higgs signal selection efficiency. The studies are performed in accord with Ref. [69], which reconstructs $Z_1$ from two OS-SF lepton pairs and '$m_{Z1}$' is required to be close to nominal Z mass. The invariant mass distribution of '$m_{Z1}$' for contributing background and Higgs signal process is presented in Fig. 4.11a, which shows a perfect Data-MC agreement. Later on, $Z_2$ is reconstructed from 2 other highest $p_T$ leptons in that event. The invariant mass distribution of '$m_{Z2}$' is displayed in Fig. 4.11b and it shows a lack of events at Z mass peak. This behavior is confirmed by Data and MC samples.

The reason is that if we found any Z boson having '$m_Z$' close to nominal Z mass (or an on mass shell Z), it is assigned as $Z_1$. It decreases the possibility to get second on mass shell Z also as $Z_2$. So selection criterion of $Z_1$ and $Z_2$ leads to a deficiency of events in invariant mass spectrum of '$m_{Z2}$' exactly at Z mass peak. It is shown in Fig. 4.11b that the effect becomes visible for Higgs mass $\approx$ ZZ di-boson mass but stays permanently for higher masses as well. Conceptually this effect presents at lower Higgs mass too, where two Z bosons can not be on mass shell.

This observation have shown a logical space for refinement and impulsed to improve the event selection methodology by changing the selection criterion of $Z_1$ and $Z_2$.

The alternative approach that I proposed is devoted to study the effect of dealing with $4\ell$ candidates built with any possible combination of good leptons, so not using the above mentioned way of selecting $Z_1$ and $Z_2$. If we bypass the '$m_{Z1}$ close to nominal Z mass criterion', it can results to increase the Higgs signal selection efficiency, which will be followed by partial increase in relative background contributions as well.

In particular for current section, analysis have been performed over proton-proton collision data recorded by the CMS detector at the LHC, corresponding to integrated luminosities of 4.71 fb$^{-1}$ @ $\sqrt{s} = 7$ TeV (2011). It starts from trigger selection (see Tab. 3.1), that requires

- pair of electrons with $E^e_{T,1} > 17$ GeV and $E^e_{T,2} > 8$ GeV, or
- pair of muons with $p^\mu_{T,1} > 17$ GeV/c and $p^\mu_{T,2} > 8$ GeV/c,

where $E_T$ is transverse energy. The trigger is found fully efficient for the $4e$, $4\mu$ and $2e2\mu$ channels within the acceptance of current analysis.

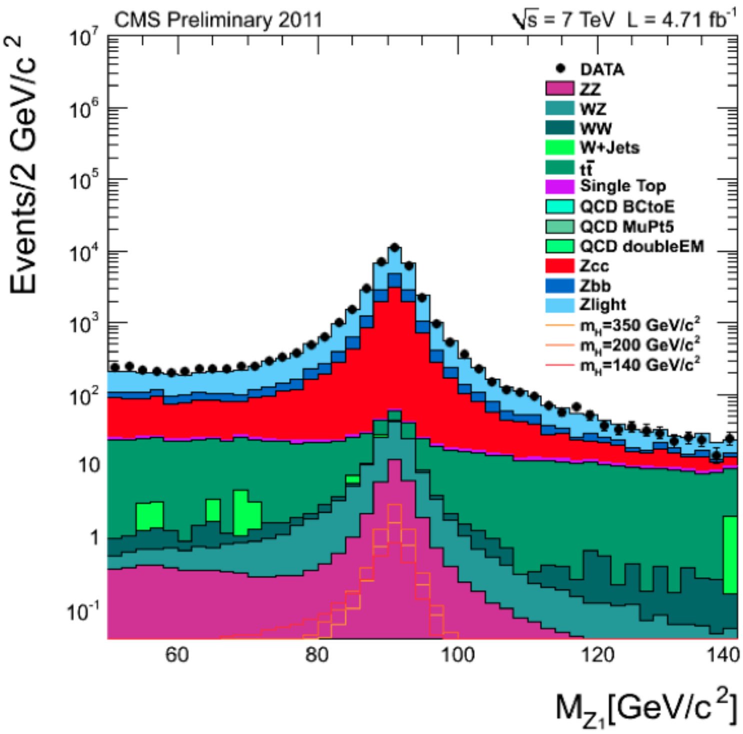


(a)

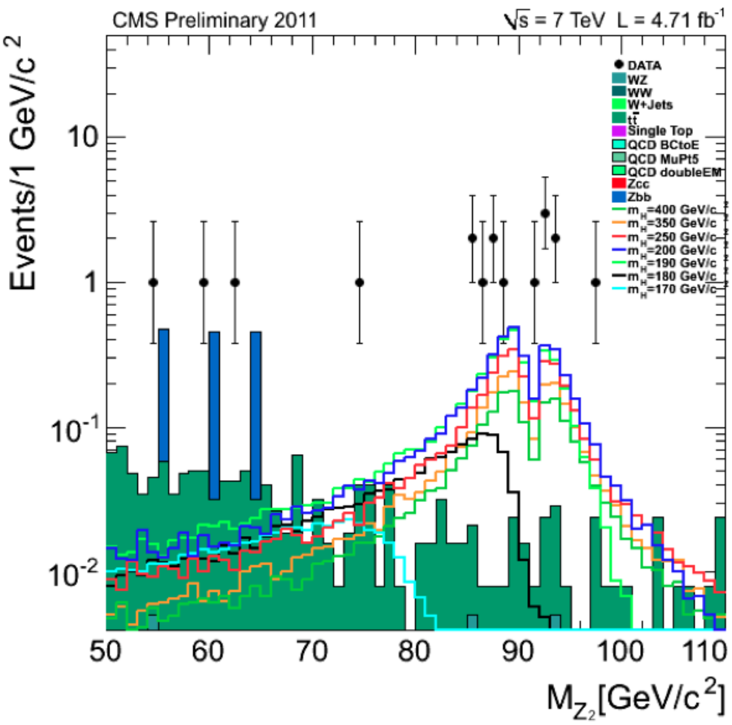


(b)

Figure 4.11: (a) Invariant mass distribution of reconstructed Z boson ($4\mu$) after *best* $Z_1$ selection (left) in accord with event selection methodology of Ref. [69], whereas (b) shows the invariant mass distribution of second reconstructed Z boson ($4\mu$) as *best* $Z_2$ after full event selection. Shaded histogram displays MC samples and solid points represent data corresponding to $\mathcal{L} = 4.71 fb^{-1}$ @ $\sqrt{s} = 7$ TeV.

### 4.4.1 Skimming

A preliminary selection of events, referred to as a *skim*, is designed to reduce the data set to a manageable size while preserving high signal selection efficiency. The skim is common to all $4\ell$ channels, requires the HLT selection described in the previous section, the requirement of at least one same flavor di-lepton candidate selected with the following criteria on the component leptons:

- leptons of opposite charge, reconstructed with either the electron basic track-supercluster objects, global muon objects, or tracker muon objects.
- electrons and muons should be within the geometrical acceptance of $|\eta^e| < 2.5$, $|\eta^\mu| < 2.4$ with $p_T^e > 7$ GeV/c, $p_T^\mu > 5$ GeV/c.
- invariant mass of at least one di-lepton pair (made from OS-SF leptons) should be greater than 40 GeV/c$^2$.

### 4.4.2 Event selection

The leptons should be loosely isolated lepton candidates. A lepton is defined as *loosely isolated* if the sum $\sum_i p^i_{T,\mathrm{track}}$ of the transverse momentum of the tracks divided by $p_T^\ell$ is less than 0.7. The tracks are lying in a cone of radius $\Delta R = \sqrt{\Delta\eta^2 + \Delta\phi^2} < 0.3$ around the lepton $\ell$ with axis along the lepton candidate direction, excluding a central inner 'veto' region of width $\Delta\eta < 0.015$ (electron) or $\Delta R < 0.015$ (muon), which contains the lepton candidate track footprint. The $\Delta\phi$ is the difference between azimuthal angles of two leptons (i.e. $\phi_1$ and $\phi_2$), which are lying outside inner veto of 0.015 and within $\Delta R < 0.3$. The lepton isolation efficiency for identified leptons within this very loose isolation is found to be greater than 99%. Once an event satisfies the above mentioned quality criterion, the 4 lepton signal selection strategy implemented as given below:

- Each $4\ell$ candidate in an event is treated individually by checking the quality parameters of its daughters.
- $4\ell$ daughters should have $p^l_{T1} > 20$, $p^l_{T2} >10$, $p^l_{T,3,4} > 7$ GeV/c (5 GeV/c) for electrons (muons).
- **Baseline**: The mass cuts over Z boson have been lowered to make the analysis strategy compatible to low mass Higgs searches. One Z should have m$_Z$ between 50 GeV/c$^2$ to 120 GeV/c$^2$ and m$_Z$ for second Z should be within 12 GeV/c$^2$ to 120 GeV/c$^2$.

- **Intermediate**: This region is compatible to Higgs searches in intermediate mass range, where invariant mass of one Z should lie between 60 GeV/c$^2$ to 120 GeV/c$^2$ and $m_Z$ for second Z should be within 20 GeV/c$^2$ to 120 GeV/c$^2$.
- **High mass**: This class is used for ZZ cross-section measurement as it's suitable for high mass Higgs searches, where possibility increases to get both on mass shell Z boson. The corresponding selection range over invariant mass of Z for both Z bosons is $60 < m_Z < 120$ GeV/c$^2$.
- significance of the impact parameter to the event vertex, $\mathrm{SIP_{3D}}$, is required to satisfy $\mathrm{SIP_{3D}} = \frac{|\mathrm{IP}|}{\sigma_{\mathrm{IP}}} < 4$ for each lepton.
- The combined relative isolation should be $< 0.35$ for each lepton.
- The invariant mass of four lepton candidate ($\mathrm{m}_{4\ell}$ ) should be greater than 100 GeV/c$^2$.
- In case of more than one 4 lepton candidates, select one having at least one Z particle whose mass is close to real Z mass.

### 4.4.3 Results

The expected improvement is shown in Fig. 4.12, which represents the invariant mass distributions of $\mathrm{m}_{Z1}$, $\mathrm{m}_{Z2}$, $\mathrm{m}_{4e}$ and $\mathrm{m}_{4\mu}$. It is observed that asymmetry over Z mass peak in case of $\mathrm{m}_{Z2}$ is resolved and invariant mass spectrum of Z boson is well reproduced by Data and MC for 4e and 4$\mu$ final states. All plots are obtained after applying full selection criterion described above. The large error bars associated to data points are caused by the less number of events surviving full selection.

The signal selection efficiency for each step of selection is shown in Fig. 4.13a and 4.13b for 4e and 4$\mu$ final states respectively. The X-axis represents Higgs signal selection efficiency and simulated Higgs masses ($\mathrm{m}_H$) are represented along Y-axis. The signal selection efficiency is calculated as follows:

$$\epsilon = \frac{A_{events}}{B_{events}} \tag{4.10}$$

where:

- $\epsilon$ is the Higgs signal selection efficiency.
- $A_{events}$ represents total number of events satisfying the $|\eta| < 2.5$ (2.4) for electrons (muons) and $p_T > 7$ GeV/c (5 GeV/c) for electrons (muons).
- $B_{events}$ is the total number of events surviving corresponding selection cut.

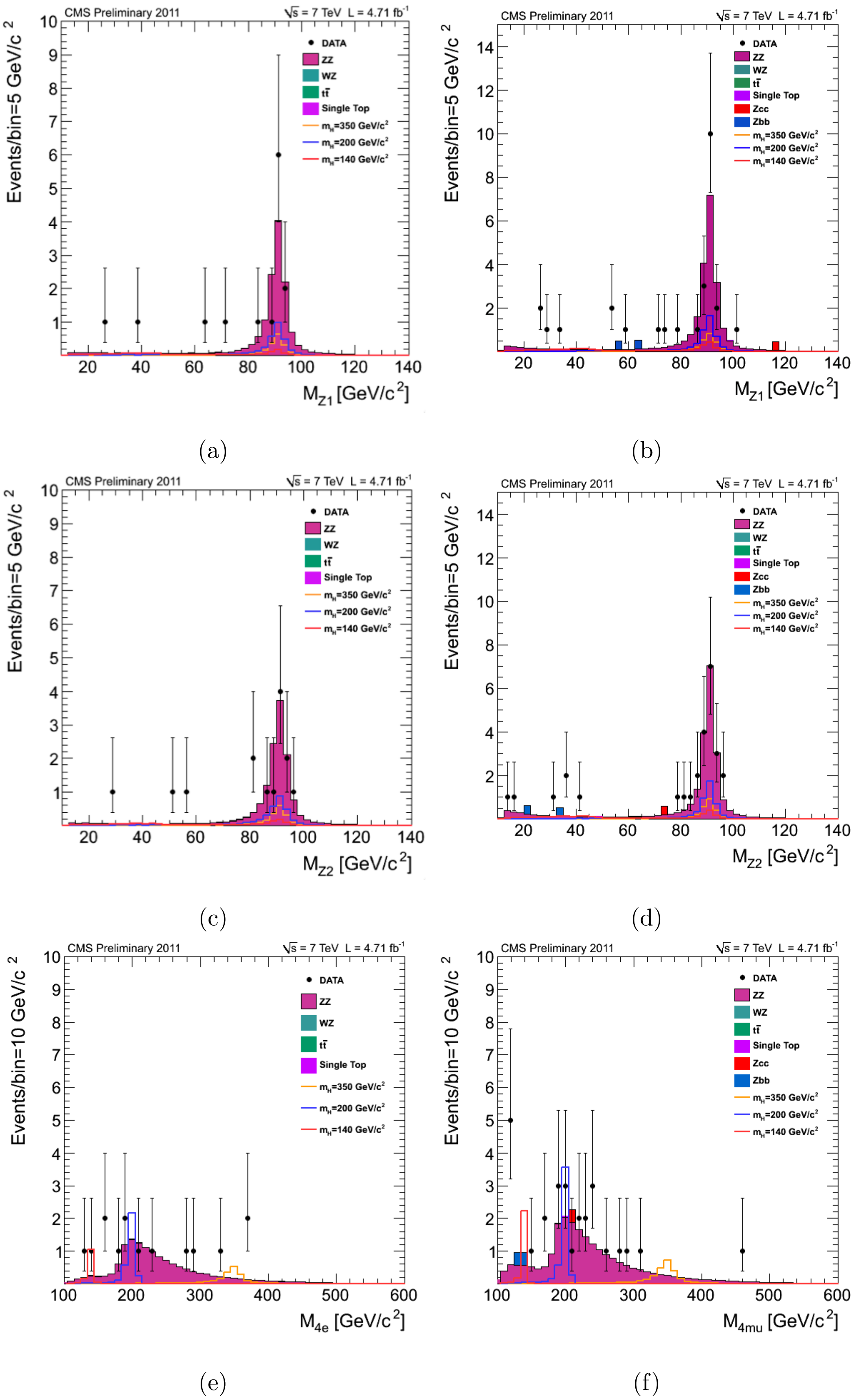


Figure 4.12: Distribution of reconstructed mass of Z1, Z2 and $4\ell$ in case of 4e (left) and $4\mu$ (right) final state. Shaded histogram displays MC samples and solid points represent data corresponding to $\mathcal{L} = 4.71 fb^{-1}$ @ $\sqrt{s} = 7$ TeV.

The overall small signal selection efficiency for lower Higgs masses can be understood from Fig. 3.6 and 3.8a, which shows that analysis cuts like $m_{4\ell} > 100$ GeV/c$^2$ and $p_T$ cut over leptons can decrease the number of signal events considerably along with background events after full selection.

Moreover, it is observed that selection efficiency for Higgs signal is increased by 4% (10%) in case of 4e (4mu) for Higgs mass 120 GeV/c$^2$ as compared to Ref. [69]. This increase in signal selection efficiency is followed by relative increase in background contribution as well. The cut wise status of event yield of contributing samples has been shown in Tab. 4.9 and 4.10 for 4e and 4mu final states.

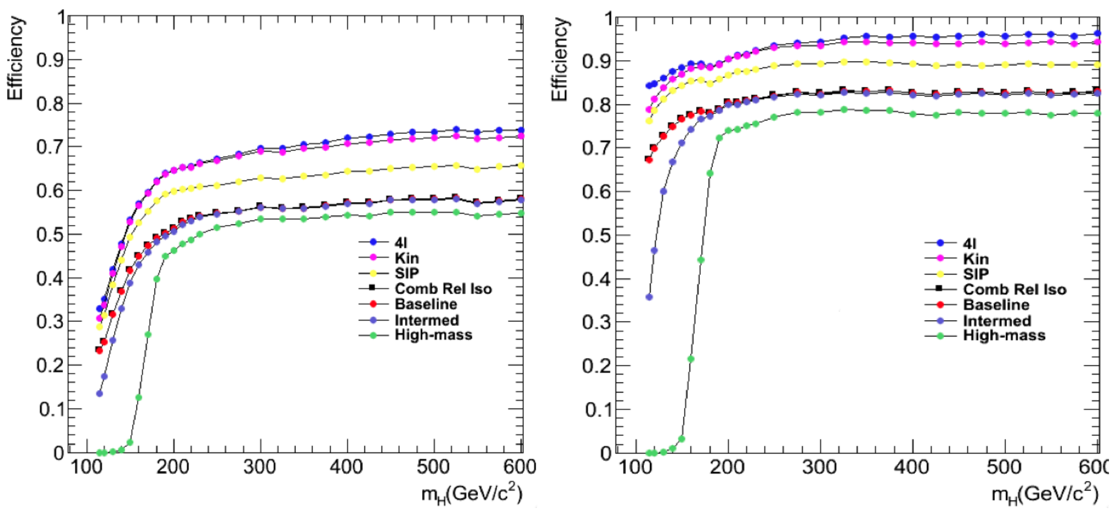


(a) (b)

Figure 4.13: Signal selection efficiencies for Higgs masses, 4e (a) and $4\mu$ (b). Shaded histogram displays MC samples and solid points represent data corresponding to $\mathcal{L} = 4.71 fb^{-1}$ @ $\sqrt{s} = 7$ TeV.

Table 4.9: The cut wise status of event yields of contributing samples in $4\mu$ final state

| Sample | Skimm | 4l | SIP | $R_{iso}$ | Baseline | Intermediate | High mass |
|---|---|---|---|---|---|---|---|
| QCD | 769631 | 0 | 0 | 0 | 0 | 0 | 0 |
| $t\bar{t}$ | 11013 | 11.16 | 1.46 | 0.04 | 0.04 | 0.03 | 0.008 |
| Z+ jets | 1.5e+06 | 0.4 | 0 | 0 | 0 | 0 | 0 |
| Zbb | 124526 | 25.4 | 5.2 | 0.8 | 0.8 | 0.4 | 0 |
| Zcc | 578439 | 0.8 | 0.4 | 0.4 | 0.4 | 0.4 | 0.4 |
| WZ | 642.04 | 0.16 | 0.08 | 0.025 | 0.025 | 0.023 | 0.005 |
| ZZ | 197.94 | 29.36 | 24.6 | 22.9 | 22.9 | 21.02 | 17.61 |
| H 200 | 32.63 | 5.34 | 5.12 | 4.74 | 4.74 | 4.72 | 4.37 |
| Total | 2975069 | 67.28 | 31.73 | 24.19 | 24.19 | 21.87 | 18.02 |
| **Data** | 3312214 | 168 | 36 | 27 | 27 | 24 | 15 |

Table 4.10: The cut wise status of event yields of contributing samples in 4e final state

| Sample | Skimm | 4l | SIP | $R_{iso}$ | Baseline | Intermediate | High mass |
|---|---|---|---|---|---|---|---|
| QCD | 48614 | 0 | 0 | 0 | 0 | 0 | 0 |
| $t\bar{t}$ | 6167 | 2.82 | 0.69 | 0.016 | 0.016 | 0.008 | 0.008 |
| Z+ jets | 1.3 e+06 | 2.38 | 0.8 | 0 | 0 | 0 | 0 |
| Zbb | 108234 | 3.17 | 0 | 0 | 0 | 0 | 0 |
| Zcc | 511890 | 2.38 | 0.4 | 0 | 0 | 0 | 0 |
| WZ | 578.6 | 0.28 | 0.18 | 0.069 | 0.069 | 0.061 | 0.02 |
| ZZ | 174.3 | 18.99 | 16.02 | 14.36 | 14.36 | 13.76 | 11.9 |
| H 200 | 28.8 | 4.0 | 3.7 | 3.2 | 3.2 | 3.14 | 2.87 |
| Total | 1.9e+06 | 30.04 | 18.08 | 14.44 | 14.44 | 13.83 | 11.93 |
| **Data** | 2146946 | 39 | 19 | 14 | 14 | 14 | 9 |

## 4.5 H→ ZZ* → 4ℓ analysis by Bayesian Approach

The search of the SM Higgs boson in the H→ $ZZ^*$ → $4\ell$ decay channel is also performed by using a multivariate technique [77] known as Bayesian neural networks (BNNs) [78]. Signal and background discriminants are derived and the results are compared to the baseline cut-based method. A detailed treatment of H→ $ZZ^*$ → $4\ell$ decay channel via BNN approach have been reported in Refs. [79], [80].

The analysis have been performed over proton-proton collision data recorded by the CMS detector at the LHC, corresponding to integrated luminosities of 4.71 $fb^{-1}$ @ $\sqrt{s} = 7$ TeV (2010 & 2011) and 5.26 $fb^{-1}$ @ $\sqrt{s} = 8$ TeV (2012).

A "multivariate discriminant" function $D(x)$ is used to classify objects characterized by a vector of properties $x$. In our case, we use $D(x)$ to classify events as signal $s(x)$ or background $b(x)$ with minimum classification error [2]. The consistently Bayesian method uses a binned likelihood constructed from a multivariate discriminant $D(x)$ and a $4\ell$ mass distribution created from a comprehensive set of simulated events for signal and background.

I have estimated the reducible background contribution in signal region by using methodology explained in previous sections. The estimated values of background are used for training of the BNN events to get input histogram for background samples, which are used to calculate the binned likelihood D($x$) *vs.* $m_{4\ell}$. The $4\mu$, 4e and $2e2\mu$ decay channels were trained separately.

[2]In principle, the discriminant should be chosen to minimize directly the quantity of interest. Experience suggests, however, that a discriminant that minimizes classification error performs well in practice.

# Chapter 5

# Results and Statistical Interpretation

The first half of current chapter will reveal the background estimation results in respective control regions and relative uncertainties over their measurements will be briefly discussed. While the second half will cover results obtained by using estimated values of corresponding backgrounds in signal region *i.e.* about mass measurements and statistical results.

## 5.1 ZZ Continuum

The total number of events in Higgs signal region and relative uncertainties from $ZZ^* \to 4\ell$ have been estimated from Monte Carlo simulation. The corresponding event yield and uncertainties are described in following Tab. 5.1.

Table 5.1: Number of ZZ background events expected and relative uncertainties in the signal region estimated from Monte Carlo simulation, for 5.1 fb$^{-1}$ at 7 TeV and 12.21 fb$^{-1}$ at 8 TeV data. Uncertainty on the yields due to QCD scale and the choice of parton distribution functions is also reported. Only the Monte Carlo statistical uncertainty is shown.

(a) **7 TeV**

| | | |
|---|---|---|
| $q\bar{q}$ | $N^{\mathrm{ZZ}\to 4e}$ | $13.3 \pm 0.06$ |
| | $N^{\mathrm{ZZ}\to 4\mu}$ | $20.77 \pm 0.08$ |
| | $N^{\mathrm{ZZ}\to 2e2\mu}$ | $31.8 \pm 0.3$ |
| $gg$ | $N^{\mathrm{ZZ}\to 4e}$ | $0.91 \pm 0.01$ |
| | $N^{\mathrm{ZZ}\to 4\mu}$ | $1.28 \pm 0.01$ |
| | $N^{\mathrm{ZZ}\to 2e2\mu}$ | $2.15 \pm 0.08$ |

(b) **8 TeV**

| | | |
|---|---|---|
| $q\bar{q}$ | $N^{\mathrm{ZZ}\to 4e}$ | $36.9 \pm 0.2$ |
| | $N^{\mathrm{ZZ}\to 4\mu}$ | $56.2 \pm 0.2$ |
| | $N^{\mathrm{ZZ}\to 2e2\mu}$ | $89.8 \pm 0.6$ |
| $gg$ | $N^{\mathrm{ZZ}\to 4e}$ | $2.22 \pm 0.01$ |
| | $N^{\mathrm{ZZ}\to 4\mu}$ | $3.06 \pm 0.02$ |
| | $N^{\mathrm{ZZ}\to 2e2\mu}$ | $6.51 \pm 0.20$ |

### 5.1.1 Uncertainties in ZZ measurement

The theoretical uncertainties have been calculated over event yield as a function of $m_{4\ell}$ in Ref. [62]. These are briefly discussed here for completeness. PDF+$\alpha_s$ and QCD scale uncertainties for $pp \to ZZ \to 4\ell$ at NLO and $gg \to ZZ \to 4\ell$ are evaluated using MCFM [75]. The $2e2\mu$ final state has been used with following fiducial cuts for leptons:

- electrons should have $p_T > 7$ GeV/c and $|\eta| < 2.5$.
- muon's $p_T$ should be greater than 5 GeV/c and $|\eta| < 2.4$.
- invariant mass of di-electron and di-muon pairs must be greater than 12 GeV/c$^2$.

The cross sections are calculated inclusively in the number of jets found at NLO. The uncertainties are assessed both for 7 TeV and 8 TeV and assumed to be 100% correlated. The PDF+$\alpha_s$ and QCD scale uncertainties are treated as uncorrelated.

The shape uncertainties in $m_{4\ell}$ distribution imply the knowledge of correlations between possible event yield variations at different $m_{4\ell}$ points. For simplicity, 100% correlation is assumed between errors across the entire $m_{4\ell}$ mass range. With $\mathcal{O}(70)$ observed $ZZ \to 4\ell$ events, the statistical error is about 12%, which is larger than the current theoretical error of $\mathcal{O}(5\%)$.

## 5.2 Reducible and Instrumental Backgrounds

The number of events along with corresponding expected event yield from Z+X and the relative systematic and statistical errors in the signal region in a mass range from $m_1 = 100$ GeV/c$^2$ to $m_2 = 600$ GeV/c$^2$ for the baseline selections are listed in Tab. 5.2.

The statistical error quoted represents the number of events in the control region, while the systematics one is extracted by varying the fake rates by $\pm 1$ sigma and inflated by 10% according to the WZ underestimation.

### 5.2.1 Relative Uncertainties

The assessment of statistical and systematic uncertainties over reducible background prediction method and various sources of uncertainties are discussed below:

Table 5.2: The number of events from Z+X expected and the relative systematics and statistical errors in the signal region in a mass range from $m_1 = 100$ GeV/c$^2$ to $m_2 = 600$ GeV/c$^2$.

| **Analysis over 7 TeV data** | |
|---|---|
| Sample | Baseline (full range) |
| $N^{Z\rightarrow X\rightarrow 4e}$ | 1.7 ± 0.07 (4%) (stat., 649 events) ±0.85 (50%) (syst.) |
| $N^{Z\rightarrow X\rightarrow 4\mu}$ | 0.5 ± 0.06 (12%) (stat., 87 events)±0.25 (50%) (syst.) |
| $N^{Z\rightarrow X\rightarrow 2\mu 2e}$ | 2.0 ± 0.06 (3%) (stat., 839 events)±1.0 (50%) (syst.) |
| **Analysis over 8 TeV data** | |
| Sample | Baseline (full range) |
| $N^{Z\rightarrow X\rightarrow 4e}$ | 5.5 ± 0.1 (2%) (stat., 1932 events)±2.75 (50%) (syst.) |
| $N^{Z\rightarrow X\rightarrow 4\mu}$ | 1.6 ± 0.1 (6%) (stat., 204 events)±0.8 (50%) (syst.) |
| $N^{Z\rightarrow X\rightarrow 2\mu 2e}$ | 7.9 ± 0.16 (2%) (stat., 2685 events)±3.95 (50%) (syst.) |

- The dependance of fake ratios on the exact composition of background processes in a region of interest is one of the main source of systematic uncertainties of the method. The statistical uncertainty of 50% is assigned due to less statistics in signal region.

- The current method can underestimate the reducible background containing three real leptons and one jet faking lepton like WZ. While MC studies have shown that the overall contribution of WZ to the total reducible background is small (between 5 and 10%). The total reducible background estimated with the Z+X method may therefore be underestimated by a small amount (about 7%). This is taken into account by increasing the systematic of the Z+X method by 10%.

- The compositions of reducible background processes ($DY$, $t\bar{t}$, $WZ$, $Z\gamma^{(*)}$) in the region where fake ratios are measure and applied, are typically not the same. The dominating statistical uncertainty is driven by the number of events in the control region and is typically in the range of 5-10%.

- The functional form for the invariant mass ($m_{4\ell}$) shape that is used to extrapolate from the full range of $m_{4\ell}$ to the range of interest is another source of the systematic uncertainty. The respective differences between the shapes of predicted background distributions for all three channels have been examined in order to estimate it. The envelope of differences between these shapes of distributions is used as a measure of the uncertainty of the shape. The uncertainty is estimated to be up to 10 - 15%.

## 5.3 The H→ $ZZ^* \to 4\ell$ Phase Space

The number of candidates observed in 2011 and 2012 data are reported in Tab. 5.3 and 5.4 for the baseline selection in accord with the three final states. These numbers are accompanied by estimated background contributions in the signal region. The reconstructed four-lepton invariant mass distribution is shown in Fig. 5.1 for the full dataset, where different mass ranges are shown, including the mass below 100 GeV/c$^2$ (not used for analysis). The SM background distributions are obtained by combining the rate normalization from data-driven methods and knowledge on shapes taken from the MC samples. Fig. 5.2 is showing the invariant mass distribution of reconstructed $Z_1$ and $Z_2$.

The statistical procedure followed to derive upper limits on the SM Higgs boson cross section times branching ratio is the so-called CLs method, described in Ref. [71]. The expected and observed upper limits at 95% confidence level on the signal strength modifier $\mu = \sigma/\sigma_{SM}$ are shown in Fig. 5.3. In other words, the plot shows the factor by which the SM Higgs boson cross section times branching ratio must be scaled to be excluded at 95% CL, as a function of the Higgs mass. The dashed line has been obtained by tossing toy Monte Carlo pseudo experiments, whereas the solid line shows the results obtained from real data. The green and yellow bands indicate the $\mu$ ranges in which an additional measurement would lie with a probability of 68% and 95%, respectively. An upper limit at 95% confidence level exclude the ranges 113 - 116 GeV/c$^2$ and 129 - 720 GeV/c$^2$ while the expected exclusion range for the standard model Higgs boson is 118 - 670 GeV/c$^2$.

The compatibility of the observed excesses of data events with the background-only hypothesis can be quantified by the p-value. The p-value is the probability of observing an upwards fluctuation of the background event yield at least as large as the one measured in data. It is estimated by tossing a large number of toy MC pseudo-datasets. Its trend as a function of the SM Higgs boson mass is plotted in Fig. 5.4. A local significance above the expected background of 4.5 standard deviations is observed at $m_H \approx 126$ GeV/c$^2$.

Table 5.3: The number of event candidates observed in 2011 data at $\mathcal{L} = 5.05$ fb$^{-1}$, compared to the mean expected background and signal rates for each final state for $100 < m_{4\ell} < 1000$ GeV/c$^2$. For the Z + X background, the estimations are based on data.

| **Channel** | $4e$ | $4\mu$ | $2e2\mu$ |
|---|---|---|---|
| Z + X | $1.88^{+2.45}_{-1.13}$ | $0.99^{+1.49}_{-0.6}$ | $2.97^{+2.97}_{-1.49}$ |
| ZZ background | 15.06 ±1.71 | 22.58 ±2.23 | 35.66 ±3.64 |
| All background expected | $16.94^{+2.99}_{-2.05}$ | $23.58^{+2.68}_{-2.31}$ | $38.63^{+4.7}_{-3.93}$ |
| $m_H$ = 125 GeV | 0.65 ±0.1 | 1.2 ±0.13 | 1.54 ±0.18 |
| $m_H$ = 126 GeV | 0.72 ±0.11 | 1.3 ±0.14 | 1.71 ±0.2 |
| $m_H$ = 200 GeV | 4.12 ±0.48 | 5.86 ±0.59 | 9.84 ±1.02 |
| $m_H$ = 350 GeV | 2.34 ±0.28 | 3.21 ±0.34 | 5.59 ±0.61 |
| $m_H$ = 500 GeV | 0.81 ±0.1 | 1.08 ±0.12 | 1.89 ±0.21 |
| Observed | 14 | 20 | 43 |

Table 5.4: The number of event candidates observed in 2012 data at $\mathcal{L} = 12.21$ fb$^{-1}$, compared to the mean expected background and signal rates for each final state for $100 < m_{4\ell} < 1000$ GeV/c$^2$. For the Z + X background, the estimations are based on data.

| **Channel** | $4e$ | $4\mu$ | $2e2\mu$ |
|---|---|---|---|
| Z+X | $4.46^{+7.58}_{-3.12}$ | $2.08^{+2.29}_{-1.04}$ | $7.04^{+11.26}_{-4.22}$ |
| ZZ background | 40.2 ±4.7 | 60.14 ±6.66 | 98.35 ±10.71 |
| All background expected | $44.66^{+8.92}_{-5.64}$ | $62.22^{+7.04}_{-6.74}$ | $105.39^{+15.54}_{-11.51}$ |
| $m_H$ = 125 GeV | 1.8 ±0.25 | 3.47 ±0.41 | 4.52 ±0.54 |
| $m_H$ = 126 GeV | 1.99 ±0.28 | 3.79 ±0.44 | 4.99 ±0.6 |
| $m_H$ = 200 GeV | 12.68 ±1.52 | 17.82 ±2.02 | 30.4 ±3.38 |
| $m_H$ = 350 GeV | 7.66 ±0.94 | 10.27 ±1.19 | 18.2 ±2.07 |
| $m_H$ = 500 GeV | 2.8 ±0.35 | 3.68 ±0.43 | 6.51 ±0.75 |
| Observed | 45 | 75 | 119 |

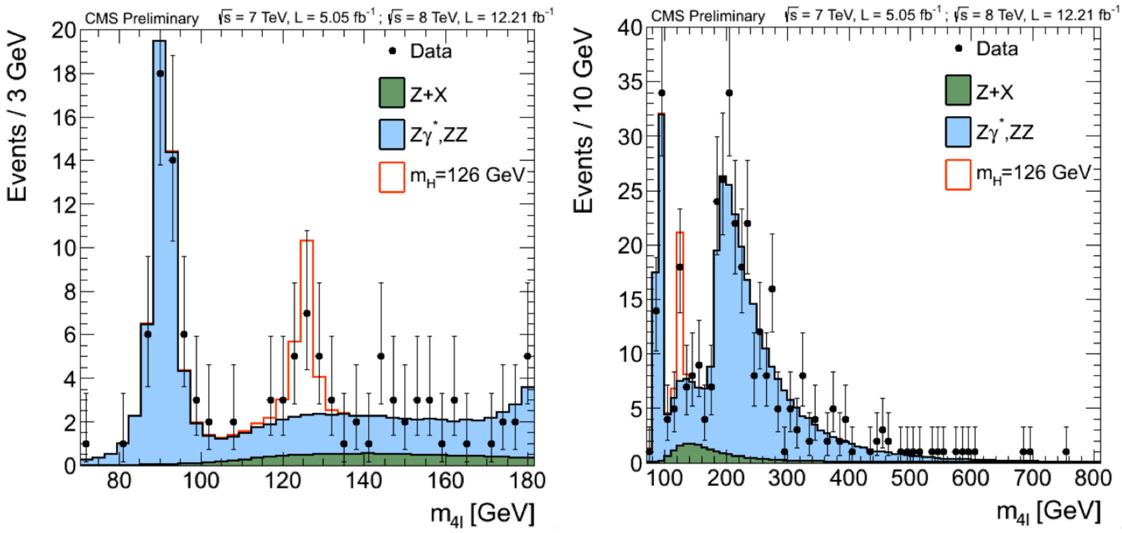


(a) (b)

Figure 5.1: Distribution of the four-lepton reconstructed mass, (a) represents low mass region and (b) is displaying full mass range considered in the analysis. Region $m_{4l} < 100$ GeV/c$^2$ is shown but not used in analysis. The sample correspond to an integrated luminosity of $\mathcal{L} = 5.1$ fb$^{-1}$ of 2011 data and $\mathcal{L} = 12.21$ fb$^{-1}$ of 2012 data.

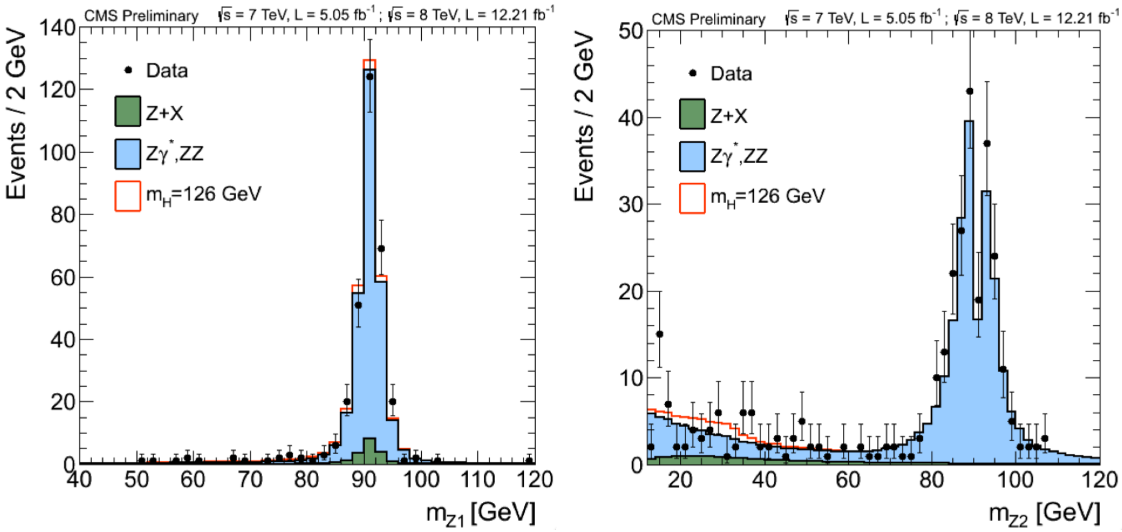


(a) (b)

Figure 5.2: Fig. (a) and (b) are showing invariant mass distributions of Z1 and Z2 respectively. The sample correspond to an integrated luminosity of $\mathcal{L} = 5.1$ fb$^{-1}$ of 2011 data and $\mathcal{L} = 12.21$ fb$^{-1}$ of 2012 data.

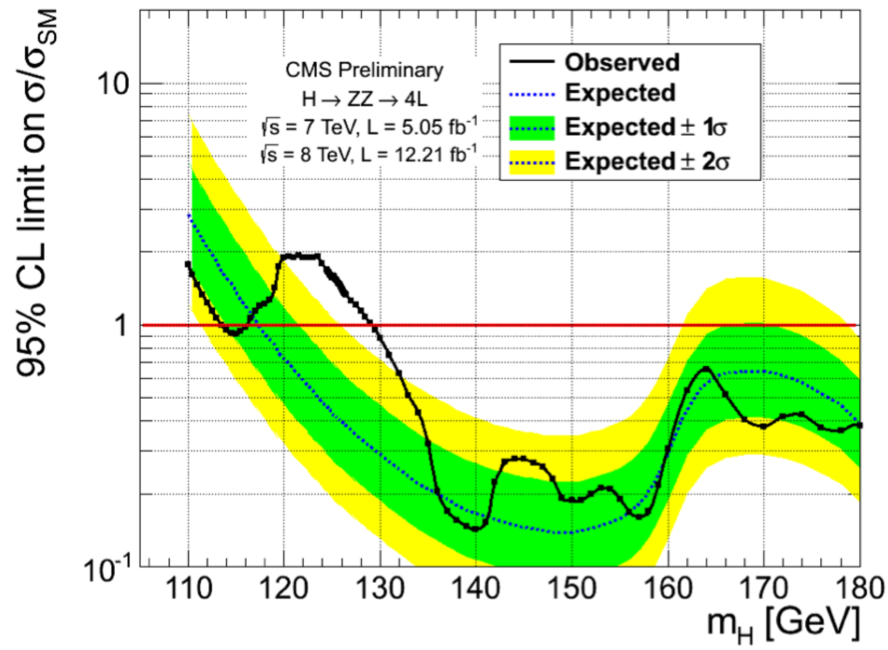


(a)

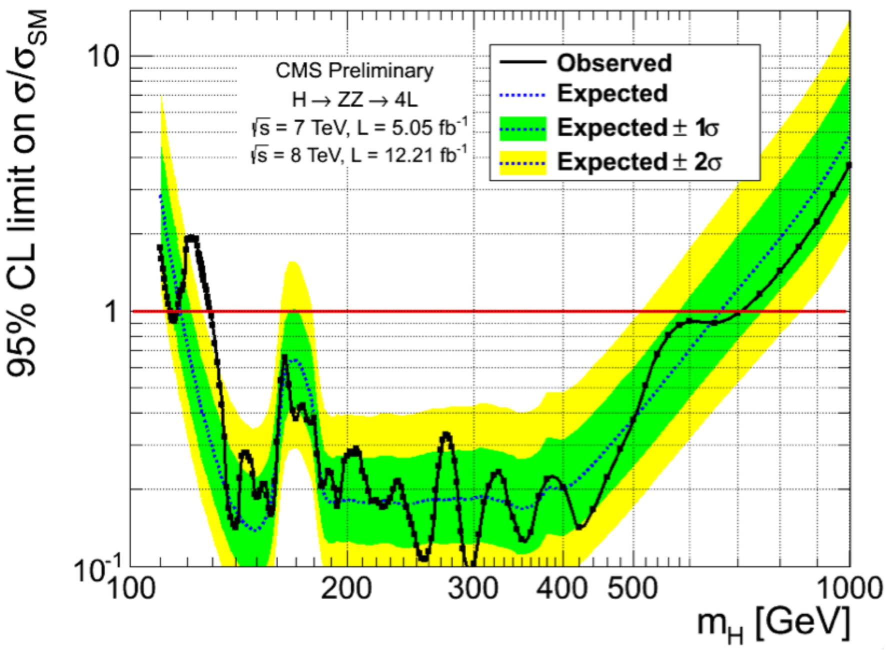


(b)

Figure 5.3: Observed and expected 95% CL upper limit on the ratio of the production cross section to the SM expectation with the 2D fit. 2011 and 2012 data-samples are used. The 68% and 95% ranges of expectation for the background-only model are also shown with green and yellow bands, respectively. (a) represents lower mass range only and (b) shows full mass range.

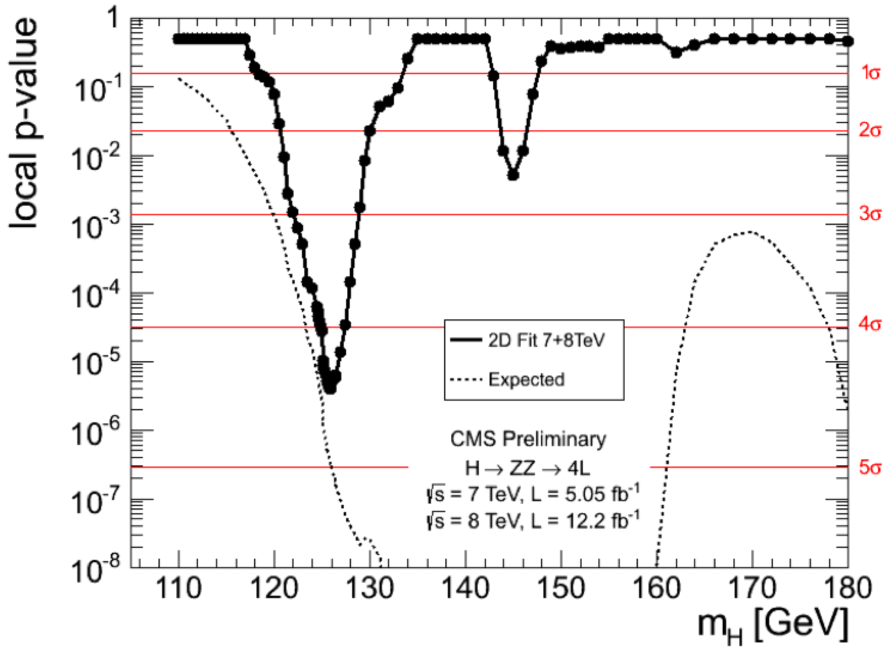


(a)

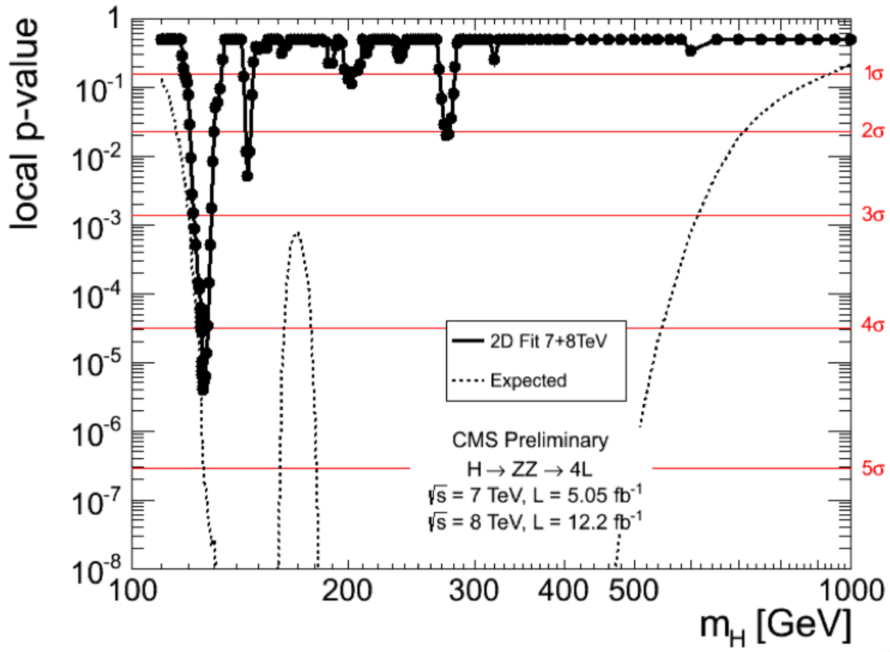


(b)

Figure 5.4: Significance of the local fluctuations with respect to the standard model expectation as a function of the Higgs boson mass for an integrated luminosity of 5.1 fb$^{-1}$ at 7 TeV and 12.21 fb$^{-1}$ at 8 TeV in the low mass range (110 - 180 GeV/c$^2$) in (a) and in the mass range (110 -1000 GeV/c$^2$) in (b). Dashed line shows mean expected significance of the SM Higgs signal for a given mass hypothesis.

## 5.4 ZZ Cross Section Measurement

The initial event selection strategy for ZZ cross section measurement is same as described in Sec. 4.2 but events are constrained to follow mass cuts over $Z_1$, $Z_2$ and $m_{4\ell}$ in accord with *High-mass phase space* only to get both on mass shell Z bosons.

The background contributions extrapolated in signal region for high mass region contributed in cross section measurement as well, which is reported individually for 7 TeV and 8 TeV in Refs. [81] and [82] respectively. The measured values of ZZ cross section with $\sqrt{s} = 7$ TeV & 8 TeV data are reported as:

- $\sigma(pp \rightarrow ZZ) = 6.24^{+0.86}_{-0.80}(stat)^{+0.41}_{-0.32}(syst.) \pm 0.14(lumi.)$ pb at 7 TeV.
- $\sigma(pp \rightarrow ZZ) = 8.4 \pm 1.0(stat.) \pm 0.7(syst.) \pm 0.4(lumi.)$ pb at 8 TeV.

# Conclusions

The search of the SM Higgs boson has to encounter with various SM and electroweak background processes that have similar final states as those of the signal. On the way to the SM Higgs boson search in $H \rightarrow ZZ^* \rightarrow 4\ell$ decay channel, the current thesis have reported results from analysis of the background-like real data events in accord with $H \rightarrow ZZ^* \rightarrow 4\ell$ decay mode. The contribution of all SM and electroweak background processes, contributing in signal phase space have been estimated. In parallel, the proper understanding of the Higgs signal is equally important to comprehend the status of various background events in signal phase space, which leads to the methodological developments for their precise evaluation in signal region.

The analysis have been presented over proton-proton collision data recorded by the CMS detector at the LHC, corresponding to integrated luminosities of 5.05 $fb^{-1}$ @ $\sqrt{s} = 7$ TeV (2011) and 12.21 $fb^{-1}$ @ $\sqrt{s} = 8$ TeV (2012) to perform cut based analysis in two different phase spaces *i.e.* background and Higgs signal.

The major part of research activities was devoted to examine the feasible developments of new techniques for background measurements and to improve the efficiency of existing ones. The multiple ways were checked and studied for background estimation and most efficient techniques are reported in current work.

The very initial tenure of my analysis studies was devoted to comprehend the signatures of predominant source of backgrounds giving 4 *leptons* as final state. These were categorized as *irreducible $ZZ$ continuum*, *reducible backgrounds* ($Zb\bar{b}$, $Zc\bar{c}$ & $t\bar{t}$) and *instrumental backgrounds* (Z+jets or WZ+jet(s)) in accord with their experimental signatures. The preliminary analyses of all these background processes including Higgs signal samples have been performed over MC generator level samples and contributed to comprehend the topologies of individual final states by understanding the signatures of the relevant decays. The important kinematic distributions ($m_{4l}$, $m_{\ell\ell}$, $p_T$ of leptons etc.) obtained at MC level have shown the inherent challenges to get a clear Higgs signal signature in low mass range. It displays the impulse to development of effective background estimation methodologies by paying particular attention to low mass Higgs searches and contributed in the development of event selection strategy for background and Higgs signal phase spaces.

The present work have contributed in the development and improvement of the techniques to reconstruct $H \rightarrow ZZ^* \rightarrow 4\ell$ final sates in accord with individual lepton flavor (4e, $4\mu$, $2e2\mu$), by keeping higher efficiency to select Higgs signal.

The irreducible ZZ continuum have been measured from MC to get its estimate in Higgs signal phase space. On the other hand, to cop with low MC statistics problem in case of instrumental (Z + light jets, WZ + jets) & reducible ($Zb\bar{b}$, $Zc\bar{c}$, $t\bar{t}$) backgrounds, an inclusive approach has been accomplished for their measurement directly from data by applying fake rate probabilities over leptons to be misidentified by jets. The event rates measured in the background control region are extrapolated to the signal region to evaluate their contribution in Higgs signal phase space.

In addition, the feasible improvements in the $H \rightarrow ZZ^* \rightarrow 4\ell$ event selection methodology to increase the Higgs signal selection efficiency has been examined.

The studies presented in this thesis over background estimations have contributed in below mentioned research:

- The combined results at $\sqrt{s} = 7$ TeV & 8 TeV data in context of $H \rightarrow ZZ^* \rightarrow 4\ell$ analysis have resulted in an observation of a new boson with a local significance above the expected background of 4.5 standard deviations as shown in Ref. [76]. It could be the SM Higgs boson but it's not yet confirmed. A measurement of its mass gives 126.2 ± 0.6 (stat) ± 0.2 (syst) GeV/$c^2$. No other significant excess is found, and upper limits at 95% confidence level exclude the mass ranges 113 - 116 GeV/$c^2$ and 129 - 720 GeV/$c^2$ while the expected exclusion range for the standard model Higgs boson is 118 - 670 GeV/$c^2$.

- The ZZ cross section measurement at $\sqrt{s} = 7$ TeV & 8 TeV data.

# Bibliography

[1] ALEPH, DELPHI, L3, OPAL Collaborations, and LEP Working Group for Higgs Boson Searches, "Search for the standard model Higgs boson at LEP ", *Phys. Lett. B*, 565 (2003) 61.

[2] The Tevatron New-Phenomena and Higgs Working Group, for the CDF and D0 Collaborations, "Combined CDF and D0 Search for Standard Model Higgs Boson Production with up to 10 $fb^{-1}$ of Data", *FERMILAB-CONF-12-065-E*, CDF Note 10806, D0 Note 6303.

[3] K. Nakamura et al., "Review of particle physics", *J.Phys.G*,vol. G37, p. 075021, 2010.

[4] G. Bertone, D. Hooper, and J. Silk, "Particle dark matter: Evidence, candidates and constraints", *Phys.Rept.*, vol. 405, pp. 279-390, 2005.

[5] N. Jarosik, C. Bennett, J. Dunkley, B. Gold, M. Greason, et al., "Seven-Year Wilkinson Microwave Anisotropy Probe (WMAP) Observations: Sky Maps, Systematic Errors, and Basic Results,". *Astrophys.J.Suppl.*, vol. 192, p. 14, 2011.

[6] A. D. Martin F. Halzen. *"Quarks Leptons: An Introductory Course in Modern ParticlePhysics"*. Wiley, 1984.

[7] D. H. Perkins. *"Introduction To High Energy Physics"*. Cambridge University Press, 2000.

[8] S. Dawson, "Introduction to Electroweak Symmetry Breaking", *hep-ph/9901280.*

[9] S. Chatrchyan *et al.* [CMS Collaboration], "Observation of Z decays to four leptons with the CMS detector at the LHC", *arXiv:1210.3844*, [hep-ex].

[10] ATLAS Collaboration, "An update to the combined search for the Standard Model Higgs boson with the ATLAS detector at the LHC using up to 4.9 $fb^{-1}$

of pp collision data at $\sqrt{s} = 7$ TeV", *ATLAS Conference Report*, ATLAS-CONF-2012-019, (2012).

[11] CMS searchesCollaboration, " Combination of SM, SM4, FP Higgs boson", *CMS Physics Analysis Summary*, CMS-PAS-HIG-12-008, (2012).

[12] LHC Higgs Cross Section Working Group, S. Dittmaier, C. Mariotti, G. Passarino, and R. Tanaka (Eds.), "Handbook of LHC Higgs Cross Sections: 1. Inclusive Observables", *CERN-2011-002*, CERN, Geneva, 2011.

[13] The LHC Study Group Collaboration. "LHC-the Large Hadron Collider accelerator project". Technical report, CERN-AC-93-03, 2003.

[14] The LHC Study Group Collaboration. "LHC-the Large Hadron Collider conceptual design". Technical report, CERN-AC-95-05, 2005.

[15] L. Evans, P. Bryant [LHC Collaboration]. "LHC - Machine". *JINST*, 3, 2008.

[16] K Nakamura and Particle Data Group, "Review of particle physics.", of Physics G: Nuclear and Particle Physics, 37(7A):075021, 2010.

[17] Roger Eckhardt. Stan Ulam, John Von Neumann, and the Monte Carlo method. *Los Alamos Science, Special Issue 15,* 15:131-137, 1987.

[18] M.A. Dobbs et al., "Les houches guidebook to monte carlo generators for hadron collider physics", *hep-ph/0403045*, 2004.

[19] T. Sjostrand, S. Mrenna, and P. Skands, "PYTHIA 6.4 Physics and Manual", *JHEP, 05(026)*, 2006.

[20] S. Alioli et al., "A general framework for implementing nlo calculations in shower monte carlo programs: the powheg box", *JHEP*, 1006:043, 2010.

[21] T. Binoth, N. Kauer, and P. Mertsch. "Gluon-induced QCD corrections to $pp \rightarrow \ell\bar{\ell}\ell'\bar{\ell}'$", 2008.

[22] The Geant4 Collaboration, "GEANT-Detector Description and Simulation Tool, *http://geant4.web.cern.ch/geant4/*..

[23] J. Alwall et al., "MadGraph/MadEvent v4: The New Web Generation", *JHEP* 09 (2007) 028.

[24] H.-L. Lai et al., "Uncertainty induced by QCD coupling in the CTEQ global analysis of parton distributions", *Phys. Rev. D*, 82 (2010) 054021.

[25] M. Mohammadi Najafabadi, "Single Top production at LHC", *arXiv:hep-ex/0605034*, 2006.

[26] Pierini, M., "talk at the Joint PVT/PO Meeting", *https://twiki.cern.ch/twiki/bin/viewauth/CMS/PdwgMain*, 2011.

[27] C. Mariotti et al. LHC Higgs Cross Section Working Group, S. Dittmaier. "Handbook of LHC Higgs Cross Sections:1. Inclusive Observables". Technical report, CERN, Geneva., 2011.

[28] CMS Collaboration, " MUO-10-004: Performance of CMS muon reconstruction in pp collision events at $\sqrt{s} = 7$ TeV", *Technical report*, In preparation to JINST (2010).

[29] G. Daskalakis et al., "Measuring Electron Efficiencies at CMS with Early Data", *CMS Analysis Note 2007/019*, 2007.

[30] Hung-Liang Lai et al. "New parton distributions for collider physics". *Phys. Rev.*, D82, 2010.

[31] R. D. Ball, L. Del Debbio, S. Forte, A. Guffanti, J. I. Latorre, J. Rojo and M. Ubiali, "A first unbiased global NLO determination of parton distributions and their uncertainties", *Nucl. Phys B (2010)*, no. 838, 136.

[32] A. D. Martin, W. J. Stirling, R. S. Thorne and G. Watt, "Parton distributions for the LHC", *Eur. Phys. J C*, (2009), no. 63, 189.

[33] C. Anastasiou, R. Boughezal, and F. Petriello, "Mixed QCD-electroweak corrections to Higgs boson production in gluon fusion", *JHEP*, 04 (2009) 003.

[34] D. de Florian and M. Grazzini, "Higgs production through gluon fusion: updated cross sections at the Tevatron and the LHC", *Phys. Lett. B* 674 (2009) 291.

[35] S. Dawson, "Radiative corrections to Higgs boson production", *Nucl. Phys. B*, 359 (1991) 283.

[36] M. Spira et al., "Higgs boson production at the LHC", *Nucl. Phys. B*, 453 (1995) 17.

[37] R. V. Harlander and W. B. Kilgore, "Next-to-next-to-leading order Higgs production at hadron colliders", *Phys. Rev. Lett.*, 88 (2002) 201801.

[38] C. Anastasiou and K. Melnikov, “Higgs boson production at hadron colliders in NNLO QCD”, *Nucl. Phys. B*, 646 (2002) 220.

[39] V. Ravindran, J. Smith, and W. L. van Neerven, “NNLO corrections to the total cross section for Higgs boson production in hadron-hadron collisions”, *Nucl. Phys. B*, 665 (2003) 325.

[40] Y. Gao, A. V. Gritsan, Z. Guo et al., “Spin determination of single-produced resonances at hadron colliders”, *Phys.Rev.* D81 (2010) 075022.

[41] S. Catani et al., “Soft-gluon resummation for Higgs boson production at hadron colliders”, *JHEP*, 07 (2003) 028.

[42] S. Actis et al., “NLO Electroweak Corrections to Higgs Boson Production at Hadron Colliders”, *Phys. Lett. B*, 670 (2008) 12.

[43] M. Ciccolini, A. Denner, and S. Dittmaier, “Strong and electroweak corrections to the production of Higgs + 2-jets via weak interactions at the LHC”, *Phys. Rev. Lett.*, 99 (2007) 161803.

[44] M. Ciccolini, A. Denner, and S. Dittmaier, “Electroweak and QCD corrections to Higgs production via vector-boson fusion at the LHC”, *Phys. Rev. D*, 77 (2008) 013002.

[45] T. Figy, C. Oleari, and D. Zeppenfeld, “Next-to-leading order jet distributions for Higgs boson production via weak-boson fusion”, *Phys. Rev. D*, 68 (2003) 073005.

[46] K. Arnold et al., “VBFNLO: A parton level Monte Carlo for processes with electroweak bosons”, *Comput. Phys. Commun.*, 180 (2009) 1661.

[47] P. Bolzoni et al., “Higgs production via vector-boson fusion at NNLO in QCD”, *Phys. Rev. Lett.*, 105 (2010) 011801.

[48] A. Bredenstein et al., “Precise predictions for the Higgs-boson decay H→WW/ZZ→4 leptons”, *Phys. Rev.* D 74 (2006) 013004.

[49] S.Dittmaier et al. A. Bredenstein, A. Denner. “Radiative corrections to the semileptonic and hadronic Higgs-boson decays H→WW/ZZ→4 fermions”. *JHEP*, 0702(080), 2007.

[50] A. Djouadi, J. Kalinowski, M. Muhlleitner et al. “An update of the program HDECAY“. In *The Les Houches 2009 workshop on TeV colliders:The tools and Monte Carlo working group summary report*, 2010.

[51] G. Bozzi, S. Catani, D. de Florian et al., "Transverse-momentum resummation and the spectrum of the Higgs boson at the LHC", *Nucl. Phys. B* 737 (2006) 73.

[52] I. Pulljak et al. A. Denner, S. Heinemeyer. "Standard Model Higgs-Boson Branching Ratios with Uncertainties". *Eur. Phys. J.*, C71(1753), 2011.

[53] S. Actis, G.Passarino, C. Sturm et al. "NNLO Computational Techniques: the Cases $H \to \gamma\gamma$ and $H \to gg$". *Nucl. Phys.*, B811:182–273, 2009.

[54] S. Baffioni et al. "Search strategy for the Higgs boson in the ZZ* decay channel with the CMS experiment", *CMS-AN*, 2010/237, 2008.

[55] M. Cacciari, S. Frixione, M. Mangano et al., "Updated predictions for the total production crosssections of top and of heavier quark pairs at the Tevatron and at the LHC".

[56] W. Adam, S. Baffioni, F. Beaudette et al. "Electron Reconstruction in CMS". CMS AN-2009/164, November 2009.

[57] CMS Collaboration, " Electron reconstruction and identification at $\sqrt{s} = 7$ 7 TeV", *CMS Physics Analysis Summary*, CMS-PAS-EGM-10-004 (2010).

[58] CMS Collaboration, " Electron commissioning results at at $\sqrt{s} = 7$ TeV", *CMS Detector Performance Summaries* 2011/003 (2011).

[59] S. Baffioni et al, " Electron Charge Determination Commissioning from 7 TeV Data", *CMS-AN*, 2010/468 (2010).

[60] M. Cacciari and G. P. Salam, "Pileup subtraction using jet areas", *Phys. Lett.* B659 (2008) 119-126.

[61] M. Cacciari, G. P. Salam, and G. Soyez, "The Catchment Area of Jets, *JHEP* 04 (2008) 005.

[62] CMS Collaboration, "Updated results on the new boson discovered in the search for the standard model Higgs boson in the $H \to ZZ \to 4l$ channel in pp collisions at $\sqrt{s} = 7$ and 8 TeV", *CMS-AN*, 2012/367 (2012).

[63] G. Abbiendi, N. Adam et al. "Muon Recostruction in the CMS Detector". CMS AN 2008/097, July 2009.

[64] K. Fruhwirth, "Application of Kalman filtering to track and vertex fitting", *Nucl.Instrum.Meth. A*, 262 (1987) 444.

[65] CMS Collaboration, “Performance of CMS muon reconstruction in cosmic-ray events”, *JINST*, 5 (2010) T03022.

[66] CMS Collaboration, “CMS Physics Technical Design Report, volume I: Detector performance and software “, *CERN/LHCC*, 2006-001 (2006).

[67] CMS Collaboration, “Measurement of tracking efficiency”, *CMS Physics Analysis Summary*, CMS-PAS-TRK-10-002 (2010).

[68] A. Bodek and J. Han, “Improved Rochester Misalignment and Muon Scale Corrections Extracted for 2011A, 2011B CMS Data”, *CMS-AN* 2012/298 (2012).

[69] CMS Collaboration, “Search for the standard model Higgs boson in the decay channel H to ZZ to 4 leptons in $pp$ collisions at $\sqrt{(s)} = 7$ TeV”, *Phys.Rev.Lett.*, 108 (2012) 111804, February 2012.

[70] https://twiki.cern.ch/twiki/bin/view/CMS/MultivariateElectronIdentification

[71] A. L. Read. “Modified Frequentist analysis of search results (the $CL_s$ method)”. Yellow Report 81, CERN-2000-005, 2000.

[72] S. Alekhin et al., “The PDF4LHC working group interim report, *arXiv:hep-ph/1101.0536.*.

[73] CMS Collaboration, “Commissioning of the particle-flow event reconstruction with leptons from J/Psi and W decays at 7 TeV, *CMS Physics Analysis Summary*, CMS-PAS-PFT-10-003 (2010).

[74] CMS Collaboration, “Performance of CMS muon reconstruction in pp collisions at $\sqrt{s} = 7$ TeV”, *CMS PAS* , MUO-10-002 (2010).

[75] K. Ellis C.W J. Campbell. “MCFM-Monte Carlo for FeMtobarn process”, 2011.

[76] CMS Collaboration, “Updated results on the new boson discovered in the search for the standard model Higgs boson in the $H \rightarrow ZZ \rightarrow 4l$ channel in pp collisions at $\sqrt{s} = 7$ and 8 TeV”, *CMS-PAS-HIG-12-041*, November 2012.

[77] “https://twiki.cern.ch/twiki/bin/view/TMVA/WebHome”.

[78] “http://www.cs.toronto.edu/ radford/fbm.software.html”.

[79] J. Bochenek, P.C. Bhat, N. De Filippis, K.F. Johnson, H.B. Prosper, G. Singh, S.Tentindo, “ Bayesian Search for a Higgs Boson in the Decay Channel $H \rightarrow ZZ \rightarrow 4l$”, *CMS-AN-2012/334*, September 2012.

[80] J. Bochenek, P.C. Bhat, D. Charles, N. De Filippis, K.F. Johnson, H.B. Prosper, G.Singh, S. Tentindo, "Search for the Standard Model Higgs Boson in the Decay Channel $H \rightarrow ZZ \rightarrow 4l$: a Bayesian Approach", *CMS-AN-2012/129*, August 2012.

[81] CMS Collaboration, "Measurement of the ZZ production cross section and search for anomalous couplings in 2l2l' final states in pp collisions at $\sqrt{s} = 7$ TeV data", *CERN-PH-EP-2012-336*,

[82] CMS Collaboration, "of ZZ production cross section in ZZ → 2l2l' decay channel in pp collisions at $\sqrt{s} = 8$ TeV", *CMS-PAS-SMP-12-014*, July 2012.

gluon fusion".